



CONTENTS

**Biochemistry**

- M. L. Mihajlović and P. M. Mitrašinović*: Some novel insights into the binding of oseltamivir and zanamivir to H5N1 and N9 influenza virus neuraminidases: a homology modeling and flexible docking study ..... 1
- S. S. Stajković, S. Z. Borozan and G. Gađanski-Omeović*: The effect of toluene on oxidative processes in rat blood ..... 15
- B. M. Mandić, D. N. Gođevac, V. P. Beškovski, M. R. Simić, S. S. Trifunović, V. V. Tešević, V. V. Vajs and S. M. Milosavljević*: Pyrrolizidine alkaloids from seven wild-growing *Senecio* species in Serbia and Montenegro ..... 27
- N. S. Radulović, P. D. Blagojević, R. M. Palić, B. K. Zlatković and B. M. Stevanović*: Volatiles from vegetative organs of the palaeoendemic resurrection plants *Ramonda serbica* Panč. and *Ramonda nathaliae* Panč. et Petrov. .... 35

**Theoretical Chemistry**

- M. R. Darafsheh and A. Moghani*: Q-conjugacy character table for the non-rigid group of 2,3-dimethylbutane ..... 45

**Physical Chemistry**

- M. Jović, M. Dašić, K. Holl, D. Ilić and S. Mentus*: Gel-combustion synthesis of  $\text{CoSb}_2\text{O}_6$  and its reduction to powdery  $\text{Sb}_2\text{Co}$  alloy ..... 53

**Materials**

- S. Kostić, A. Golubović and A. Valčić*: Primary and secondary dendrite spacing of Ni-based superalloy single crystals ..... 61
- B. Babić-Stojić, D. Milivojević and J. Blanuša*: Ferromagnetic behaviour of the Zn–Mn–O system ..... 71

**Environment**

- M. Simonić*: Removal of inorganic  $\text{As}^{5+}$  from a small drinking water system ..... 85
- M. Kresović, M. Jakovljević, S. Blagojević and S. Maksimović*: Specific transformations of mineral forms of nitrogen in acid soils ..... 93



www.shd.org.rs

*J. Serb. Chem. Soc.* 74 (1) 1–13 (2009)

JSCS–3803

Journal of  
the Serbian  
Chemical Society

JSCS@tmf.bg.ac.yu • www.shd.org.rs/JSCS

UDC 578.7:616.988.7:598.2

Original scientific paper

## Some novel insights into the binding of oseltamivir and zanamivir to H5N1 and N9 influenza virus neuraminidases: a homology modeling and flexible docking study

MARIJA L. MIHAJLOVIĆ<sup>1,2#</sup> and PETAR M. MITRAŠINOVIĆ<sup>2\*#</sup>

<sup>1</sup>Faculty of Physical Chemistry, University of Belgrade, Studentski trg 12–16, 11000 Belgrade and <sup>2</sup>Institute for Multidisciplinary Research, Kneza Višeslava 1, 11030 Belgrade, Serbia

(Received 2 April, revised 21 October 2008)

**Abstract:** In the context of the recent pandemic threat by the worldwide spread of H5N1 avian influenza, novel insights into the mechanism of ligand binding and interaction between various inhibitors (zanamivir – ZMV, oseltamivir – OTV, 2,3-didehydro-2-deoxy-*N*-acetylneuraminic acid – DANA, peramivir – PMV) and neuraminidases (NA) are of vital importance for the structure-based design of new anti-viral drugs. To address this issue, three-dimensional models of H5N1-NA and N9-NA were generated by homology modeling. Traditional residues within the active site throughout the family of NA protein structures were found to be highly conserved in H5N1-NA. A subtle variation between lipophilic and hydrophilic environments in H5N1-NA with respect to N9-NA was observed, thus shedding more light on the high resistance of some H5N1 strains to various NA inhibitors. Based on these models, an ArgusLab4/AScore flexible docking study was performed. The conformational differences between OTV bound to H5N1-NA and OTV bound to N9-NA were structurally identified and quantified. A slight difference of less than 1 kcal mol<sup>-1</sup> between the OTV-N9 and OTV-N1 binding free energies is in agreement with the experimentally predicted free energy difference. The conformational differences between ZMV and OTV bound to either H5N1-NA or N9-NA were structurally identified. The binding free energies of the ZMV complexes, being slightly higher than those of OTV, are not in agreement with what was previously proposed using homology modeling. The differences between ZMV and OTV are suggested to be ascribed to the presence/absence of Asn166 in the active cavity of ZMV/OTV in H5N1-NA, and to the presence/absence of Ser165 in the binding site of ZMV/OTV in N9-NA. The charge distribution was evaluated using the semi-empirical AM1 method. The trends of the AM1 charges of the ZMV and OTV side chains in the complexes deviate from those previously reported.

**Keywords:** H5N1 avian influenza virus neuraminidase; homology modeling; zanamivir; oseltamivir; Argus Lab 4.0 docking.

\* Corresponding author. E-mail: petar.mitrasinovic@cms.bg.ac.yu

# Serbian Chemical Society member.

doi: 10.2298/JSC0901001M

## INTRODUCTION

Due to the recent pandemic threat by the worldwide spread of H5N1 avian influenza, the World Health Organization has shown its profound concern regarding the possibility of an imminent spread of the virus among humans. Reports about the resistance of the virus to two approved anti-influenza drugs (OTV – Tamiflu, ZMV – Relenza, Fig. 1), which target the neuraminidase (NA) enzymes of the virus, as well as the lack of an adequate vaccine have raised the urgent question of developing new anti-viral drugs.<sup>1</sup> Even though influenza virus NA has hitherto been structurally well studied, the structure of H5N1-NA offers new opportunities for drug design.<sup>2</sup>

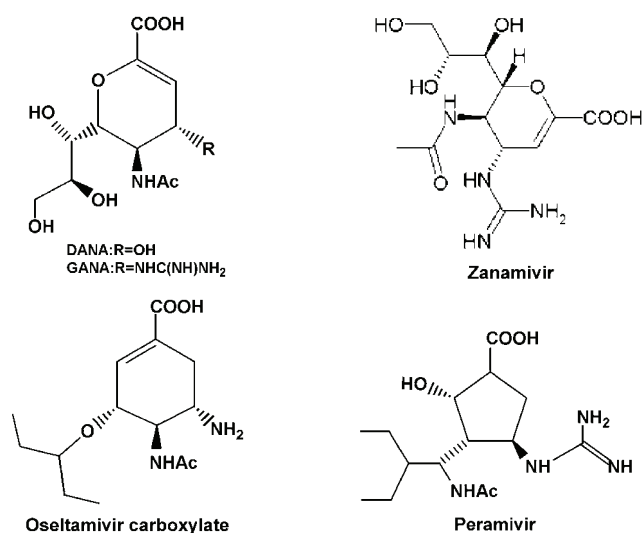


Fig. 1. The chemical structures of DANA, zanamivir, oseltamivir and peramivir.

Computational methods, such as homology modeling and flexible docking, have been identified as viable partner to experiment in the structure-based design of more potent H5N1-NA inhibitors.<sup>3-6</sup> Due to some controversy between the experimentally and computationally predicted susceptibilities of OTV to N1 and N9,<sup>7</sup> a deeper understanding of the mechanism of ligand binding and interaction between commercial drugs and NAs is currently indispensable. To place the controversy on a more rational ground, NA structural models of a quite satisfactory stereochemical quality have been herein employed to provide several novel insights into the binding of ZMV and OTV to H5N1-NA and N9-NA.

## EXPERIMENTAL

*Homology modeling of H5N1-NA and N9-NA*

Comparative modeling is a quite useful means of predicting unknown 3D protein structures by both starting from a known primary structure and relying on known 3D structures of homologous proteins. Sequentially related proteins are assumed to adopt similar conforma

tions, atomic positions in homologous regions are borrowed from known protein structures, while non-homologous portions are predicted in various ways, including potential energy minimization, molecular dynamics and simulated annealing. Two most convenient criteria for similarity are: a) an identity of at least 25 % for a sequence size > 100 amino acids and b) an expectation ( $E$ ) <  $10^{-4}$ , which gives the likelihood that similarities are due to chance. The NA protein, containing 449 amino acids from the highly pathogenic chicken H5N1 A viruses isolated during the 2003–2004 influenza outbreaks in Japan (Accession No. Q5H895) was chosen to be modeled.<sup>8</sup> The sequence of N9-NA (Accession No. Q84070), which contains 470 amino acids, was also selected for modeling.<sup>9</sup> Swiss-Model, an automated comparative modeling approach accessible *via* the ExPASy web server, was employed for the prediction of 3D NA structures.<sup>10</sup> The H5N1-NA model (Fig. 2) was based on the template with a resolution of 2.5 Å (PDB ID: 2htyG),<sup>2</sup> while the N9-NA model was based on the template crystal structure having a 1.4 Å resolution (PDB ID: 1f8dA).<sup>11</sup> The two crystal structures were identified as the best templates in terms of both sequence identity and  $E$  value. To drive the generated coordinates toward optimal geometry, energy minimization on the constructed structures was performed using the Newton subroutine within the Tinker suite of programs, known as the Software Tools for Molecular Design running under the Windows operating system.<sup>12</sup> Running the modeling tools was facilitated by Force Field Explorer 4.2, a graphical user interface to Tinker.<sup>13</sup> The Amber force field parameter set (amber99.prm), as implemented in the Tinker distribution, was used.<sup>14</sup> The Newton algorithm is usually the best choice for minimizations to the 0.01 to 0.000001 kcal mol<sup>-1</sup> Å<sup>-1</sup> level of root-mean-square (rms) gradient convergence. The 0.0001 criterion was chosen in the computations. To evaluate the stereochemical quality of the optimized protein structures by considering their  $G$ -factors, the final structures were analyzed by the Procheck program.<sup>15,16</sup> The  $G$ -factor provides a measure of how “normal”, or alternatively how “unusual”, a given stereochemical property is. In Procheck, both various combinations of torsion angles and covalent geometry are computed taking into account the main-chain bond lengths and the main-chain bond angles. The  $G$ -factor is a score based on the observed

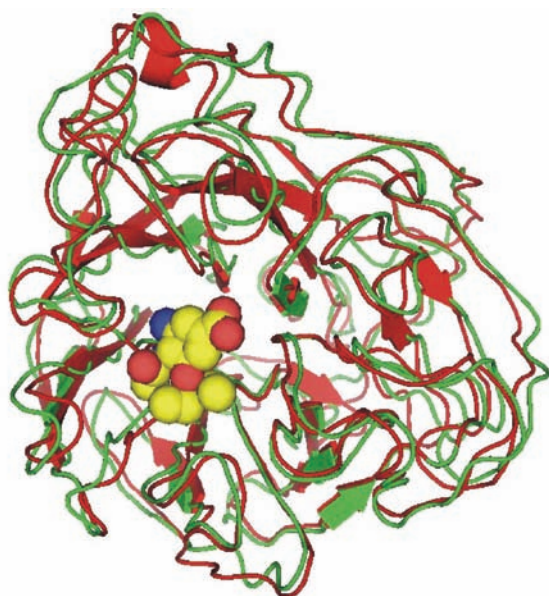


Fig. 2. A cartoon representation of the 3D-structural model of H5N1 superimposed on the 2htyG template and complexed with oseltamivir. The model is colored in red, the template is given in green, and the ligand is rendered in space-filling representation.

distributions of these stereochemical parameters. When applied to a given residue, a low  $G$ -factor indicates that the property corresponds to a low-probability conformation. For example, residues falling in the disallowed regions of the Ramachandran plot will have a low (or very negative)  $G$ -factor. Ideally, the scores should be above  $-0.5$ . Values below  $-1.0$  may need investigation. For the H5N1-NA and N9-NA optimized models, the estimated  $G$  factors were  $-0.5$  and  $-0.48$ , respectively. Figures shown in this article were generated by PyMol.<sup>17</sup> Figure 2 shows that the generated model and the template structure of H5N1-NA overlap nicely to a great extent, except in the loop regions due to the sequence alignment.

#### *ArgusLab4/AScore/ShapeDock flexible docking*

The docking problem is conceivable as a complicated optimization or an exhaustive search problem involving many degrees of freedom. Hence, the development of efficient docking algorithms would be of vital importance for the design of new drugs. The ultimate goal is to find the optimal ligand/protein configurations and accurately as well as consistently predict their binding free energy without relying on formal statistical mechanics approaches. To computationally accomplish the key objective within a reasonable time framework, an empirical scoring function (AScore) and a docking engine (ShapeDock) were developed in the ArgusLab 4.0 program.<sup>18</sup>

The AScore is based on the deconvolution of the total protein–ligand binding free energy into several distinct components:

$$\Delta G_{\text{binding}} = \Delta G_{\text{vdW}} + \Delta G_{\text{hydrophobic}} + \Delta G_{\text{H-bond}} + \Delta G_{\text{H-bond(chg)}} + \Delta G_{\text{deformation}} + \Delta G_0 \quad (1)$$

The dissected terms account for the van der Waals interaction between the ligand and the protein, the hydrophobic effect, the hydrogen bonding between the ligand and the protein, the hydrogen bonding involving charged donor and/or acceptor groups, the deformation effect, and the effects of the translational and rotational entropy loss in the binding process, respectively. The intra-ligand van der Waals energy is also included in the overall vdW term. These contributions can be conveniently written as the following products:  $\Delta G_{\text{vdW}} = C_{\text{vdW}} \times \text{vdW}$ ,  $\Delta G_{\text{hydrophobic}} = C_{\text{hydrophobic}} \times \text{HP}$ ,  $\Delta G_{\text{H-bond}} = C_{\text{H-bond}} \times \text{HB}$ ,  $\Delta G_{\text{H-bond(chg)}} = C_{\text{H-bond(chg)}} \times \text{HB(chg)}$ ,  $\Delta G_{\text{deformation}} = C_{\text{rotor}} \times \text{RT}$  and  $\Delta G_0 = C_{\text{regression}}$ . Each of the contributions possesses a specific regression coefficient multiplying a term that has a clear physical meaning. Investigating the regression coefficients enables more profound insights into the receptor–ligand binding process.

The ShapeDock docking engine approximates a complicated search problem. Flexible ligand docking is available by describing the ligand as a torsion tree. Groups of bonded atoms that do not have rotatable bonds are nodes, while torsions are connections between the nodes. The topology of a torsion tree is a determinative factor influencing efficient docking. A balanced tree with a large central node is presumably the favorite case. Two grids, overlaying the binding site, distinguish grid points with respect to the free volume of the binding site. A fine grid is used to examine whether atoms of a pose fragment are inside or outside the binding site, while a coarse grid is used to establish the search points inside the binding site. A set of energetically favorable rotations is generated by placing the root node of a ligand on a search point in the binding site. The torsion search of poses is defined by constructing torsions in breadth-first order for each rotation. Of the surviving poses candidates, the  $N$ -lowest energy poses ( $N$  usually 50–150) makes the final set of poses undergoing coarse minimization, re-clustering and ranking. The AScore/ShapeDock docking protocol is fast, reproducible, and formally explores all energy minima. To illustrate this standpoint, typical ShapeDock times for ligands with 10–15 torsions are shorter than 30 s on a 2.4 GHz Pentium computer.

## RESULTS AND DISCUSSION

Based on different antigenic properties of various glycoprotein molecules, influenza type A viruses are classified into the following subtypes: 16 for haemagglutinin (H1–H16) and 9 for neuraminidase (N1–N9). Two phylogenetically distinct groups, group 1 (N1, N4, N5, N8) and group 2 (N2, N3, N6, N7, N9), contain N1 and N2 NAs of viruses that currently circulate in humans. One of such viruses is the H5N1 avian influenza, which is threatening a new pandemic.<sup>2</sup> There have also been indications that inhibitor structure/activity relationships do not apply across subtypes.<sup>19</sup> To learn more on the subtle differences between the active cavities of two subtypes, it is necessary to explore hydrophobic effects, as they are a key factor underlying drug design.

Even though well-established residues in the active sites are highly conserved across influenza A NA subtypes, NA inhibitors tend to show different affinities for two influenza subtypes, such as N1 and N9. The different activities are presumably due to a small, but significant, difference between two lipophilic environments. Thus, the lipophilic and hydrophilic surfaces of H5N1-NA and N9-NA are shown in Fig. 3. Note a subtle variation between the lipophilic and hydrophilic environments in H5N1-NA with respect to N9-NA. A partially lipophilic pocket containing Ala261 and Tyr262 in H5N1-NA is lined up by two hydrophilic residues, Asn265 and Asn266, in N9-NA. A partially hydrophilic pocket containing Ser165 and Asn166 in H5N1-NA is lined up with two lipophilic residues, Ala166 and Thr167, in N9-NA. The particular mutations within the H5N1-NA protein structure might be correlated with the high resistance to the existing NA inhibitors.<sup>6</sup> When inhibitor binding depends on either interactions with non-essential active-site amino acids or active-site amino-acid reorientation, the possibility of genomic H5N1 mutants escaping might increase.

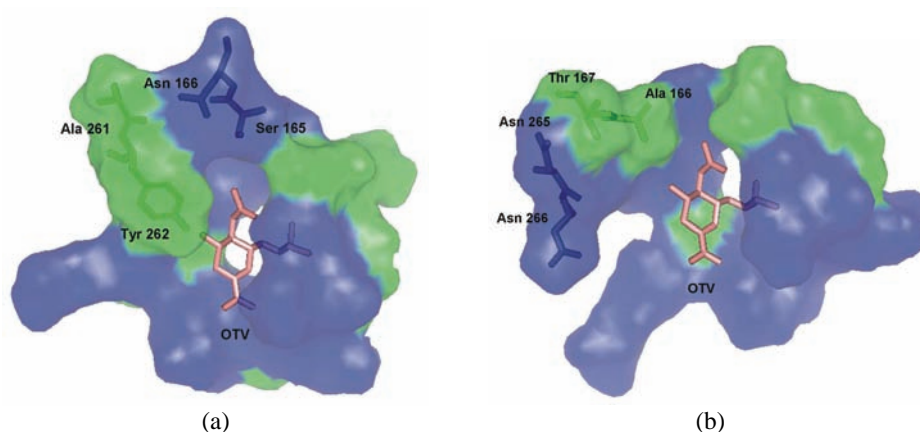


Fig. 3. Lipophilic (green) and hydrophilic (blue) environments (residues) near or in the active site of H5N1-NA (a) and N9-NA (b).

A hydrophobic difference in the binding region of the glycerol side chain has been proven to be particularly sensitive.<sup>20</sup> To fundamentally understand the inhibitory activity of ligands such as ZMV and DANA, it is important to focus on the lipophilic and hydrophilic interactions between their glycerol side chains and the active pockets. The glycerol side chain of both ZMV and DANA has three hydrophilic hydroxyl groups and lipophilic carbons (C8 and C9) and can, therefore, be viewed as a partially lipophilic group. The lipophilic pocket formed by Arg144, Glu197 and Ala166 in the complex of N9-NA with ZMV and DANA is not present in the complex of H5N1-NA with these two ligands.<sup>6</sup> In ZMV/DANA-H5N1-NA, the glycerol group is tightly bound to Ser165 and Glu196 by the formation of 4 hydrogen bonds, without being able to adapt itself to the changed lipophilic environment.<sup>6</sup> In this respect, OTV, having an  $-O-R$  group instead of the glycerol side chain, is quite a different inhibitor than either ZMV or DANA (Fig. 1). The binding interactions of oseltamivir with the residues in the active site of H5N1-NA and N9-NA are schematically shown in Fig. 4. It is well established that two or three Arg residues surrounding the carboxylic group of a ligand, which makes strong electrostatic interactions with these particular Arg residues, are the predominant factor for orienting and stabilizing various inhibitors.<sup>21,22</sup> In OTV/N9-NA, there is only Arg37 in the immediate vicinity of the  $-COO^-$  group, which makes an electrostatic interaction with the particular Arg residue. In contrast to this, note the two Arg residues (Arg36 and Arg74), in addition to Glu37, in the immediate vicinity of the carboxylic group, which makes strong charge–charge interactions with each of the particular residues in OTV/H5N1-NA. Therefore, the more stabilizing effect of the H5N1-NA binding site relative to the

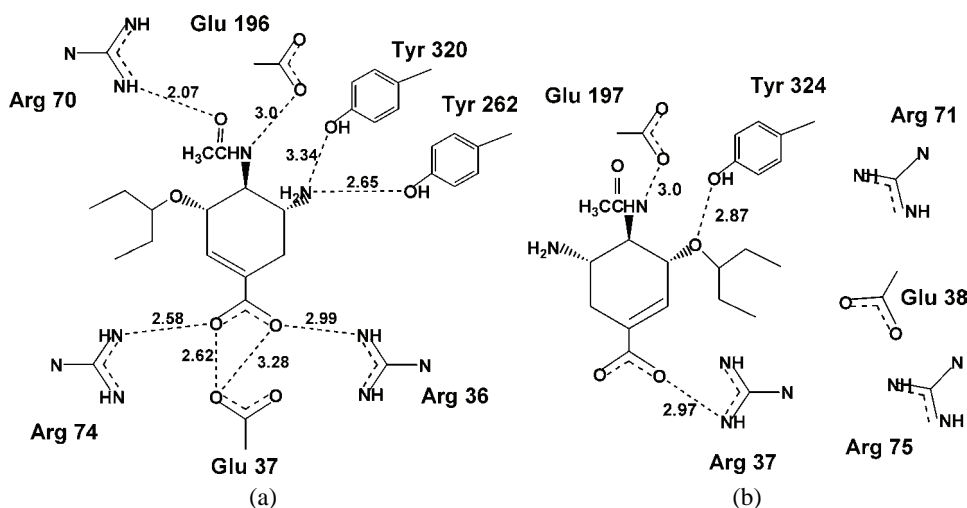


Fig. 4. The binding interactions (in Å) of oseltamivir with the residues in the active site of H5N1-NA (a) and N9-NA (b).

N9-NA binding site on OTV is quite clear. This is in agreement with the binding free energies,  $-6.63$  and  $-7.47$  kcal mol<sup>-1</sup>, of OTV docked into N9-NA and H5N1-NA, respectively (Table I). A slight difference of less than 1 kcal mol<sup>-1</sup> between the binding free energies of OTV-N9 and OTV-N1 is in agreement with the experimentally predicted free energy difference<sup>23</sup> but significantly in contrast to the computationally predicted lower susceptibility of OTV to N1 than to N9 by about 6 kcal mol<sup>-1</sup>.<sup>7</sup> Also, there are no differences between the net charges of the OTV side chains in the complexes with H5N1-NA and N9-NA, as given in Table I.

TABLE I. The binding free energies and the AM1 net charges of the side chains of various ligands in the complexes

Model	Ligand	$\Delta G_{\text{binding}}$ kcal mol <sup>-1</sup>	Charge (e)		
			Amide/-OH side chain	-NH side chain	Glycerol/ether/alkyl side chain
H5N1-NA	Zanamivir	-6.80	+1	-17	-23
	Oseltamivir	-7.47	-6	-17	-33
	DANA	-7.49	-3	-15	-7
	Peramivir	-7.82	-18	-15	-36
N9-NA	Zanamivir	-6.51	-19	-17	-21
	Oseltamivir	-6.63	-6	-17	-33
	Peramivir	-7.23	-10	-17	-34
	DANA	-7.97	-3	-17	-25

Comparison of the efficacies of ZMV, OTV and PMV against N1 and N9 NAs was previously reported in the literature.<sup>23</sup> The ranges of experimental  $IC_{50}$  (nm) values for N1-NA were 5.8–19.7 for ZMV, 36.1–53.2 for OTV and 2.6–3.4 for PMV, while those for N9-NA were 10.4–11.5 for ZMV, 9.5–17.7 for OTV and 0.9–1.6 for PMV.<sup>23</sup> The trend of the experimental  $IC_{50}$  values for N9-NA is in agreement with that of the calculated binding free energies (Table I). In contrast, the trend of the experimental  $IC_{50}$  values for ZMV and OTV bound to N1-NA slightly deviates from that of the binding free energies (Table I).

The -NHAc group of OTV makes only one polar contact with Glu197 in N9-NA, while it makes two polar contacts with Arg70 and Glu196 in H5N1-NA (Fig. 4). By focusing on the positions of the -O-R and -NH<sub>2</sub> side chains of OTV in N9-NA with respect to those in H5N1-NA, OTV docked into N9-NA is rotated by 180° relative to that docked into H5N1-NA, thus enabling the -NH<sub>2</sub> group to make two electrostatic interactions with Tyr262 and Tyr320 in H5N1-NA (Fig. 4). By noting the particular locations of Arg74, Arg70, and Glu37 in H5N1-NA relative to those of Arg75, Arg71, and Glu38 in N9-NA (Fig. 4), the OTV flip in H5N1-NA relative to N9-NA is also associated with active-site amino-acid reorientation. While the -O-R group of OTV makes an electrostatic interaction with Tyr324 in N9-NA, it does not make any contact with the active-site residues in H5N1-NA. Since the -O-R group of OTV is capable of rotating around the single bond

between the oxygen and alkyl chain R, it inclines to adapt itself and take a comfortable position relative to its environment. In this context, noteworthy is the structure of OTV docked into the active site of H5N1-NA (Fig. 5) and N9-NA (Fig. 6), respectively. A pocket containing residues Arg144, Glu197, and Ala166 is present in the complex of N9-NA, while the pocket is spoiled in the complex of H5N1-NA.

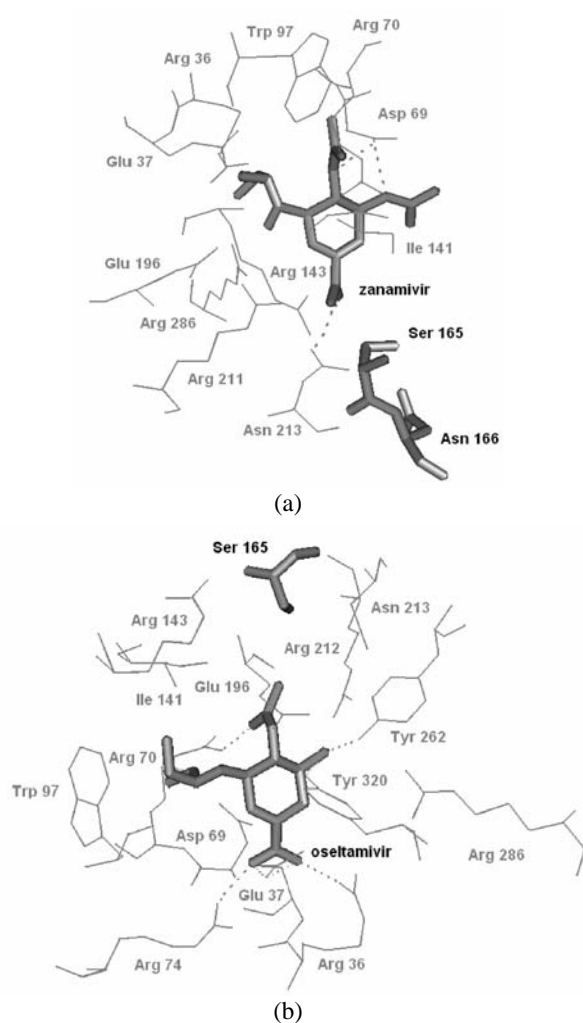
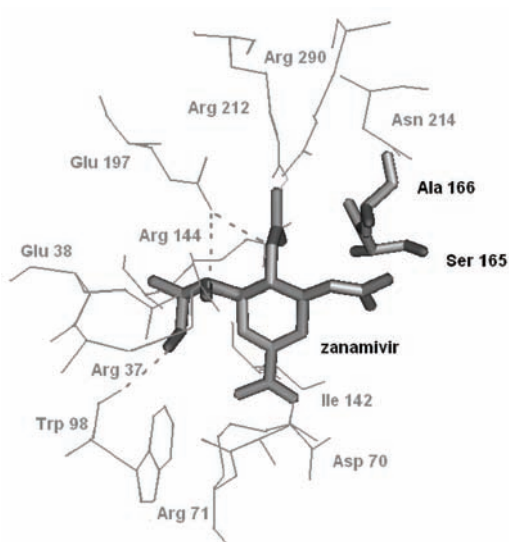
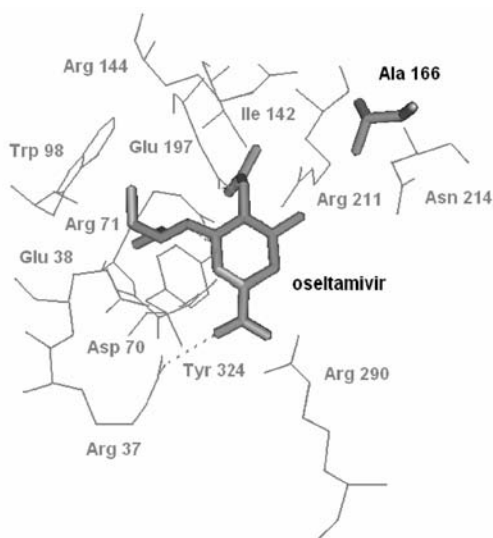


Fig. 5. The structures of zanamivir (a) and oseltamivir (b) docked into the active site of H5N1-NA.

In the case of OTV, which has been much more widely used than ZMV, a viable resistant influenza virus mutant has emerged.<sup>24</sup> This oseltamivir resistant virus remains sensitive to zanamivir, a drug derived from the naturally occurring sialic acid Neu5Ac with negligible additional functionalization.<sup>24</sup> ZMV can also



(a)



(b)

Fig. 6. The structures of zanamivir (a) and oseltamivir (b) docked into the active site of N9-NA.

be viewed as an inhibitor derived from DANA,<sup>11</sup> in which a hydroxyl group on C4 is substituted by a guanidino group (Fig. 1). The binding of ZMV and DANA to either H5N1-NA or N9-NA was considered to be very comparable in terms of electrostatic interactions made with the NA active sites.<sup>6</sup> By having a five-membered instead of a six-membered ring, peramivir is structurally different from ZMV, DANA and OTV (Fig. 1). For all these reasons, it is interesting to quantitatively compare the binding of the four inhibitors to H5N1-NA and N9-NA (Table I).

The binding free energies of ZMV, OTV, DANA, and PMV docked into H5N1-NA are  $-6.80$ ,  $-7.47$ ,  $-7.49$  and  $-7.82$  kcal mol<sup>-1</sup>, respectively. The binding free energies of ZMV, OTV, PMV, and DANA docked into N9-NA are  $-6.51$ ,  $-6.63$ ,  $-7.23$  and  $-7.97$  kcal mol<sup>-1</sup>, respectively. Note that all the inhibitor/H5N1-NA or N9-NA binding free energies are similar to each other, *i.e.*, within 1.00 or 1.45 kcal mol<sup>-1</sup>. Two previous observations,<sup>5</sup> based on a computational model of H5N1-NA, that N1–ligand binding is less potent than N9–ligand binding and that the binding free energies of the zanamivir–N1/N9 complexes are lower than those of the oseltamivir–N1/N9 complexes, do not seem to hold fast herein (Table I). The charge distribution was evaluated using the semi-empirical AM1 method. The total net charges of the –NH side chain of ZMV, OTV, and DANA are almost equal ( $-17$  e) in all the complexes. The total net charges,  $-23$  and  $-21$  e, of the glycerol side chain of ZMV in the ZMV–N1/N9 complexes are less negative than those of the ether side chain of OTV in the OTV–N1/N9 complexes ( $-33$  e). It is interesting to observe that the total net charge ( $-6$  e) of the amide side chain of OTV in OTV–N1 is more negative than that ( $+1$  e) of ZMV in ZMV–N1. In contrast to this, the total net charge ( $-6$  e) of the amide side chain of OTV in OTV–N9 is less negative than that ( $-19$  e) of ZMV in ZMV–N9. These trends of the AM1 charges of the ZMV and OTV side chains in the complexes disagree with those previously reported in the literature.<sup>5</sup> The present analysis indicates that a major difference between ZMV/OTV bound to either H5N1-NA or N9-NA is reflected through the net charges of their glycerol/ether and amide/amide side chains. In addition, Table I indicates that a main difference between ZMV bound to H5N1-NA and ZMV bound to N9-NA is reflected through the net charges of the amide side chains of ZMV. This might indicate that potential modifications of the ZMV amide side chain could lead towards the design of novel NA inhibitors with a strong resemblance to the natural substrate sialic acid. Since the oseltamivir resistant virus remains sensitive to zanamivir,<sup>1,24</sup> maintaining a strong resemblance to the natural substrate might reduce the possibility of developing viable drug-resistant mutants.

An interesting question to be elucidated is: how does the previously established, subtle variation between lipophilic and hydrophilic environments in H5N1-NA with respect to N9-NA influence the binding of ZMV and OTV to H5N1-NA and N9-NA? As shown in Fig. 3, the lipophilic Ala261 and Tyr262 (hydrophilic Ser165 and Asn166) in H5N1-NA complexed with OTV correspond to the hydrophilic Asn265 and Asn266 (lipophilic Ala166 and Thr167) in N9-NA complexed with OTV. Thus, the structures of zanamivir and oseltamivir docked into the active sites of H5N1-NA and N9-NA are shown in Figs. 5 and 6, respectively. Note the presence of Ser165 and Asn166 in the H5N1-NA active site of ZMV, while only Ser165 is present in the H5N1-NA active site of OTV. By focusing on the particular positions of Ser165 (Fig. 5), a clear reorientation of the

H5N1-NA active site residues of OTV relative to those of ZMV may be ascribed to both the presence/absence of Asn166 in the active cavity of ZMV/OTV and the -O-R side chain of OTV, which is able to rotate around the single O-R bond. Note also the presence of Ser165 and Ala166 in the N9-NA active site of ZMV, while only Ala166 is present in the N9-NA active site of OTV. By focusing on the particular positions of Ala166 (Fig. 6), a clear reorientation of the N9-NA active site residues of OTV relative to those of ZMV may be ascribed to both: the presence/absence of Ser165 in the active cavity of ZMV/OTV and the -O-R side chain of OTV, that is able to rotate around its single O-R bond.

#### CONCLUSION

Neuraminidases (NA) homology models of good stereochemical quality have been shown to be a valuable means of revealing the secret associated with the high resistance of some H5N1 strains to the commercial drugs ZMV and OTV. Thus, subtle conformational differences underlying the binding of ZMV and OTV to either H5N1-NA or N9-NA were detected. The conformational differences were shown to be more quantitatively reflected through the side chain charges of ZMV and OTV than through the binding free energies of their complexes. In this way, the previous experience that an oseltamivir-resistant virus remains sensitive to zanamivir, a drug derived from the naturally occurring sialic acid Neu5Ac with slight functional modifications, was addressed. This might provide a more profound impact on reducing the possibility of developing viable drug-resistant mutants.

#### SUPPLEMENT

Supplementary material (PDB files of the H5N1-NA and N9-NA structural models) is available upon request to authors.

*Acknowledgment.* This work was supported by Grant No. 143016B from the Ministry of Science and Technological Development of the Republic of Serbia.

#### ИЗВОД

#### НОВИ УВИДИ У МЕХАНИЗМЕ ВЕЗИВАЊА ОСЕЛТАМИВИРА И ЗНАМИВИРА СА НЕУРАМИНИДАЗАМА Н5Н1 И Н9 ВИРУСА ГРИПА: СТУДИЈА НА БАЗИ ХОМОЛОГНОГ МОДЕЛИРАЊА И МОЛЕКУЛАРНОГ ДОКИНГА

МАРИЈА Л. МИХАЈЛОВИЋ<sup>1,2</sup> И ПЕТАР М. МИТРАШИНОВИЋ<sup>2</sup>

<sup>1</sup>Факултет за физичку хемију, Универзитет у Београду, Студентски брџ 12-16, 11000 Београд и

<sup>2</sup>Институт за мултидисциплинарна истраживања, Кнеза Вишеслава 1, 11030 Београд

У контексту недавне опасности од ширења вируса птичијег грипа Н5Н1, нови увиди у механизме везивања различитих инхибитора (занамивир-ZMV, оселтамивир-OTV, DANA, перамивир-PMV) са неураминидазама (NA) су од виталне важности за структурно дизајнирање нових антивирусних лекова. Да би се обезбедили ови увиди, тродимензионални модели неураминидаза Н5Н1 и Н9 су генерисани путем хомологног моделовања. Традиционалне аминокиселине које су присутне у везивним местима целе фамилије неураминидаза су такође конзервисане у Н5Н1. Установљена је суптилна варијација липофилног и хидрофилног

окружења у H5N1 у поређењу са N9, чиме се даје допринос даљем разјашњењу високе резистенције вируса H5N1 на инхибиторе неураминидаза. На бази хомологних модела урађен је флексибилан докинг применом ArgusLab4/ASkoг протокола. Конформационе разлике између OTV везаног за H5N1-NA и везаног за N9-NA су структурно идентификоване и квантификоване. Разлика у везивној слободној енергији, која је мања од  $1 \text{ kcal mol}^{-1}$  за OTV–H5N1/N9-NA комплексе, у сагласности је са експерименталном вредности из литературе. Такође конформационе разлике између ZMV и OTV везаних за H5N1-NA и N9-NA су идентификоване. Везивне слободне енергије за занамивирове комплексе које су незнатно више у односу на вредности за оселтамивирове комплексе нису у сагласности са претходним вредностима из литературе које су базиране на хомоложном моделовању. Предложено је да се ове разлике између ZMV и OTV могу објаснити присуством/одсуством аминокиселине Asp166 у везивном месту ZMV/OTV са H5N1-NA, као и присуством/одсуством аминокиселине Ser165 у везивном месту ZMV/OTV са N9-NA. Дистрибуција наелектрисања је процењена применом полумемпиријског AM1 метода. Трендови наелектрисања бочних ланаца занамивирира и оселтамивирира у комплексима се разликују од претходно објављених трендова.

(Примљено 2. априла, ревидирано 21. октобра 2008)

#### REFERENCES

1. M. Von Itzstein, *Nature Reviews Drug Discovery* **6** (2007) 967
2. R. J. Russell, L. F. Haire, D. J. Stevens, P. J. Collins, Y. P. Lin, G. M. Blackburn, A. J. Hay, S. J. Gamblin, J. J. Skehel, *Nature* **443** (2006) 45
3. Y. Liu, J. Zhang, W. Xu, *Current Med. Chem.* **14** (2007) 2872
4. C. Sangma, S. Hannongbua, *Current Computer-Aided Drug Design* **3** (2007) 113
5. P. Nimmanpipug, J. Jitnom, C. Ngaojampa, S. Hannongbua, V. S. Lee, *Molec. Simul.* **33** (2007) 487
6. D.-Q. Wei, Q.-S. Du, H. Sun, K.-C. Chou, *Biochem. Biophys. Res. Commun.* **344** (2006) 1048
7. O. Aruksakunwong, M. Malaisree, P. Decha, P. Sompornpisut, V. Parasuk, S. Pianwanit, S. Hannongbua, *Biophys. J.* **92** (2007) 798
8. M. Mase, K. Tsukamoto, T. Imada, K. Imai, N. Tanimura, K. Nakamura, Y. Yamamoto, T. Hitomi, T. Kira, T. Nakai, M. Kiso, T. Horimoto, Y. Kawaoka, S. Yamaguchi, *Virology* **332** (2005) 167
9. G. M. Air, R. G. Webster, P. M. Colman, W. G. Laver, *Virology* **160** (1987) 346
10. (a) N. Guex, M. C. Peitsch, *Electrophoresis* **18** (1997) 2714; (b) T. Schwede, J. Kopp, N. Guex, M. C. Peitsch, *Nucleic Acids Res.* **31** (2003) 3381; (c) N. Guex, A. Diemand, T. Schwede, M. C. Peitsch, *Swiss-Model 3.5: An Automated Comparative Protein Modeling Server*, <http://www.expasy.org/swissmod/SWISS-MODEL.html> (2008)
11. B. J. Smith, P. M. Colman, M. Von Itzstein, B. Danylec, J. N. Varghese, *Protein Sci.* **10** (2001) 689
12. J. W. Ponder, *Tinker Molecular Modeling Package*, <http://dasher.wustl.edu/tinker> (2004)
13. J. W. Ponder, *Force Field Explorer 4.2: A Graphical User Interface to Tinker*, <http://dasher.wustl.edu/tinker> (2004)
14. J. Wang, P. Cieplak, P. A. Kollman, *J. Comput. Chem.* **21** (2000) 1049
15. R. A. Laskowski, M. W. MacArthur, D. S. Moss, J. M. Thornton, *J. Appl. Cryst.* **26** (1993) 283
16. A. L. Morris, M. W. MacArthur, E. G. Hutchinson, J. M. Thornton, *Proteins* **12** (1992) 345
17. W. L. DeLano, *PyMol™ 0.97*, DeLano Scientific LLC, San Carlos, CA, 2004.

18. M. A. Thompson, *ArgusLab 4.0*, Planaria Software LLC, Seattle, NY, 2004.
19. W. J. Brouillette, S. N. Bajpai, S. M. Ali, S. E. Velu, V. R. Atigadda, B. S. Lommer, J. B. Finley, M. Luo, G. M. Air, *Bioorg. Med. Chem.* **11** (2003) 2739
20. C. U. Kim, W. Lew, M. A. Williams, H. Wu, L. Zhang, X. Chen, P. A. Escarpe, D. B. Mendel, W. G. Laver, R. C. Stevens, *J. Med. Chem.* **41** (1998) 2451
21. T. Wang, R. C. Wade, *J. Med. Chem.* **44** (2001) 961
22. A. R. Ortiz, M. T. Pisabarro, F. Gago, R. C. Wade, *J. Med. Chem.* **38** (1995) 2681
23. E. A. Govorkova, I. A. Leneva, O. G. Goloubeva, K. Bush, R. G. Webster, *Antimicrob. Agents Chemother.* **45** (2001) 2723
24. Q. M. Le, M. Kiso, K. Someya, Y. T. Sakai, T. H. Nguyen, K. H. L. Nguyen, N. D. Pham, H. H. Ngyen, S. Yamada, Y. Muramoto, T. Horimoto, A. Takada, H. Goto, T. Suzuki, Y. Suzuki, Y. Kawaoka, *Nature* **437** (2005) 1108.





www.shd.org.rs

J. Serb. Chem. Soc. 74 (1) 15–25 (2009)

JSCS–3804

JSCS@tmf.bg.ac.yu • www.shd.org.rs/JSCS

UDC 547.533:541.124:577.15+547.96:611.018.5

Original scientific paper

## The effect of toluene on oxidative processes in rat blood

SILVANA S. STAJKOVIĆ<sup>1</sup>, SUNČICA Z. BOROZAN<sup>2\*</sup> and  
GORDANA GAĐANSKI-OMEROVIĆ<sup>3</sup>

<sup>1</sup>Department of Food Hygiene and Technology, <sup>2</sup>Department of Chemistry and  
<sup>3</sup>Department of Biochemistry, Faculty of Veterinary Medicine, University of Belgrade,  
Bulevar Oslobođenja 18, 11000 Belgrade, Serbia

(Received 19 February, revised 10 June 2008)

**Abstract:** This study was designed to investigate the effects of toluene treatment on oxidative stress in rat blood. Since toluene metabolism produces reactive oxygen and nitrogen species, it was hypothesized that the toluene treatment would: 1) provoke changes in the activities of antioxidant enzymes, 2) impair the integrity of the cell membrane and 3) induce structural changes in the plasma proteins. Female Wistar rats were treated with toluene intraperitoneally, at a daily dose of 0.38 mmol/kg body weight for 12 days, and 5 mmol/kg body weight for 6 days, respectively, with propylene glycol as the carrier. Toluene significantly increased superoxide dismutase activity at low doses, catalase activity at high doses and the level of erythrocytes malondialdehyde in both treated groups when compared to the control group. The nitrite ( $\text{NO}_2^-$ ) level in both treated groups was not different from that in the control animals. Toluene caused oxidative modification of plasma proteins and, consequently, changes in the concentration of glycoproteins and lipoproteins when compared to the control group. The observed alterations indicate that toluene treatment might be involved in free radical processes.

**Keywords:** toluene; free radicals; antioxidant enzymes; protein modification.

### INTRODUCTION

Toluene is an organic solvent widely used in industry. During the process of its biotransformation, reactive intermediary products (aryl oxides),<sup>1–3</sup> reactive oxygen species (ROS), including the superoxide anion ( $\text{O}_2^{\bullet-}$ ), the hydroxyl radical ( $\text{OH}^\bullet$ ) and hydrogen peroxide<sup>2</sup> and reactive nitrogen species (RNS), including the nitrosyl radical ( $\text{NO}^\bullet$ ),<sup>4</sup> could be formed.  $\text{O}_2^{\bullet-}$  in reaction with NO generates peroxynitrite ( $\text{ONOO}^-$ ), which can cause extensive cell damage through peroxidation of lipids.<sup>5</sup> The reactive  $\text{O}_2^{\bullet-}$  is converted into less toxic  $\text{H}_2\text{O}_2$  by superoxide dismutase (SOD).  $\text{H}_2\text{O}_2$  may be converted to  $\text{H}_2\text{O}$  either by catalase

\* Corresponding author. E-mail: sborozan@vet.bg.ac.yu

doi: 10.2298/JSC0901015S

(CAT) or glutathione peroxidase. It may generate the highly reactive free HO• *via* a Fenton reaction, which is believed to be responsible for oxidative damage.<sup>6</sup> HO• leads to peroxidation of polyunsaturated fatty acids (PUFAs), the constituents of cell and organelle membranes. In the terminal phase of lipid peroxidation (LPO), malondialdehyde (MDA) is produced, as one of the products of degradation of PUFAs.<sup>7,8</sup> Exposure of proteins to HO•, O<sub>2</sub><sup>•-</sup> or both leads to gross structural modifications.<sup>9</sup> Oxidative damage of plasma proteins commonly occurs *via* reaction with small reactive aldehydes or with aldehydes derived specifically from LPO, such as MDA,<sup>8</sup> leading to the accumulation of heterogeneous protein modifications, classified as advanced glycation end-products (glycoproteins) or advanced lipidation end products (lipoproteins).<sup>10,11</sup>

Toluene promotes the state of oxidative stress,<sup>4</sup> by exhaustion of the anti-oxidative defense enzymes. Hence, it was hypothesized that toluene treatment would: 1) provoke changes in the activities of the anti-oxidant enzymes, 2) induce the process of LPO and 3) lead to oxidative modifications of plasma proteins.

Previous studies suggest that toluene may be toxic to humans at concentrations lower than the toluene threshold limit value (*TLV*) (50 ppm) recommended by the American Conference of Governmental Industrial Hygienists (ACIGH).<sup>12</sup> It was, therefore, important to investigate the influence of toluene at the concentrations lower and higher than the *TLV*. In this study, the resulting processes in the blood of rats exposed to toluene were investigated.

## EXPERIMENTAL

All the used chemicals were of reagent grade, purchased from Merck (Darmstadt, Germany).

### *Animals*

Adult female Wistar rats (180–220 g) were housed in stainless steel grid-bottom cages, with free access to food and water. They were maintained under constant conditions (12 h light–dark cycles, temperature 22±2 °C). The study was conducted in compliance with the EEC Directive 86/609 and was approved by the Ethics Committee of the Faculty of Veterinary Medicine, the University of Belgrade.

### *Toluene treatments*

Twelve rats were randomly assigned to each group. The animals were treated daily, at 9 am, by injection of propylene glycol intraperitoneally (i.p.) (vehicle control, group I), or toluene, at a dose of 0.38 mmol/kg body weight (bw) for 12 days (low dose, group II), a concentration lower than the toluene *TLV*, and at a dose of 5 mmol/kg bw for 6 days (high dose, group III), a concentration higher than the toluene *TLV*. The i.p. route enables the maximal absorption of toluene. The rats were killed by diethyl ether inhalation 24 h after the last administration.

Blood (6–8 ml) was obtained from the *aorta abdominalis* and collected in tubes containing Na citrate (3.8 % w/v) as anticoagulant. The erythrocytes were separated by centrifugation (3000 rpm) and washed three times in saline solution, followed by the immediate assessment of the enzyme activities.

### *Erythrocyte enzymes activities*

The CAT activity was determined by the method of Aebi.<sup>13</sup> The decrease in H<sub>2</sub>O<sub>2</sub> was measured spectrophotometrically at 240 nm (Cecil CE 2021 UV/Vis). One unit of CAT activity was defined as the activity required to degrade 1.0 μmol H<sub>2</sub>O<sub>2</sub> in 60 s at 25 °C and pH 7.0. The activity is expressed as 10<sup>4</sup> μM min<sup>-1</sup> (g Hb)<sup>-1</sup>.

The SOD activity was determined using a Superoxide Assay Kit (Calbiochem), which utilizes 5,6,6a,11b-tetrahydro-3,9,10-trihydroxybenzyl[*c*]fluorene. This reagent undergoes alkaline auto-oxidation, which is accelerated by SOD. The auto-oxidation of this reagent was measured at 525 nm (Cecil CE 2021 UV/Vis). The SOD activity is expressed as U (g Hb)<sup>-1</sup>.

The SOD isoenzymes (SOD1 and SOD2) were separated on discontinuous polyacrylamide gels according to Beauchamp and Fridovich.<sup>14</sup>

The LPO in erythrocytes was quantified by measuring the formation of thiobarbituric acid reactive substances (TBARS) by the method of Stock and Dormondy,<sup>15</sup> and is expressed in nmol MDA (g Hb)<sup>-1</sup>.

The total Hb content was measured by the cyanmethemoglobin method of Salvati and Tentori.<sup>16</sup>

The NO<sub>2</sub><sup>-</sup> levels were analyzed by ELISA assay, using Griess reagent by the method of Guevara.<sup>17</sup> The absorbance was measured using a microplate reader (Plate reader, Mod. A1, Nubenco Enterprises, Inc.) at a wavelength of 545 nm. The results are expressed as μM L<sup>-1</sup>.

### *Native polyacrylamide gel electrophoresis (PAGE)*

Plasma proteins were analyzed by native PAGE (8 %) according to the method of Laemmli.<sup>18</sup> The native PAGE (8 %) of glycoproteins and lipoproteins were performed according to Hames and Rickwood<sup>19</sup> and Laemmli.<sup>18</sup> The glycoproteins and lipoproteins bands were stained using Pas Schiff's reagent<sup>19,20</sup> and Amido Black,<sup>21</sup> respectively. The electrophoretic analyses were performed on a vertical device Mini Ve Hoffer (LKB 2117, Bromma, Uppsala, Sweden).

The band intensities of the isoenzymes of SOD, plasma proteins, glycoproteins and lipoproteins were estimated using Scion Image Beta 4.02 software (<http://www.scioncorp.com>).<sup>22</sup> The density of each band was estimated with respect to the total area. Data are expressed as percentages of the total protein area.

The plasma protein concentration was determined spectrophotometrically according to Lowry.<sup>23</sup>

### *Statistical analyses*

Data are expressed as the means ± standard deviation (*SD*). Statistical significance was tested by the one-way Anova, followed by Dunnett's *t*-test. The minimum level of statistical significance was set to *p*<0.05.

## RESULTS

The changes in the SOD and CAT activities and the MDA levels in the erythrocytes are presented in Figs. 1–3, respectively. Toluene treatment at the low dose (0.38 mmol/kg bw) significantly increased the total SOD activity (Fig. 1a), as well as the isoenzyme SOD1 and SOD2 activity, 50.90, 52.21 and 130 %, respectively (Fig. 1b and 1c), when compared to the control group. The MDA levels also significantly increased 43.69 % upon treatment (*p* < 0.05). There is a tendency towards an increase in the CAT activity. The high dose of toluene (5 mmol/kg bw) induced the CAT activity (*p* < 0.001) and MDA levels (*p* < 0.05)

by 34.07 and 50.96 %, respectively. No differences in activity of the total SOD, SOD1, and SOD2 were observed among treated animals in comparison with the control group.

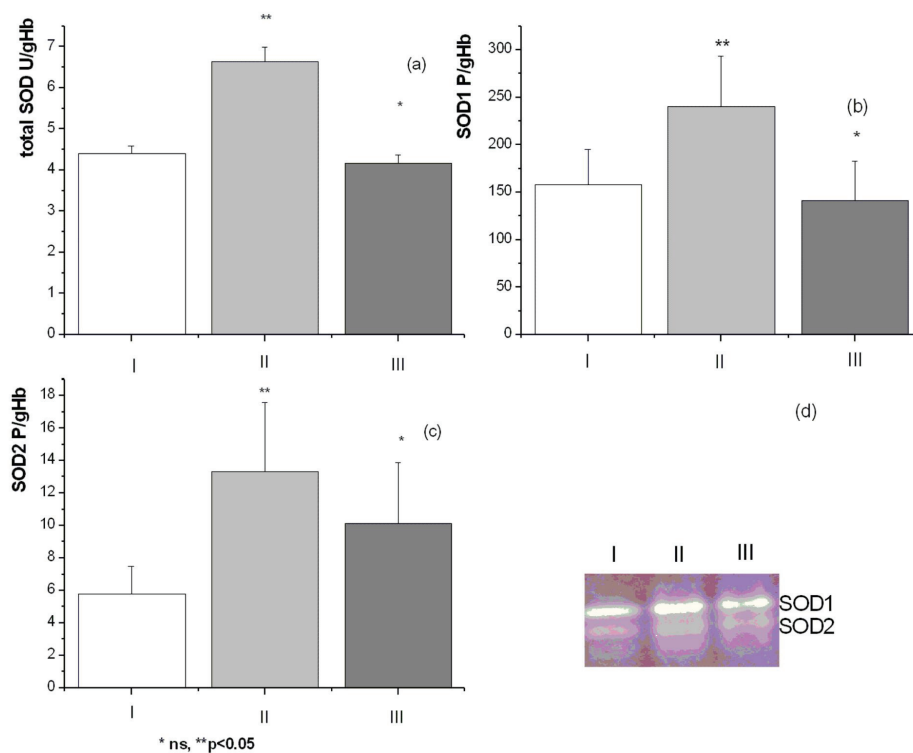


Fig. 1. Activity of SOD: total activity of SOD (a), activity of isoenzyme SOD1 (b), SOD2 (c) and activity of SOD on native PAGE (d); I – control group, II – rats treated i.p. with toluene at doses of 0.38 mM/kg bw and III – rats treated i.p. with toluene at doses of 5.00 mM/kg bw.

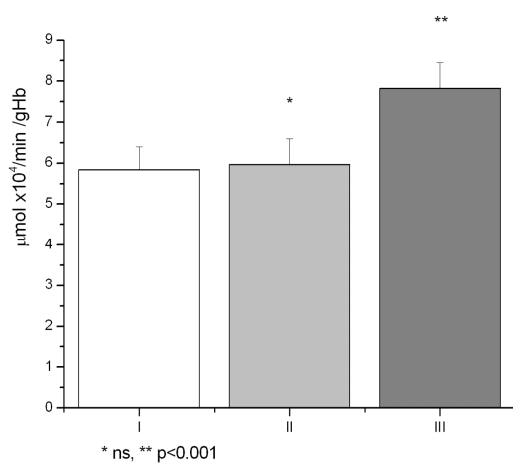


Fig. 2. CAT activities: I – control group, II – rats treated i.p. with toluene at doses of 0.38 mM/kg bw and III – rats treated i.p. with toluene at doses of 5.00 mM/kg bw.

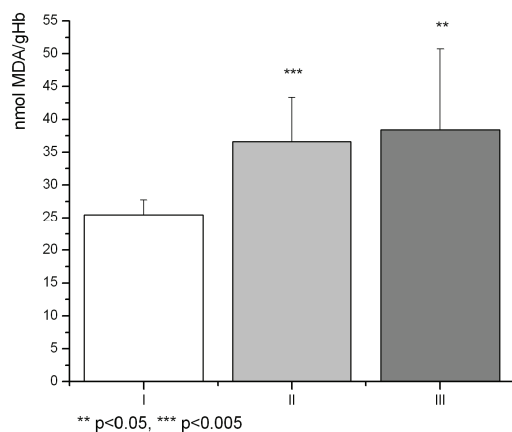


Fig. 3. Levels of erythrocytes MDA: I – control group, II – rats treated i.p. with toluene at doses of 0.38 mM/kg bw and III – rats treated i.p. with toluene at doses of 5.00 mM/kg bw.

The changes in the  $\text{NO}_2^-$  levels and total protein content of the control and the exposed groups of rats in blood plasma are presented in Figs. 4 and 5, respectively. Toluene treatment at the low dose decreased the  $\text{NO}_2^-$  levels ( $p > 0.05$ ) and total protein content ( $p < 0.05$ ) by 8.10 % compared to the non-treated animals. The high dose of toluene significantly decreased the total protein content ( $p < 0.05$ ) by 9.46 % compared to the control group. The observed decrease in the  $\text{NO}_2^-$  levels was not statistically significant.

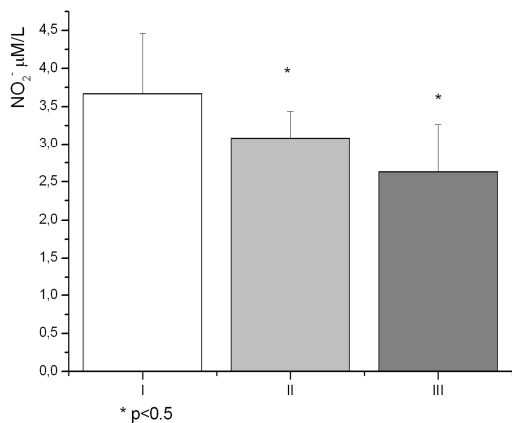


Fig. 4. Content of  $\text{NO}_2^-$ : I – control group, II – rats treated i.p. with toluene at doses of 0.38 mM/kg bw and III – rats treated i.p. with toluene at doses of 5.00 mM/kg bw.

The plasma proteins, glycoproteins and lipoproteins were separated by native PAGE and the results of the quantitative analysis of the gel bands are given in Tables Ia, Ib and Ic as percentages of the total area. Seven major protein fractions of plasma proteins are presented in Table Ia. The content of glycoproteins and lipoproteins are given in Table Ib and Ic, respectively.

Toluene treatment induced changes in the concentrations of plasma proteins (Table Ia). Toluene treatment at the low dose significantly increased the concentration of alpha-1 glycoprotein ( $p < 0.001$ ) and decreased the concentration of albumin ( $p < 0.001$ ) by 37.05 and 12.02 %, respectively, compared to the control

group. Toluene treatment at the high dose significantly increased the content of alpha-1 ( $p < 0.05$ ), alpha-2 glycoprotein and haptoglobin ( $p < 0.001$ ) by 23.11, 67.96 and 101 %, respectively, and decreased albumin ( $p < 0.001$ ) by 27.27 % compared to the values for the control animals. The albumin to globulin ratio (A/G) decreased in both groups ( $\approx 1.36$  fold for the low dose group, and  $\approx 1.91$  fold for the high dose group) compared to the control group.

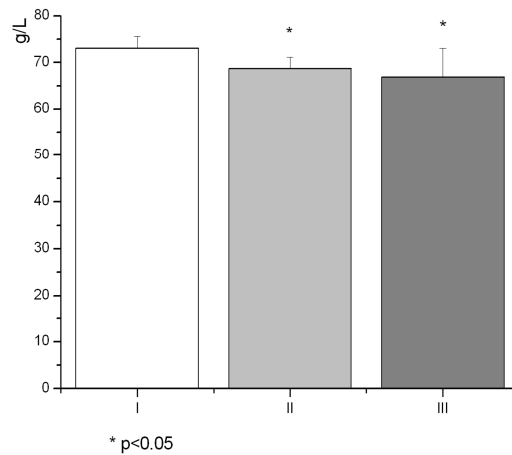


Fig. 5. Total content of plasma proteins: I – control group, II – rats treated i.p. with toluene at doses of 0.38 mM/kg bw and III – rats treated i.p. with toluene at doses of 5.00 mM/kg bw.

TABLE Ia. The results of quantitative analysis of gel bands of plasma proteins expressed as mean  $\pm$ SD for: I – control group, II – rats treated i.p. with toluene at doses of 0.38 mM/kg bw, and III – rats treated i.p. with toluene at doses of 5.00 mM/kg bw

Group	Total area, % (mean $\pm$ SD)							A/G
	Albumin	Alpha-1	Alpha-2	Transferrin	Haptoglobin	Gamma 1	Gamma2	
I	55.16 $\pm 3.8$	48.53 $\pm 1.07^a$	40.19 $\pm 3.72^a$	8.16 $\pm 1.49$	6.37 $\pm 0.79$	4.40 $\pm 0.73$	3.91 $\pm 1.06$	1.28 $\pm 0.52$
II	11.12 $\pm 1.26$	15.24 $\pm 1.73^a$	13.69 $\pm 0.66^b$	9.08 $\pm 0.70$	6.77 $\pm 1.27$	4.81 $\pm 1.47$	3.43 $\pm 0.83$	0.94 $\pm 0.15$
III	5.15 $\pm 1.62$	6.65 $\pm 1.35$	18.65 $\pm 2.36^a$	9.12 $\pm 0.85$	12.81 $\pm 2.28^a$	4.44 $\pm 1.50$	3.26 $\pm 0.91$	0.67 $\pm 0.22$

TABLE Ib. The results of quantitative analysis of gel bands of glycoproteins expressed as mean  $\pm$ SD for: I – control group, II – rats treated i.p. with toluene at doses of 0.38 mM/kg bw, and III – rats treated i.p. with toluene at doses of 5.00 mM/kg bw

Group	Total area, % (mean $\pm$ SD)					IgG
	Albumin	Alpha-1 and alpha-2	Transferrin	Beta region	Haptoglobin	
I	17.05 $\pm$ 8.40	7.79 $\pm$ 4.18	6.53 $\pm$ 3.82	16.62 $\pm$ 3.84 <sup>b</sup>	21.28 $\pm$ 6.62	19.75 $\pm$ 1.30
II	11.41 $\pm$ 8.72	13.81 $\pm$ 4.28	23.03 $\pm$ 4.59 <sup>b</sup>	22.65 $\pm$ 4.51 <sup>a</sup>	25.58 $\pm$ 6.28	13.69 $\pm$ 3.63 <sup>b</sup>
III	5.49 $\pm$ 1.59 <sup>b</sup>	11.16 $\pm$ 4.59	20.73 $\pm$ 2.65 <sup>a</sup>	24.18 $\pm$ 3.33 <sup>a</sup>	33.13 $\pm$ 6.58 <sup>b</sup>	6.11 $\pm$ 2.70 <sup>a</sup>

TABLE Ic. The results of quantitative analysis of gel bands of lipoproteins expressed as mean  $\pm$ SD for: I – control group, II – rats treated i.p. with toluene at doses of 0.38 mM/kg bw, and III – rats treated i.p. with toluene at doses of 5.00 mM/kg bw

Group	Total area, % (mean $\pm$ SD)			ApoA-HDL/ApoB-LDL
	Albumin	ApoA-HDL	ApoB-LDL	
I	19.40 $\pm$ 1.45	17.79 $\pm$ 2.05	26.04 $\pm$ 5.79b	1.75 $\pm$ 0.64
II	23.96 $\pm$ 3.51	17.62 $\pm$ 5.94	5.43 $\pm$ 2.39a	3.41 $\pm$ 0.90
III	41.87 $\pm$ 5.46	60.09 $\pm$ 6.61a	45.02 $\pm$ 4.63b	8.34 $\pm$ 0.52

<sup>a</sup> $p < 0.001$ ; <sup>b</sup> $p < 0.05$

Toluene treatment induced changes in the content of glycoproteins (Table Ib) and lipoproteins (Table Ic). Statistical analysis of the glycoproteins revealed a significantly increased transferrin content ( $p < 0.05$ ,  $\approx 65\%$ ) and the amount of proteins of the beta region ( $p < 0.001$ ,  $>85\%$ ) and decreased the IgG content in both groups compared to the control group (Table Ib). Toluene treatment with high dose increased the alpha-1 and alpha-2 glycoproteins and haptoglobin ( $p < 0.05$ ) by 113 and 55.69%, respectively, and decreased albumin ( $p < 0.05$ ) by 67.80% in comparison to the control group.

The low dose of toluene given along a period of 12 days significantly increased the level of the apoB-LDL lipoprotein fraction ( $p < 0.001$ ) by 43.52% and non-significantly decreased the level of the ApoA-HDL lipoprotein fraction ( $p < 0.1$ ), whilst toluene treatment with the high dose significantly increased level of ApoB-LDL and albumin ( $p < 0.05$ ) by 7.52 and 36.00%, respectively, and decreased the level of ApoA-HDL ( $p < 0.001$ ) by 77.34%, compared to the control group. The ratio ApoA-HDL/ApoB-LDL increased in both groups ( $\approx$  two-fold for the low dose and  $\approx$  five-fold for the high dose group) compared to the control group (Table Ic).

## DISCUSSION

Toluene is a lipophilic agent and therefore absorbed and retained well by the lipid rich areas in organisms.<sup>24</sup> Toluene and its metabolites cause a significant elevation in the rate of ROS generation.<sup>2</sup> The interplay between ROS and antioxidant defense in living aerobic organisms is connected with a series of intracellular antioxidant enzymes, the roles of which are to intercept and inactivate reactive radicals. CAT scavenges an excess of free radicals *via* enzymatic and chemical mechanisms, which results in depletion of H<sub>2</sub>O<sub>2</sub>. This study showed significantly increased CAT activities in rats treated with toluene at the high dose. This increase could be attributed to the production of ROS provoked by toluene. The ROS scavenging activity of SOD is effective only when it is followed by the action of CAT, since the dismutase activity of SOD generates H<sub>2</sub>O<sub>2</sub> from O<sub>2</sub><sup>•-</sup>.<sup>25</sup> The increased concentration of H<sub>2</sub>O<sub>2</sub> and CAT activity in rats treated with toluene at the high dose, which appears to inhibit some protective enzymes including SOD, allows the production of HO<sup>•</sup>, formed in Fenton and Haber-

-Weiss reactions.<sup>26</sup> The HO• radicals lead to peroxidation of PUFAs and MDA is produced in the terminal phase of LPO. MDA has been mainly employed as a marker of oxidative stress in both *in vitro* and *in vivo* studies.<sup>7,8,27</sup> In the present study, toluene significantly increased the erythrocytes MDA levels in both treated groups.

Organic solvents (toluene and benzene) and their metabolites induced the formation of RNS<sup>28,29</sup> and enhanced the expression of inducible nitric oxide synthase (iNOS), which can lead to the formation of excessive NO•.<sup>30</sup> The present results showed that there were no significant changes in the level of NO<sub>2</sub><sup>-</sup> in plasma of both toluene treated groups. The reason possibly lies in the difference in the toluene concentration and, consequently, the difference in NO• release and the higher reactivity of NO• with toluene metabolites<sup>31</sup> and cellular macromolecules. The combination of NO• and O<sub>2</sub><sup>-</sup> also results in the rapid generation of the highly reactive molecule ONOO<sup>-</sup>.<sup>32</sup> The marker for ONOO<sup>-</sup> formation is nitration of tyrosine residues in proteins (Tyr(NO<sub>2</sub>)). Tyr(NO<sub>2</sub>) is a post-translational modification associated with oxidative stress.<sup>29</sup>

Oxidative damage of plasma proteins can be induced directly *via* H<sub>2</sub>O<sub>2</sub>, *via* xenobiotics such as CCl<sub>4</sub>, through reduced transition metals (Fe<sup>2+</sup>) and ionizing radiation,<sup>33</sup> indirectly *via* reaction with small reactive aldehydes, such as glyoxal, methylglyoxal, or with aldehydes derived specifically from LPO, such as MDA,<sup>8</sup> leading to the accumulation of heterogeneous protein modifications, which are classified as advanced glycation end products (AGEs)<sup>10,11</sup> or advanced lipidation end products (ALEs).<sup>10,11</sup> The total plasma proteins were analyzed on native PAGE to study the changes in individual protein component and changes in the A/G ratio. The level of albumin decreased but alpha-1, alpha-2 and haptoglobin increased upon toluene treatment compared to the control group. These proteins are classified as acute-phase proteins. Ceron *et al.*<sup>34</sup> showed that concentration of acute-phase proteins changes with inflammation, tissue damage, infection, certain cancers and xenobiotics. Kaukianinen found a positive correlation between blood glucose levels and toluene exposure.<sup>35</sup> An increased level of glucose leads to increased glycosilation of some of the plasma proteins (alpha-1 and alpha-2, transferrin, proteins of beta region, and haptoglobin),<sup>36</sup> as the present results also show.

The two lipoprotein subfractions responsible for cholesterol transport are low density lipoproteins (LDLs) and high density lipoproteins (HDLs).<sup>37</sup> Knezević *et al.*<sup>38</sup> showed that human exposure to toluene and xylene increases the level of plasma LDL cholesterol but substantially decreases the HDL concentration, thereby increasing the LDL/HDL ratio. The present results are in accordance with these findings. LDL binds receptors *via* protein ApoB (ApoB-LDL). Receptor-bound LDL is internalized by endocytosis into the cell. Oxidative damage of LDL could arise from a number of different causes, including free radicals, such as O<sub>2</sub><sup>-</sup> and NO•.<sup>39</sup> LDL oxidation is a progressive process leading at

first to the formation of mildly oxidized LDL, which is defined by a low content of lipid-peroxidation derivatives and slight ApoB modifications, and later to extensively oxidized LDL, which contains high levels of lipid-peroxidation products and severe ApoB alterations.<sup>40–42</sup> These severe ApoB alterations lead to the failure to bind and internalize LDL, which is probably the reason for the increased LDL levels in the plasma of the animals treated in this study. HDL particles contain molecules of apolipoprotein A1 (ApoA1-HDL). In addition to its role in reverse cholesterol transport (from peripheral tissues to the liver),<sup>43,44</sup> HDL exhibits a protective effect against the cytotoxicity of oxidized LDL, by inhibiting LDL oxidation induced by cells and inhibiting the cytotoxicity of oxidized LDL.<sup>45,46</sup> To the best of our knowledge, the mechanism of the protective effect of HDL at the cellular level is still unclear. This protective effect is impaired on account of decreased HDL levels.

#### CONCLUSIONS

The results of this study show that toluene treatment of rats (low and high dose) leads to oxidative stress caused by ROS and RNS, and consequently to the: 1) changed antioxidant enzyme activity, 2) increased LPO and impaired integrity of the cell membrane and 3) structural changes in the plasma proteins. Further studies are required to evaluate the possible molecular mechanisms of the toxicity induced by toluene exposure.

*Acknowledgement.* This study was supported by the Ministry of Science of the Republic of Serbia (Grant No. 1518).

#### ИЗВОД

#### УТИЦАЈ ТОЛУЕНА НА ОКСИДАТИВНЕ ПРОЦЕСЕ У КРВИ ПАЦОВА

СИЛВАНА С.СТАЈКОВИЋ<sup>1</sup>, СУНЧИЦА З. БОРОЗАН<sup>2</sup> И ГОРДАНА ГАЋАНСКИ-ОМЕРОВИЋ<sup>3</sup>

<sup>1</sup>Каџедра за хигијену и тешнолозију намирница анималног порекла, <sup>2</sup>Каџедра за хемију

<sup>3</sup>Каџедра за биохемију, Факултет вейеринарске медицине, Универзитет у Београду,  
Булевар Ослобођења 18, 11000 Београд

У овом раду је испитиван утицај толуена на оксидативни стрес у крви пацова. С обзиром на то да метаболизам толуена доводи до стварања реактивних кисеоничних и азотових врста, претпостављено је да третирање пацова различитим концентрацијама толуена доводи до 1) промене у активности ензима антиоксидативне одбране, 2) нарушавања интегритета ћелијске мембране и 3) структурних промена код плазма протеина. Женке пацова соја Wistar су подељене у три групе: I група – контролна, II и III група – пацови третирани i.p. толуеном свакодневно 12 и 6 дана, дозом од 0,38 mmol/kg телесне масе и 5,0 mmol/kg телесне масе. Толуен је статистички значајно повећавао активност SOD у II групи и активност CAT у III групи, док је садржај MDA био значајно повећан у обе групе у поређењу са контролном групом. Снижење NO<sub>2</sub><sup>-</sup> у обе третиране групе није било статистички значајно у односу на контролну групу. Толуен је довео до оксидативних промена плазма протеина, а самим тим и до промене концентрације глико- и липопротеина у односу на контролну групу. Доказане промене указују на то да третирање толуеном изазива слободно-радикалске процесе.

(Примљено 19. фебруара, ревидирано 10. јуна 2008)

## REFERENCES

1. R. Toftgard, O. G. Nilsen, J. A. Gustafsson, *Scand. J. Work Environ. Health* **71** (1981) 31
2. C. J. Mattia, S. F. Ali, S. C. Bondy, *Mol. Chem. Neuropathol.* **18** (1993) 313
3. T. Tabatabaie, R. A. Floyd, *Toxicol. Appl. Pharmacol.* **141** (1996) 389
4. M. Maniscalco, L. Grieco, A. Galdi, J. O. N. Landberg, M. Sofia, *Occup. Med.* **54** (2004) 404
5. A. Denicola, R. Rafael, *Toxicol.* **208** (2005) 273
6. J. M. Mates, C. Perez-Gomez, I. N. De Castro, *Clin. Biochem.* **32** (1999) 595
7. K. Uchida, *Prog. Lipid. Res.* **42** (2003) 318
8. N. Traverso, S. Menini, E. P. Maineri, S. Patriarca, P. Odetti, D. Cottalasso, U. M. Marinari, M. A. Pronzato, *J. Gerontol.* **59** (2004) 890
9. J. C. Mayo, D. X. Tan, R. M. Sainz, M. Natarajan, S. Lopez-Burillo, R. J. Reiter, *Biochim. Biophys. Acta* **1620** (2003) 139
10. A. Lapolla, D. Fedele, R. Seraglia, P. Traldi, *Mass Spectrom. Rev.* **25** (2006) 775
11. A. Odhiambo, D. H. Perlman, H. Huang, C. E. Costello, H. W. Farber, M. H. Steinberg, M. E. McComb, E. S. Klings, *Rapid Commun. Mass Spectrom.* **21** (2007) 2195
12. American Conference of Governmental Industrial Hygienists, 2006
13. H. Aebi, *Methods in Enzymology*, Academic Press, Orlando, 1984, p. 121
14. C. H. Beauchamp, I. Fridovich, *Anal. Biochem.* **44** (1971) 276
15. J. Stock, T. L. Dormandy, *Br. J. Haematol.* **20** (1971) 95
16. A. M. Salvati, L. Tentori, *Methods Enzymol.* **76** (1981) 715
17. I. Guevara, J. Iwanejko, A. Dembinska-Kiec, J. Pankiewicz, A. Wanat, P. Anna, *Clin. Chim. Acta* **274** (1998) 177
18. U. K. Laemmli, *Nature* **227** (1970) 680
19. B. D. Hames, D. Rickwood, *Gel electrophoresis of proteins*, IRL Press Oxford, Washington DC, 1985, p. 59
20. J. F. Frederick, *Gel Electrophoresis*, The Academy of Science, New York, 1964, p. 431
21. F. Gentile, E. Bali, G. Pignalosa, *Anal. Biochem.* **245** (1997) 260
22. Scion Corp., <http://www.scioncorp.com> (June, 2007)
23. O. H. Lowry, N. J. Rosebrough, A. L. Farr, R. J. Randall, *J. Biol. Chem.* **193** (1951) 265
24. O. Coskun, S. Oter, A. Korkmaz, F. Armutcu, M. Kanter, *Neurochem. Res.* **30** (2005) 33
25. Q. S. Wang, C. L. Zhang, X. L. Zhao, S. F. Yu, K. Q. Xie, *Toxicol.* **227** (2006) 36
26. J. P. Kehrer, *Toxicol.* **149** (2000) 43
27. M. Boaz, Z. Matas, A. Biro, Z. Katzir, M. Green, M. Fainaru, S. Smetana, *Kidney Int.* **56** (1999) 1078
28. O. Myhre, F. Fonnum, *Biochem. Pharmacol.* **62** (2001) 119
29. K. M. Chen, K. El-Bayoumy, J. Hosey, J. Cunningham, C. Aliaga, A. A. Melikian *Chem. Biol. Interact.* **156** (2005) 81
30. D. L. Laskin, D. E. Heck, C. J. Punjabi, J. D. Laskin, *J. Toxicol. Environ. Health* **61** (2000) 413
31. K. M. Chen, K. El-Bayoumy, J. Cunningham, C. Aliaga, H. Li, A. A. Melikian, *Chem. Res. Toxicol.* **17** (2004) 370
32. R. E. Huie, S. Padmaja, *Free Radical Res. Commun.* **18** (1993) 18195
33. S. Z. Borozan, G. N. Gadjanski-Omerovic, S. S. Stajkovic *Centr. Eur. J. Occup. Environ. Health* **10** (2004) 12
34. J. J. Ceron, P. D. Eckershall, S. Martinez-Subiela, *Vet. Clin. Pat.* **34** (2005) 85

35. A. Kaukianinen, T. Vehmas, K. Rantala, M. Nurminen, R. Martikainen, H. Taskinen, *Int. Arch. Occup. Environ. Health* **77** (2003) 39
36. S. Rahbar, *Cell Biochem. Biophys.* **48** (2007) 147
37. L. B. Nielsen, *Atherosclerosis* **143** (1999) 229
38. V. Knezević, D. Joksović, O. Knezević, *Jugoslov. Med. Biochem.* **23** (2004) 65 (in Serbian)
39. V. Z. Lankin, A. K. Tikhaze, V. I. Kapel'Ko, G. S. Shepel'kova, K.B. Shumaev, O. M. Panasenko, G. G. Konovalova, Yu. N. Belenkov, *Biochemistry* **72** (2007) 1081
40. J. L. Witztum, D. Steinberg, *J. Clin. Invest.* **88** (1991) 1785
41. J. W. Heinecke, H. Rosen, A. Chait, *J. Clin. Invest.* **4** (1984) 1890
42. H. Esterbauer, M. Dieber-Rotheneder, G. Waeg, G. Striegl, G., Jürgens, *Biochem. Chem. Res. Toxicol.* **3** (1990) 77
43. S. Eisenberg, *J. Lipid Res.* **25** (1984) 1017
44. F. Oram, S. Yokoyama, *J. Lipid Res.* **37** (1996) 2473
45. J. L. Hessler, A. L. Robertson, G. M Chisolm. *Atherosclerosis* **32** (1979) 213
46. M. I. Mackness, P. N. Durrington, *Atherosclerosis* **115** (1995) 243.





www.shd.org.rs

J. Serb. Chem. Soc. 74 (1) 27–34 (2009)  
JSCS–3805

JSCS@tmf.bg.ac.yu • www.shd.org.rs/JSCS

UDC 582.475:547.77+547.94:  
:615.28(497.11)(497.16)

Original scientific paper

## Pyrrolizidine alkaloids from seven wild-growing *Senecio* species in Serbia and Montenegro

BORIS M. MANDIĆ<sup>1</sup>, DEJAN N. GOĐEVAC<sup>2</sup>, VLADIMIR P. BEŠKOSKI<sup>2</sup>,  
MILENA R. SIMIĆ<sup>3</sup>, SNEŽANA S. TRIFUNOVIĆ<sup>2</sup>, VELE V. TEŠEVIĆ<sup>1</sup>,  
VLATKA V. VAJS<sup>2#</sup> and SLOBODAN M. MILOSAVLJEVIĆ<sup>1\*\*</sup>

<sup>1</sup>Faculty of Chemistry, Studentski trg 16, P.O. Box 158, 11000 Belgrade, <sup>2</sup>Institute of  
Chemistry, Technology and Metallurgy, University of Belgrade, Njegoševa 12,  
11000 Belgrade, <sup>3</sup>Faculty of Pharmacy, University of Belgrade,  
Vojvode Stepe 450, 11000 Belgrade, Serbia

(Received 17 June 2008)

**Abstract:** The genus *Senecio* (family Asteraceae) is one of the largest in the world. It comprises about 1100 species which are the rich source of pyrrolizidine alkaloids. Plants containing pyrrolizidine alkaloids are among the most important sources of human and animal exposure to plant toxins and carcinogens. The pyrrolizidine alkaloids of seven *Senecio* species (*S. erucifolius*, *S. othonnae*, *S. wagneri*, *S. subalpinus*, *S. carpathicus*, *S. paludosus* and *S. rupestris*) were studied. Fourteen alkaloids were isolated and their structures determined from spectroscopic data (<sup>1</sup>H- and <sup>13</sup>C-NMR, IR and MS). Five of them were identified in *S. erucifolius*, four in *S. othonnae*, two in *S. wagneri*, four in *S. subalpinus*, two in *S. carpathicus*, three in *S. paludosus* and three in *S. rupestris*. Seven pyrrolizidine alkaloids were found for the first time in particular species. The results have chemotaxonomic importance. The cytotoxic activity and antimicrobial activity of some alkaloids were also studied.

**Keywords:** *Senecio*; pyrrolizidine alkaloids; antitumor and antimicrobial activity.

### INTRODUCTION

The toxic pyrrolizidine alkaloids (PA) are a large group of related compounds that occur in plants, mainly in species of *Crotalaria* (Leguminosae), *Senecio* and related genera (Compositae), *Heliotropium*, *Trichodesma*, *Symphytum*, *Echium* and other genera of the Boraginaceae.

The worldwide distributed genus *Senecio* (family Asteraceae) is a rich source of pyrrolizidine alkaloids. It was shown that the alkaloid pattern differs between some subspecies.<sup>1–4</sup> Previous investigations of alkaloids from seven *Senecio* spe-

\* Corresponding author. E-mail: smilo@chem.bg.ac.rs

# Serbian Chemical Society member.

doi: 10.2298/JSC0901027M

cies (*S. erucifolius*, *S. othonnae*, *S. wagneri*, *S. subalpinus*, *S. carpathicus*, *S. paludosus* and *S. rupestris*) are presented in short in Table I.<sup>5–27</sup>

TABLE I. Alkaloids (1–37) isolated from species of genus *Senecio* (Columns: I – *S. erucifolius*; II – *S. othonnae*; III – *S. wagneri*; IV – *S. subalpinus*; V – *S. carpathicus*; VI – *S. paludosus*; VII – *S. rupestris*). The Arabic numbers in the columns correspond to the reference numbers of the papers

Alkaloid	I	II	III	IV	V	VI	VII
Senecionine (1)	5–11	12	–	5, 13, 14	–	–	5, 15, 16
Seneciophylline (2)	5, 6, 8, 9, 10, 11	17	–	5, 13, 14	5	18–20	–
<i>O</i> -AcetylSeneciophylline (3)	10	–	–	–	–	–	–
Seneciophylline <i>N</i> -oxide (4)	21	–	–	–	–	–	–
<i>O</i> -AcetylSeneciophylline <i>N</i> -oxide (5)	21	–	–	–	–	–	–
Senecivernine (6)	6, 10	–	–	5	–	–	5
Integerimmine (7)	5, 6, 9, 10	–	–	5, 13	–	–	5, 15, 16
21-Hydroxyintegerimmine (8)	5	–	–	–	–	–	5
Integerimmine <i>N</i> -oxide (9)	21	–	–	–	–	–	–
Senkirkine (10)	5, 9	–	5	–	–	–	–
<i>O</i> -AcetylSenkirkine (11)	9	–	–	–	–	–	–
Neosenkirkine (12)	–	–	5	–	–	–	–
Otosenine (13)	–	17, 22, 23	–	–	–	–	–
Doronine (14)	–	22, 23	–	–	–	–	–
Platyphylline (15)	–	12	–	–	–	–	–
Neoplatyphylline (16)	–	–	–	5	–	–	–
7-Angeloylplatynecine (17)	–	–	–	–	–	24	–
9-Angelylplatynecine (18)	–	–	–	–	–	25	–
Retronecine (19)	–	12	–	–	–	–	–
Onetine (20)	–	17, 22	–	–	–	–	–
Othonnine (21)	–	12	–	–	–	–	–
Retrorsine (22)	8	12	–	–	–	–	16
Dihydroretrorsine (23)	–	–	–	–	–	24	–
Erucifoline (24)	6, 10	–	–	–	–	–	–
<i>O</i> -Acetylerucifoline (25)	10	–	–	–	–	–	–
Erucifoline <i>N</i> -oxide (26)	21	–	–	–	–	–	–
Eruciflorine (27)	6	–	–	–	–	–	–
Procerine (28)	–	–	5	–	–	–	–
Racemonine (29)	–	–	–	–	–	26, 27	–
Racemocine (30)	–	–	–	–	–	26, 27	–
Racemodine (31)	–	–	–	–	–	24	–
Floridanine (32)	–	22, 23	–	–	–	–	–
Senecioracene (33)	–	–	–	–	–	25	–
Sarracine (34)	–	–	–	–	–	25	–
Riddeline (35)	–	12	–	–	–	–	–
7-Angelylheliotridine (36)	–	–	5	–	–	–	–
Spartioidine (37)	6	–	–	–	–	–	–

Despite the fact that secondary metabolites (especially PAs) of *Senecio* species have been the subject of investigations for many years, interest in them remains. The investigations of the activities of plants PAs indicated their neurotoxic, mutagenic, carcinogenic, but also antitumor effects.<sup>28,29</sup> PAs are readily absorbed from the digestive tract and cause harmful effects only after undergoing activation in the liver to toxic metabolites. The effects include a variety of changes leading to permanent damage to genes and chromosomes, the ability of cells to divide, the development of cancer and even cell death. Some of them are strong toxins for humans and domestic animals.<sup>30,31</sup> The acute toxicity of PAs varies widely. The rat  $LD_{50}$  of most alkaloids known to be significant for human health are in the range of 34–300 mg/kg, although some approach 1000 mg/kg.

On the other hand, many *Senecio* species are used in traditional medicine in Asia and Africa, which makes them a very interesting for phytochemical investigation.

In this study, the pyrrolizidine alkaloids from seven *Senecio* species (*S. erucifolius*, *S. othonnae*, *S. wagneri*, *S. subalpinus*, *S. carpathicus*, *S. paludosus* and *S. rupestris*) were isolated and their structure elucidated. Also, the cytotoxicity and antimicrobial activity of some of PAs were investigated.

## EXPERIMENTAL

### General

The IR spectra were measured in the form of KBr pellets on a Perkin-Elmer FT-IR spectrometer 1725X. The  $^1\text{H}$ - (200 MHz) and  $^{13}\text{C}$ -NMR (50 MHz) spectra were recorded on a Varian Gemini 2000 spectrometer. The mass spectra were obtained on a Finnigan MAT 8230, BE DCI (150 eV, iso-butane).

Silica gel, 0.008 mm (Merck, Darmstadt, Germany), was used for preparative column chromatography (CC) and silica gel F-254 (Merck, Darmstadt, Germany) for analytical and preparative thin layer chromatography (TLC).

### Plant material

The studied species and collection data are listed in Table II.

TABLE II. Studied species and collection data

Species	Collection data
<i>S. erucifolius</i>	Deliblatska peščara, Serbia, July 2003
<i>S. othonnae</i>	Sinjajevina, Montenegro, August 2003
<i>S. wagneri</i>	Maja Rusalija, Montenegro, July 2004
<i>S. subalpinus</i>	Hajla, Montenegro, July 2003
<i>S. carpathicus</i>	Stara planina, Serbia, July 2004
<i>S. paludosus</i>	Suva planina, Serbia, July 2005
<i>S. rupestris</i>	Lisa, Montenegro, July 2005

### Extraction and isolation

The dried and powdered plant material of each sample was extracted with methanol. After solvent removal, the residue was dissolved in 1.0 M sulfuric acid, washed with  $\text{CH}_2\text{Cl}_2$ , the pH adjusted to 9.0 with  $\text{NH}_4\text{OH}$ , extracted with  $\text{CH}_2\text{Cl}_2$  and purified by silica gel CC and

prep. TLC to yield pure alkaloids. The elution was commenced with CH<sub>2</sub>Cl<sub>2</sub>:methanol:NH<sub>4</sub>OH (9:1:0.1) and the polarity was gradually increased. The spots were detected under UV<sub>254</sub>, by Dragendorff reagent or by spraying with 50 % H<sub>2</sub>SO<sub>4</sub>.

#### *Investigation of antiproliferative and antimicrobial activity*

Stock solutions of the isolated alkaloids were prepared in DMSO at a concentration of 10 mM and afterwards diluted with nutrient medium (RPMI 1640), supplemented with L-glutamine (3 mM), streptomycin (100 µg/ml), penicillin (100 IU/ml), 10 % heat inactivated (56 °C) fetal bovine serum and 25 mM Hepes, adjusted to pH 7.2 with bicarbonate solution and applied to the target cells (human cervix carcinoma HeLa cells, human myelogenous leukemia K562 cells, human melanoma Fem-X cells and normal human peripheral blood mononuclear cells) at various final concentrations ranging from 0 to 100 µM. HeLa and Fem-X cell survival was determined indirectly by measuring the total cellular protein by the Kenacid Blue R dye binding method.<sup>32</sup> Inhibition of the growth of PBMC and K562 cells was determined by the MTT test.<sup>33</sup>

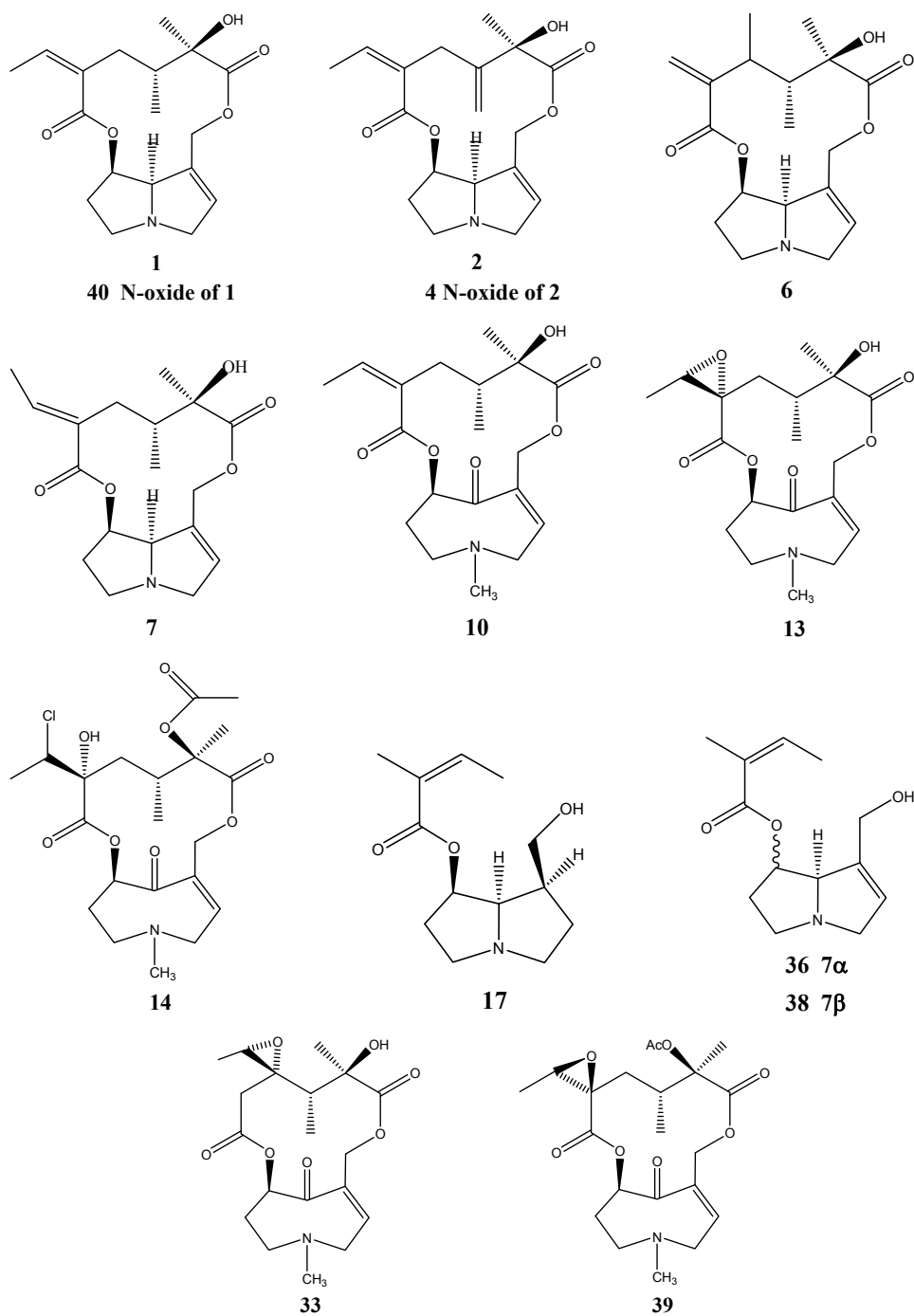
The antibacterial activity of alkaloids (otosenine, seneciophylline and a mixture of senecionine and seneciophylline) was tested against the microorganisms *Staphylococcus aureus*, *Escherichia coli*, *Bacillus subtilis*, *Candida albicans* and *Aspergillus niger*. The concentration of the tested samples was 1.0 mg/ml. The surface of an agar plate was inoculated by streaking the bacterial suspension (*ca.* 10<sup>5</sup> cfu/ml). After incubation at 37 °C for 24 h, the inhibitory effect was determined as the prevention of visible growth.

### RESULTS AND DISCUSSION

The isolation procedure for alkaloids from the crude extract (of seven *Senecio* species: *S. erucifolius*, *S. othonnae*, *S. wagneri*, *S. subalpinus*, *S. carpathicus*, *S. paludosus* and *S. rupestris*) yielded fourteen alkaloids (**1**, **2**, **4**, **6**, **7**, **10**, **13**, **14**, **17**, **33**, **36**, **38–40**) (Table III, Scheme 1). The structural assignments of alkaloids were based on comparison of their spectral data with those published in literature.<sup>34,35</sup>

TABLE III. Alkaloids isolated from species of genus *Senecio* (Columns: I – *S. erucifolius*; II – *S. othonnae*; III – *S. wagneri*; IV – *S. subalpinus*; V – *S. carpathicus*; VI – *S. paludosus*; VII – *S. rupestris*). Mark PA indicates alkaloids isolated for the first time from the *Senecio* species

Alkaloid	I	II	III	IV	V	VI	VII
Senecionine ( <b>1</b> )	+	–	–	+	–	–	+
Seneciophylline ( <b>2</b> )	+	–	–	+	+	–	–
Seneciophylline <i>N</i> -oxide ( <b>4</b> )	+	–	–	PA	PA	–	–
Senecivernine ( <b>6</b> )	–	–	–	–	–	–	+
Integerimmine ( <b>7</b> )	–	–	–	–	–	–	+
Senkirkine ( <b>10</b> )	–	–	+	–	–	PA	–
Otosenine ( <b>13</b> )	PA	+	–	–	–	–	–
Doronine ( <b>14</b> )	–	+	–	–	–	–	–
7-Angeloylplatynecine ( <b>17</b> )	–	–	–	–	–	+	–
Senecioracene ( <b>33</b> )	–	PA	–	–	–	–	–
7-Angelylheliotridine ( <b>36</b> )	–	–	+	–	–	–	–
7-Angelylretronecine ( <b>38</b> )	–	–	–	–	–	PA	–
Neopetasitenine ( <b>39</b> )	–	PA	–	–	–	–	–
Senecionine <i>N</i> -oxide ( <b>40</b> )	PA	–	–	PA	–	–	–



Scheme 1.

Previous studies of *S. erucifolius* resulted in the isolation and identification of 17 PAs (**1–11**, **22**, **24–27** and **37**). In the present study, three of the previously identified alkaloids (senecionine, seneciphylline and seneciphylline *N*-oxide) and an additional two, namely otosenine (**13**) and senecionine *N*-oxide (**40**), are now reported and identified for the first time as alkaloids in *S. erucifolius*.

Four alkaloids were identified from *S. othonnae*, two of them (otosenine and doronine) were previously reported in this plant. Senecioracene (**33**) and neopetasitenine (**39**) are alkaloids isolated for the first time from this species.

Four PAs, namely senkirkine, neosenkirkine, procerine and 7-angeloylheliotridine (**10**, **12**, **28** and **36**) were previously isolated from *S. wagneri*. This investigation confirmed the presence of two alkaloids senkirkine (**10**) and 7-angeloylheliotridine (**36**).

Senecionine (**1**) and seneciphylline (**2**) identified in *S. subalpinus* are two of five previously isolated alkaloids. However, seneciphylline *N*-oxide (**4**) and senecionine *N*-oxide (**40**) are alkaloids new for this plant.

One (**2**) and five (**1**, **6**, **7**, **8** and **22**) alkaloids were previously isolated from *S. carpathicus* and *S. rupestris*, respectively. In this investigation, the presence of seneciphylline (**2**) as well as senecionine, senecivernine and integerimine (**1**, **6** and **7**) respectively, were confirmed. Seneciphylline *N*-oxide (**4**) was isolated from *S. carpathicus* for the first time.

One (7-angeloylplatynecine) of nine previously reported alkaloids of *S. paludosus* was identified in the present study. An additional two alkaloids, namely senkirkine (**10**) and 7-angeloylretronecine (**38**), had not been previously isolated from this plant.

In order to anticipate antitumor action, the antiproliferative activity of some alkaloids (senkirkine and a mixture of senecionine and seneciphylline, which were isolated in sufficient quantities to allow bioassays) against malignant cell lines (human cervix carcinoma HeLa cells, human myelogenous leukemia K562 cells and human melanoma Fem-X cells) and normal human cells (PBMC) was tested. The investigated alkaloids (in concentrations from 0 to 100  $\mu$ M) exhibited no cytotoxic effects against any of the tested human cancer cells.

The antimicrobial action of otosenine, seneciphylline and a mixture of senecionine and seneciphylline against *Staphylococcus aureus*, *Escherichia coli*, *Bacillus subtilis*, *Candida albicans* and *Aspergillus niger* was also investigated. Only the senecionine-seneciphylline mixture (2:1) exhibited a weak (on the limit of detection) inhibitory effect against *A. niger* at a concentration of 1 mg/ml.

#### CONCLUSIONS

Fourteen pyrrolizidine alkaloids were isolated and identified from seven *Senecio* species (*S. erucifolius*, *S. othonnae*, *S. wagneri*, *S. subalpinus*, *S. carpathicus*, *S. paludosus* and *S. rupestris*). Seven of them were identified for the first time in the particular species. The results are of chemotaxonomic importance.

Senkirkine and a mixture of senecionine and seneciphylline at the investigated concentrations did not exhibit antiproliferative effects against the tested human malignant cell lines. However, a mixture of senecionine and seneciphylline exhibited a weak antimicrobial effect against *Aspergillus niger*.

*Acknowledgement.* The authors acknowledge their gratitude to the Ministry of Science of the Republic of Serbia for financial support (Project No. 142053).

## ИЗВОД

ПИРОЛИЗИДИНСКИ АЛКАЛОИДИ ИЗ СЕДАМ САМОНИКЛИХ БИЉНИХ ВРСТА РОДА *Senecio* КОЈЕ РАСТУ У СРБИЈИ И ЦРНОЈ ГОРИ

БОРИС М. МАНДИЋ<sup>1</sup>, ДЕЈАН Н. ГОЂЕВАЦ<sup>2</sup>, ВЛАДИМИР П. БЕШКОСКИ<sup>2</sup>, МИЛЕНА Р. СИМИЋ<sup>3</sup>, СНЕЖАНА С. ТРИФУНОВИЋ<sup>2</sup>, ВЕЛЕ В. ТЕШЕВИЋ<sup>1</sup>, ВЛАТКА В. ВАЈС<sup>2</sup> И СЛОБОДАН М. МИЛОСАВЉЕВИЋ<sup>1</sup>

<sup>1</sup>Хемијски факултет, Студентски брџ 16, 11000 Београд, <sup>2</sup>Институт за хемију, технологију и металургију, Универзитет у Београду, Њеџошева 12, 11000 Београд и <sup>3</sup>Фармацеутички факултет, Универзитет у Београду, Војводе Силеје 450, 11000 Београд

Један од најбројнијих родова на свету је род *Senecio* (фамилија Asteraceae). Обухвата око 1100 врста које представљају богат извор пирилизидинских алкалоида. Најзначајнија изложеност људи и животиња биљним токсинима и карциногенима потиче од биљака које садрже пирилизидинске алкалоиде. У овом раду изоловани су пирилизидински алкалоиди из седам врста рода *Senecio* (*S. erucifolius*, *S. othonnae*, *S. wagneri*, *S. subalpinus*, *S. carpathicus*, *S. paludosus* и *S. rupestris*), а њихове структуре одређене на бази спектроскопских података (<sup>1</sup>H- и <sup>13</sup>C-NMR, IR и MS). Изоловано је укупно 14 алкалоида, пет из *S. erucifolius*, четири из *S. othonnae*, два из *S. wagneri*, четири из *S. subalpinus*, два из *S. carpathicus*, три из *S. paludosus* и три из *S. rupestris*. Седам пирилизидинских алкалоида је по први пут изоловано из неких појединачних врста. Добијени резултати имају хемотаксономски значај. Испитана је цитотоксичност и антимикуробна активност изолованих алкалоида.

(Примљено 17. јуна 2008)

## REFERENCES

1. V. Christov, N. Kostova, L. Evstatieva, *Nat. Prod. Res.* **19** (2005) 300
2. N. Kostova, V. Christov, M. Cholakova, E. Nikolova, L. Evstatieva, *J. Serb. Chem. Soc.* **71** (2006) 1275
3. T. Hartmann, L. Witte, A. Ehmke, C. Theuring, M. Rowell-Rahier, J. Pasteels, *Phytochemistry* **45** (1997) 489
4. E. Roeder, H. Wiedenfeld, P. Knoezinger-Firscher, *Planta Med.* **50** (1984) 203
5. V. Christov, L. Evstatieva, *Z. Naturforsch. C: J. Biosci.* **58** (2003) 300
6. L. Witte, L. Ernst, H. Adam, T. Hartmann, *Phytochemistry* **31** (1992) 559
7. A. Boeva, B. Stefanova-Gateva, D. Krushovska, *Farmatsiya* **29** (1979) 32 (in Russian)
8. S. Ferry, J. L. Brazier, *Ann. Pharm. Francaises* **34** (1976) 133
9. D. S. Bhakuni, S. Gupta, *Planta Med.* **46** (1982) 251
10. G. Toppel, L. Witte, B. Riebesehl, K. Von Borstel, T. Hartmann, *Plant Cell Rep.* **6** (1987) 466
11. I. Kompis, F. Santavy, *Collect. Czech. Chem. C.* **27** (1962) 1413
12. B. Sener, F. Ergun, S. Kusmenoglu, A. E. Karakaya, *Gazi Universitesi Eczacilik Fakultesi Dergisi* **5** (1988) 101

13. A. Klasek, T. Reichstein, F. Santavy, *Helv. Chim. Acta* **51** (1968) 1089
14. B. Trivedi, F. Santavy, *Collect. Czech. Chem. C* **28** (1963) 3455
15. A. Sidjimov, A. Tashev, *Godishnik na Sofiiskiia Universitet "Sv. Kliment Okhridski"*, Khimicheski Fakultet, **97** (2005) 130 (in Bulgarian)
16. E. Roeder, T. Pflueger, *Nat. Toxins* **3** (1995) 305
17. A. V. Danilova, N. I. Koretskaya, L. M. Utkin, *Zh. Obshch. Khimii* **32** (1962) 647 (in Russian)
18. V. S. Alekseev, *Farm. Zh. (Kiev)* **16** (1961) 39 (in Russian)
19. V. S. Alekseev, *Izuch. i Ispol'z. Lekarstv. Rast. Resursov SSSR Sb.* (1964) 204 (in Russian)
20. M. P. Khmel, *Farm. Zh. (Kiev)* **16** (1961) 35 (in Russian)
21. H. Sander, T. Hartmann, *Plant Cell Tissue Org.* **18** (1989) 19
22. D. S. Khalilov, M. V. Telezhenetskaya, S. N. Yunusov, *Khim. Prir. Soedin.* **2** (1980) 262 (in Russian)
23. D. S. Khalilov, M. V. Telezhenetskaya, S. N. Yunusov, *Khim. Prir. Soedin.* **6** (1977) 866 (in Russian)
24. W. Ahmed, A. Q. Khan, A. Malik, F. Ergun, B. Sener, *Phytochemistry* **32** (1992) 224
25. W. Ahmed, A. Q. Khan, A. Malik, F. Ergun, B. Sener, *J. Nat. Prod.* **55** (1992) 1764
26. W. Ahmed, A. Q. Khan, A. Malik, F. Ergun, B. Sener, *Fitoterapia* **64** (1993) 361
27. W. Ahmed, Z. Ahmed, A. Malik, F. Ergun, B. Sener, *Heterocycles* **32** (1991) 1729
28. E. Roeder, *Pharmazie* **50** (1995) 83
29. E. Roeder, *Curr. Org. Chem.* **3** (1999) 557
30. R. A. Smith, E. Panariti, *Vet. Hum. Toxicol.* **37** (1995) 478
31. P. R. Cheeke, *Toxicants of Plant Origin, Vol. 1, Alkaloids*, CRC Press, Boca Raton, 1989, p. 1
32. R. H. Clothier, *Meth. Mol. Biol.* **43** (1995) 109
33. M. Ohno, T. Abe, *J. Immunol. Meth.* **145** (1991) 199
34. C. G. Logie, M. R. Grue, J. R. Liddel, *Phytochemistry* **37** (1994) 43
35. E. Roeder, *Phytochemistry* **29** (1990) 11.



www.shd.org.rs

J. Serb. Chem. Soc. 74 (1) 35–44 (2009)  
JSCS–3806

JSCS@tmf.bg.ac.yu • www.shd.org.rs/JSCS

UDC \*Ramonda serbica Panč.:  
:556.132.6:665.52/54

Original scientific paper

## Volatiles from vegetative organs of the palaeoendemic resurrection plants *Ramonda serbica* Panč. and *Ramonda nathaliae* Panč. et Petrov.

NIKO S. RADULOVIĆ<sup>1\*</sup>, POLINA D. BLAGOJEVIĆ<sup>1</sup>, RADOSAV M. PALIĆ<sup>1</sup>,  
BOJAN K. ZLATKOVIĆ<sup>2</sup> and BRANKA M. STEVANOVIĆ<sup>3</sup>

<sup>1</sup>Department of Chemistry, Faculty of Science and Mathematics, University of Niš, Višegradaska 33, 18000 Niš, <sup>2</sup>Department of Biology and Ecology, Faculty of Science and Mathematics, University of Niš, Višegradaska 33, 18000 Niš and <sup>3</sup>Department of Plant Ecology and Phytogeography, Institute of Botany and Botanical Garden "Jevremovac", Faculty of Biology, University of Belgrade, 11000 Belgrade, Takovska 43, Serbia

(Received 16 July 2008)

**Abstract:** GC and GC/MS analyses of the essential oils hydrodistilled separately from fresh leaves and roots of *Ramonda serbica* and *Ramonda nathaliae*, together with diethyl ether extracts of their roots, enabled the identification of 82 constituents accounting for between 88.9 and 94.5 % of the oils and extracted compounds. Although phenylacetaldehyde was one of the major contributors (20.5–57.1 %) of all the oils, it was only a minor contributor to the extracts. The latter were characterized by a large amount of squalene (*R. serbica* – 36.0 %; *R. nathaliae* – 59.4%) and steroids (*R. serbica* – 27.4 %; *R. nathaliae* – 14.1 %). Squalene was also the most abundant compound in *R. nathaliae* root oil (29.0 %), but was not detected in the corresponding *R. serbica* oil. While the root oils and extracts of both species contained comparable amounts of volatile fatty acids, there were significant differences in their contents in the oils hydrodistilled from the leaves of *R. serbica* and *R. nathaliae* (18.7 % and 0.6 %, respectively). The presented results provide the first insight into the unique sets of volatiles produced by these distinctive, closely related, relict taxa, which disclose their specific adaptive advantages.

**Keywords:** *Ramonda serbica*; *Ramonda nathaliae*; essential oil; ether extract; squalene; phenylacetaldehyde.

### INTRODUCTION

The genus *Ramonda* (Gesneriaceae) includes three relict palaeoendemic species of the Tertiary Period, surviving as the rare resurrection angiosperms of the Northern hemisphere in refugia habitats on the Balkan (*Ramonda nathaliae* Panč.

\* Corresponding author. E-mail: vangelis0703@yahoo.com  
doi: 10.2298/JSC0901035R

*et* Petrov. and *Ramonda serbica* Panč.) and Iberian (*Ramonda myconi* (L.) Rchb.) Peninsulas. Their current distribution is restricted to the northern rocky slopes of gorges and canyons, mainly on foothills, sometimes reaching the alpine belts.<sup>1,2</sup> They all prefer limestone rocks, while *R. nathaliae* also settles on ophiolitic bedrock.<sup>1,3</sup> The ranges of the Balkan *Ramonda* species, discovered at the beginning of the 19<sup>th</sup> century by the Serbian botanists Pančić and Petrović, overlap in SE Serbia, constituting a sympatric zone with mixed or spatially very close populations. The distribution of *R. serbica* thus extends from NW Bulgaria, SE and SW Serbia, NE and SE Montenegro to Albania, W FYR Macedonia and NW Greece, while *R. nathaliae* is spread in N and C FYR Macedonia and N Greece, with a disjunct part of the range in SE Serbia.<sup>1,2,4,5</sup> It is noteworthy that the natural hybridization, proposed to occur between *R. serbica* and *R. nathaliae*, has been confirmed by genome size analysis in the sympatric populations from their localities in SE Serbia.<sup>6</sup>

*Ramonda* species have been the subject of several biological, genetic, and biochemical studies concerning the defence mechanism and the physiological changes that occur during dehydration and rehydration, their genome size and variation of the ploidy level, polymorphism, *etc.*<sup>6–13</sup> The volatile constituents of the vegetative organs of the *Ramonda* species, however, have not been studied. The aim of this study was to determine the chemical composition of the essential oils of the leaves and roots and of the root diethyl ether extracts of *R. serbica* and *R. nathaliae*, and, if possible, to clarify the differentiation in the taxonomic relationship between the two taxa, from their volatile profiles.

## EXPERIMENTAL

### *Plant material*

Leaves and roots of the two Balkan *Ramonda* species were collected at the beginning of May, 2007. Sample sites included two distant populations, one located on the slopes of Suva planina (*R. nathaliae*, voucher No. 16208) and the other in Sićevačka klisura (*R. serbica*, voucher No. 20639) in SE Serbia. Voucher specimens were deposited in the Herbarium of the Institute of Botany and Botanical Garden (BEOU) “Jevremovac”, Department of Plant Ecology and Phytogeography, Faculty of Biology, University of Belgrade.<sup>14</sup>

### *Isolation of the essential oils and preparation of the extracts*

The minimal amount (500 g) of plant material (fresh leaves or roots of *R. serbica* and *R. nathaliae*) was subjected to hydrodistillation for 2.5 h using a Clevenger-type apparatus. The oils obtained were separated, dried over anhydrous sodium sulphate and immediately analyzed. The yields (% w/w) were the following: *R. serbica* root oil, 0.002; *R. serbica* leaf oil, 0.002; *R. nathaliae* root oil, 0.004 and *R. nathaliae* leaf oil, 0.003.

Roots of *R. serbica* and *R. nathaliae* (50 g) were cut into small pieces and extracted in sealed vessels with 250 mL of diethyl ether in an ultrasonic bath (Bandelin electronic, GmbH & Co. KG, Germany) for 5 h at room temperature. The extracts were gravity filtered through small columns packed with 1 g of Celite<sup>®</sup> (Merck, Germany), to remove all the insoluble material, and then concentrated to 10 mL at room temperature using a stream of nitrogen be-

fore GC and GC/MS analyses. The yields of dry extracts (% w/w), obtained by complete evaporation of the solvents *in vacuo*, were 0.037 (*R. serbica*) and 0.052 (*R. nathaliae*).

#### *Gas chromatography and gas chromatography/mass spectrometry*

The GC/MS analyses (three repetitions of each sample) were performed using a Hewlett-Packard 6890N gas chromatograph equipped with a fused silica capillary column HP-5MS (5 % phenylmethylsiloxane, 30 m×0.25 mm, film thickness 0.25 µm, Agilent Technologies, USA) and coupled with a 5975B mass selective detector from the same company. The injector and interface were operated at 250 and 300 °C, respectively. The oven temperature was raised from 70 to 290 °C at a heating rate of 5 °C/min and then held isothermally for 10 min. Helium at 1.0 mL/min was used as the carrier gas. 1 µL of the oil solution in diethyl ether (1:100) or the extract, prepared as earlier mentioned, was injected in a pulsed split mode (the flow was 1.5 mL/min for the first 0.5 min and then set to 1.0 mL/min throughout the remainder of the analysis; split ratio 40:1). The MS conditions were: ionization voltage 70 eV, acquisition mass range 35–500, scan time 0.32 s. The oil and extract constituents were identified by comparing their linear retention indices (relative to C<sub>7</sub>–C<sub>33</sub> alkanes<sup>15</sup> on the HP-5MS column) with literature values<sup>16</sup> and their mass spectra with those of authentic standards, as well as those from Wiley 6, NIST02, MassFinder 2.3, and a homemade MS library with the spectra corresponding to pure substances and components of known oils. Wherever possible, the identity of the constituents was verified by co-injection with an authentic sample. GC (FID) analysis was performed under the same experimental conditions using the same column as described for the GC/MS measurements. The percentage composition of the oil was computed from the GC peak areas without any corrections.

## RESULTS AND DISCUSSION

GC and GC/MS analyses of *R. serbica* and *R. nathaliae* essential oils and extracts enabled the overall identification of 82 components, listed in Table I. The common feature of the oils was their high content of phenylacetaldehyde (from 20.5 to 57.1 %), a constituent found only as a minor contributor to the root extracts from the two plant species. The diethyl ether extracts, on the other hand, were characterized by large amounts of squalene (36.0 % in *R. serbica* and 59.4 % in *R. nathaliae*) and steroids (27.4 % in *R. serbica* and 14.1 % in *R. nathaliae*). In addition, constituents belonging to the following classes: terpenoids, alkanes, fatty acids, carotenoid derived compounds and “green leaf” volatiles, were present in almost all the oils and extracts (Table I). It might be assumed that certain volatiles listed in Table I could be considered as artefacts of the isolation procedure and not as direct products of plant metabolism. For example, 3-(methylthio)propanal and 2-acetylthiazole (identified only in the volatile oils) could be products of Maillard-type reactions including the thermal fragmentation of amino acids and sugars, alone or in conjunction, during hydrodistillation.<sup>17</sup> The “green leaf” volatiles, on the other hand, are most probably produced by enzymatic degradation of unsaturated fatty acids, such as in desiccation, *i.e.*, as a stress-induced response of the plants, produced during collection and preparation of the plant samples.<sup>18</sup> Some scent compounds identified in the analyzed essential oils and extracts of *R. serbica* and *R. nathaliae* could be related to their pollination

biology, since it has been shown that a blend containing phenylacetaldehyde, 2-phenylethanol, and benzaldehyde (compounds present in the analyzed oils and extracts, Table I) is attractive to halictid bees.<sup>19</sup>

TABLE I. Percentage composition of *R. serbica* and *R. nathaliae* leaf and root essential oils and root diethyl ether extracts

<i>RF</i> <sup>a</sup>	Compound	Class	Method <sup>b</sup>	<i>R. serbica</i>			<i>R. nathaliae</i>		
				Root oil	Leaf oil	Root extract	Root oil	Leaf oil	Root extract
753	2-Methylpropanoic acid	F	a, b, c						0.1
763	Butanoic acid	F	a, b, c			0.2			
765	3-Methyl-2-buten-1-ol	T	a, b		0.4				
827	3-Methylbutanoic acid (syn. <sup>c</sup> Isovaleric acid)	T	a, b, c			2.9			
828	Furfural	GL	a, b, c	3.0	0.4			tr <sup>d</sup>	
832	2-Methylbutanoic acid	T	a, b, c			0.7	0.3		0.3
833	3-Methylpentanol	GL	a, b			tr			
844	( <i>E</i> )-3-Hexenol	GL	a, b		0.2				
908	3-(Methylthio)propanal	O	a, b	1.0	0.4				
965	Benzaldehyde	O	a, b, c	3.3	0.2	0.2	1.0	1.8	tr
970	Hexanoic acid	F	a, b, c			tr			
978	1-Octen-3-ol	GL	a, b		5.0	tr		8.1	
995	2-Pentylfuran	GL	a, b			tr			
1014	( <i>E,E</i> )-2,4-Heptadienal	GL	a, b					tr	
1021	2-Acetylthiazole	O	a, b		0.2				
1037	Benzyl alcohol	O	a, b, c			0.2	0.7	0.5	
1047	Phenylacetaldehyde	O	a, b, c	57.1	41.6	tr	20.5	52.2	0.2
1056	5-Methyldecane	A	a, b	tr	tr	tr			
1061	4-Methyldecane	A	a, b	2.3	tr	tr			
1070	Acetophenone	O	a, b, c	1.7	0.4	tr			
1100	Undecane	A	a, b, c	3.6	tr	tr			
1102	Linalool	T	a, b, c		1.3		0.6	0.8	
1108	( <i>Z</i> )-6-Methyl-3,5-heptadien-2-one	CR	a, b	3.3				1.2	
1118	2-Phenylethanol	O	a, b, c			0.8	0.6	tr	tr
1126	Isophorone	CR	a, b					tr	
1163	Benzoic acid	O	a, b, c			tr			
1167	<i>o</i> -Hydroxyacetophenone	O	a, b, c		tr				
1170	3,5-Dimethylphenol	O	a, b	4.0	2.1		tr		
1172	Borneol	T	a, b, c				0.9	1.1	
1196	$\alpha$ -Terpineol	T	a, b, c		tr			tr	
1252	Phenylacetic acid	O	a, b			1.8			tr
1257	Geraniol	T	a, b, c				0.8		
1280	3-Methyldodecane	A	a, b	tr	2.3	0.2			
1294	Thymol	T	a, b, c		0.6		1.8		
1300	Tridecane	A	a, b, c	tr	tr				

TABLE I. Continued

R <sup>a</sup>	Compound	Class	Method <sup>b</sup>	<i>R. serbica</i>			<i>R. nathaliae</i>		
				Root oil	Leaf oil	Root extract	Root oil	Leaf oil	Root extract
1318	<i>p</i> -Vinylguaiacol	O	a, b	0.7	0.2		tr	tr	
1320	( <i>E,E</i> )-2,4-Decadienal	GL	a, b				0.9	0.8	
1405	Vanillin	O	a, b, c			tr			
1500	Pentadecane	A	a, b, c	3.6	1.9	0.2	0.4		
1525	1,2-Diphenylethane	O	a, b				0.4	5.7	
1585	4,6,8-Megastigmatrien-3-one <sup>c</sup>	CR	a, b		1.1				
1631	4,6,8-Megastigmatrien-3-one <sup>c</sup>	CR	a, b		0.8				
1661	( <i>E</i> )-4-Oxo- $\beta$ -ionone	CR	a, b			tr			
	Syringaldehyde	O	a, b			tr			
1667	(syn. 3,5-Dimethoxy-4-hydroxybenzaldehyde)								
1694	1-Heptadecene	AE	a, b					0.6	
1700	Heptadecane	A	a, b, c					0.3	
1755	5-Methylheptadecane	A	a, b	tr	1.1	tr	tr		
1762	Tetradecanoic acid	F	a, b, c		0.6	tr			
	Dehydrovomifoliol	CR	a, b			0.4			
1796	(syn. 7-Hydroxy-3-oxo- $\alpha$ -ionone)								
1800	Octadecane	A	a, b, c				tr		
	Syringic acid	O	a, b						1.0
1823	(syn. 3,5-Dimethoxy-4-hydroxybenzoic acid)								
1841	Neophytadiene Isomer I	T	a, b			tr			
1847	Hexahydrofarnesyl acetone	CR	a, b		0.6		0.7	1.7	
1944	( <i>E</i> )-9-Hexadecenoic acid (syn. ( <i>E</i> )-palmitoleic acid)	F	a, b			1.0			
1952	( <i>Z</i> )-9-Hexadecenoic acid (syn. ( <i>Z</i> )-Palmitoleic acid)	F	a, b			0.7			
1963	Hexadecanoic acid (syn. Palmitic acid)	F	a, b, c	5.3	18.1	5.8	6.2	0.6	3.3
1994	1-Eicosene	AE	a, b		0.8				
2000	Eicosane	A	a, b, c		tr		tr	tr	
2100	Heneicosane	A	a, b, c		0.4		tr	0.5	
2136	( <i>Z,Z</i> )-9,12-Octadecadienoic acid (syn. Linoleic acid)	F	a, b			6.0			7.2
2141	( <i>E</i> )-9-Octadecenoic acid (syn. Elaidic acid)	F	a, b, c			3.1			
2143	( <i>E,Z</i> )-9,12-Octadecadienoic acid	F	a, b						4.8

TABLE I. Continued

<i>RI</i> <sup>a</sup>	Compound	Class	Method <sup>b</sup>	<i>R. serbica</i>			<i>R. nathaliae</i>		
				Root oil	Leaf oil	Root extract	Root oil	Leaf oil	Root extract
2146	( <i>Z</i> )-9-Octadecenoic acid (syn. Oleic acid)	F	a, b, c			3.2			
2163	Octadecanoic acid (syn. Stearic acid)	F	a, b, c			0.5			
2194	1-Docosene	AE	a, b		0.8				
2200	Docosane	A	a, b, c	tr				tr	
2300	Tricosane	A	a, b, c				1.9	1.2	
2400	Tetracosane	A	a, b, c				0.4	tr	
2469	4-Methyltetracosane	A	a, b		0.6				
2500	Pentacosane	A	a, b, c			0.2	13.0	7.7	0.3
2600	Hexacosane	A	a, b, c				1.1	0.5	0.2
2662	4-Methylhexacosane	A	a, b				1.5	0.5	
2686	3-Methylhexacosane	A	a, b	tr	4.6				
2694	1-Heptacosene	AE	a, b				0.3		
2700	Heptacosane	A	a, b, c			0.6	9.0	4.2	0.3
2834	Squalene (all <i>E</i> )	T	a, b, c			36.0	29.0		59.4
2900	Nonacosane	A	a, b, c			1.2	1.1	0.5	0.2
3000	Triacontane	A	a, b, c		1.9				
3100	Hentriacontane	A	a, b			1.2			
3187	Stigmast-5-en-3 $\beta$ -ol (syn. $\beta$ -Sitosterol)	S	a, b			22.7			10.8
3200	Dotriacontane	A	a, b, c		2.1				
3237	Stigmast-4-en-3-one	S	a, b			4.7			3.3
	Total			88.9	90.7	94.5	93.1	90.5	91.4
	Terpenoids (T)				2.3	39.6	33.4	1.9	59.7
	Alkanes (A)			9.5	14.9	3.6	28.4	15.4	1.0
	<i>n</i> -Alkanes			7.2	8.6	3.6	26.9	14.9	1.0
	Branched alkanes			2.3	6.3	tr	1.5	0.5	
	1-Alkenes (AE)				1.6		0.3	0.9	
	Fatty acids (F)			5.3	18.7	20.3	6.2	0.6	15.3
	“Green leaf” volatiles (GL)			3.0	5.6	0.2	0.9	8.9	0.1
	Carotenoid derived compounds (CR)			3.3	2.5	0.4	0.7	2.9	
	Steroids (S)					27.4			14.1
	Others (O)			67.8	45.1	3.0	23.2	60.2	1.2

<sup>a</sup>Compounds listed in order of elution from a HP-5MS column (*RI* - experimentally determined retention indices on the mentioned column by co-injection of a homologous series of *n*-alkanes C<sub>7</sub>–C<sub>33</sub>); <sup>b</sup>a - constituent identified by mass spectra comparison, b - constituent identified by retention index matching; c - constituent identity confirmed by co-injection of an authentic sample; <sup>c</sup>synonym; <sup>d</sup>trace (<0.05 %); <sup>e</sup>correct stereoisomer not determined

To some extent, the limited production of volatile secondary metabolites by these *Ramonda* taxa is not surprising, knowing that they are palaeoendemic, evo-

lutionarily very old species. Moreover, the similarity in the chemical composition of their analyzed oils and extracts (Table I) was also expected, bearing in mind the close relationship of the species.<sup>7</sup> However, there are certain striking differences, for example, the fatty acids, one of the dominant compound classes in *R. serbica* leaf oil, were found only as a negligible percentage in the corresponding *R. nathaliae* oil. Furthermore, the root oil of *R. nathaliae* was characterized by a significant amount of terpenoid compounds, primarily squalene, while no terpenoids were identified in the *R. serbica* root oil. Even though squalene was by far the most dominant constituent of both extracts, the relative percentage of this compound was markedly higher in that obtained from *R. nathaliae*. A recent study concerning the genome size variation and polyploidy of *Ramonda* species showed that *R. serbica* is a hexaploid ( $2n = 6x = 144$ ) and *R. nathaliae* a diploid species ( $2n = 2x = 48$ ).<sup>7</sup> This difference in the ploidy level could be correlated to the more pronounced production and/or accumulation of squalene in *R. nathaliae*. For instance, the existence of a correlation between the production of proazulene compounds and ploidy level has been confirmed for some *Achillea* species.<sup>20</sup> In addition, squalene has long been known to exhibit antioxidant properties<sup>21</sup> and, therefore, could enhance the antioxidative system, which was essential for the survival of these poikilohydric or resurrection plants during their repeated dehydration/rehydration cycles. Squalene, which is related to cholesterol biosynthesis may be important in membrane conservation in anabiosis. Sterols are found predominantly in cell membranes and are thought to contribute to the correct functioning of membranes by controlling the fluidity characteristics of the membranes.<sup>22,23</sup> Squalene synthase represents a putative branch point in the isoprenoid biosynthetic pathway capable of diverting the carbon flow specifically to the biosynthesis of sterols and, hence, is considered a potential regulatory point for sterol metabolism.<sup>24</sup> Squalene epoxidase converts squalene into oxidosqualene, the precursor of all known plant sterols.<sup>25</sup> The results of a recent study on regulation of squalene synthase in tobacco suggests that sterol biosynthesis is localised to the apical meristems and that the apical meristems may be a source of sterols for other plant tissues.<sup>24</sup> Thus, it is important to stress that only the root volatiles (either the essential oils or extracts) consisted of a large quantity of squalene and steroids. It seems that since the apical meristems are mostly related to the root system, the present findings corroborate the correlation between the sterol biosynthesis and the meristem. Still, further research is required in this direction for the complete understanding of this special feature of resurrection plants to survive anabiosis for months with 2–5 % of relative water content in their leaves.

Another interesting feature of all of the oils and of the *R. serbica* extract was the presence of branched alkanes as minor contributors. Bearing in mind that these are rather rare in the plant kingdom and that related compounds were found

in the essential oils obtained from some other evolutionarily primitive and old higher plant taxa, such as *Equisetum*,<sup>26,27</sup> it could be assumed that the presence of branched alkanes could be a characteristic of old plant taxa.

Moreover, a comparison of the chemical composition of the oils obtained from the root and leaves of both *R. serbica* and *R. nathaliae* shows that there are certain dissimilarities between the production and/or accumulation of plant organ volatiles (Table I). This suggests that different species-specific biosynthetic pathways leading to the volatile constituents are operational, or at least favoured, in plant organs of each of these species.

As was already mentioned, the volatiles extracted from the taxa belonging to the genus *Ramonda* were not previously analyzed in general. In addition, there is only one reference concerning the essential oil of a species (*Sinningia aggregata*) from the same family (Gesneriaceae).<sup>28</sup> However, the volatile profiles of *S. aggregata* (main contributors of the oil were methyl linoleate (28.4 %), 1-octadecanol (16.9 %), (*Z*)-nerolidyl acetate (8.8 %), spathulenol (7.8 %) and (*E*)-nerolidol (6.7 %)) and of the currently analyzed *Ramonda* species differed significantly. For example, sesquiterpenoids were not among the identified volatiles in either *R. serbica* or *R. nathaliae*, while these comprised *ca.* one third of the *S. aggregata* oil. This distinction of the *Ramonda* oils is even more obvious by further comparison of *Ramonda* volatiles to those of plant taxa belonging to the recognized "aromatic" families (*e.g.*, Asteraceae, Apiaceae, Lamiaceae). While the "aromatic" species, rich in essential oils, with yields ranging from 0.1–10.0 % (*cf.* to the value  $\approx$  0.001 % for the presently investigated *Ramonda*), predominantly produce volatile mono- and sesquiterpenoids and/or phenylpropanoids, these compound classes were represented as only minor contributors, or were not identified at all in the oils and extracts of *Ramonda*.<sup>29–31</sup>

#### CONCLUSIONS

The identification of 82 compounds as constituents of the essential oils hydrodistilled separately from the fresh leaves and roots of *Ramonda serbica* and *Ramonda nathaliae*, together with the diethyl ether extracts of their roots, studied for the first time, revealed phenylacetaldehyde as one of the major contributors (20.5–57.1 %) of all the oils, but only as a minor contributor of the extracts. The latter were characterized by large amounts of squalene (*R. serbica*, 36.0 %; *R. nathaliae*, 59.4 %) and steroids (*R. serbica*, 27.4 %; *R. nathaliae*, 14.1 %). Squalene was also the most abundant compound in *R. nathaliae* root oil (29.0 %), but was not detected in the corresponding *R. serbica* oil. The difference in the ploidy level of the two *Ramonda* species could be correlated to the more pronounced production and/or accumulation of squalene in *R. nathaliae*. Resurrection is a rare phenomenon in the plant kingdom and some volatiles, such as squalene, which is related to cholesterol biosynthesis, may be important in membrane con-

servation in anabiosis. It can be concluded that these essential oil poor *Ramonda* species have not developed an elaborate metabolic pathway for the production of specific volatiles but the identified constituents are made up of compounds originating from non-specific omnipresent pathways (triterpenoid steroid biosynthesis branch, oxylipin metabolism, oxidative degradation of carotenoids and fatty acids' pathways).

*Acknowledgements.* This work was funded by the Ministry of Science and Technological Development of the Republic of Serbia (Projects 143015 and 142054 B).

## ИЗВОД

ИСПАРЉИВИ КОНСТИТУЕНТИ ВЕГЕТАТИВНИХ ОРГАНА ПАЛЕОЕНДЕМИЧНИХ  
„ВАСКРСАВАЈУЋИХ“ БИЉНИХ ВРСТА *Ramonda serbica* PANČ. И  
*Ramonda nathaliae* PANČ. et PETROV.

НИКО С. РАДУЛОВИЋ<sup>1</sup>, ПОЛИНА Д. БЛАГОЈЕВИЋ<sup>1</sup>, РАДОСАВ М. ПАЛИЋ<sup>1</sup>,  
БОЈАН К. ЗЛАТКОВИЋ<sup>2</sup> И БРАНКА М. СТЕВАНОВИЋ<sup>3</sup>

<sup>1</sup>Одсек за хемију, Природно–математички факултет, Универзитет у Нишу, Вишеградска 33, 18000 Ниш,  
<sup>2</sup>Одсек за биологију и екологију, Природно–математички факултет, Универзитет у Нишу, Вишеградска 33,  
18000 Ниш и <sup>3</sup>Катедра за екологију и географију биљака, Институт за ботанику и ботаничка бајина  
„Јевремовац“, Биолошки факултет, Универзитет у Београду, Таковска 43, 11000 Београд

Етарска уља добијена хидродестилацијом листова и корена балканских ендеморелик-  
тних биљака *Ramonda serbica* и *Ramonda nathaliae*, као и етарски екстракти корена ових  
врста, анализирани су комбинацијом GC и GC/MS. Идентификоване су укупно 82 компо-  
ненте које су чиниле од 88,9 до 94,5 % уља, тј. екстраката. У свим анализираним уљима  
главна или једна од главних компоненти био је фенилетанал (20,5–57,1 %), у екстрактима  
присутан тек у занемарљивом проценту. Насупрот томе, екстракти обе врсте били су окарак-  
терисани високим садржајем сквалена (36,0% у *R. serbica* и 59,4 % у *R. nathaliae*) и стероида  
(27,4 % у *R. serbica* и 14,1 % у *R. nathaliae*). Сквален је био и најзаступљенија компонента у  
етарском уљу корена *R. nathaliae* (29,0 %), али није детектован у одговарајућем уљу врсте *R.*  
*serbica*. Поред тога, садржај масних киселина, упоредив у уљима и екстрактима корена обе  
анализиране врсте, знатно се разликовао у уљима добијеним из листова врста *R. serbica* и *R.*  
*nathaliae* (18,7 и 0,6 %). Презентовани резултати анализе испарљивих конституената *R.*  
*serbica* и *R. nathaliae* говоре по први пут о фитохемијској различитости ове две сродне, ен-  
демичне и реликтне врсте, указујући истовремено на њихове диференцијалне адаптивне одлике.

(Примљено 16. јула 2008)

## REFERENCES

1. N. Kosanin, *Spomenik Srp. Kralj. Akad.* **20** (1939) 1 (in Serbian)
2. K. F. Meyer, *Math. Naturwiss. Reiche* **19** (1970) 401
3. V. Stevanović, B. Stevanović, *Glas. Prir. Muz. B* **40** (1985) 75 (in Serbian)
4. V. Stevanović, M. Niketić, B. Stevanović, *Glas. Prir. Muz. B* **41** (1986) 89 (in Serbian)
5. V. Stevanović, M. Niketić, B. Stevanović, *Glas. Ins. Bot. Univerziteta u Beogradu* **20** (1986) 45 (in Serbian)
6. S. Siljak-Yakovlev, V. Stevanović, M. Tomasević, S. C. Brown, B. Stevanović, *Environ. Exp. Bot.* **62** (2008) 101

7. C. Sgherri, B. Stevanović, F. Navari-Izzo, *Physiol. Plant.* **122** (2004) 478
8. S. Canigüeral, B. M. Müller, M. J. Salvia, J. Iglesias, G. Franz, *Planta Med.* **60** (2008) 73
9. S. Canigüeral, M. J. Salvia, R. Vila, J. Iglesias, A. Virgili, T. Parella, *J. Nat. Prod.* **59** (1996) 419
10. M. Quartacci, O. Glisić, B. Stevanović, F. Navari-Izzo, *J. Exp. Bot.* **53** (2002) 2159
11. H. L. Citerne, M. Moller, Q. C. B. Cronk, *Ann. Bot.* **86** (2000) 167
12. F. X. Pico, M. Moller, N. J. Ouborg, Q. C. B. Cronk, *Plant Biol.* **4** (2002) 62
13. B. J. M. Zonneveld, I. J. Leitch, M. D. Bennett, *Ann. Bot.* **96** (2005) 229
14. P. K. Holmgren, N. H. Holmgren, L. C. Barnett, **120** (1990) 1, continuously updated at <http://sciweb.nybg.org/science2/IndexHerbariorum.asp>
15. H. Van Den Dool, P. D. Kratz, *J. Chromatogr.* **11** (1963) 463
16. R. P. Adams, *Identification of Essential Oil Components by Gas Chromatography/Mass Spectrometry*, 4<sup>th</sup> Ed., Allured Publishing Corporation, Carol Stream, IL, 2007
17. Y.-C. Oh, T. G. Hartman, C.-T. Ho, *J. Agric. Food Chem.* **40** (1992) 1878
18. B. A. Roy, R. A. Raguso, *Oecologia* **109** (1997) 414
19. A. Hanataka, T. Kajiwara, K. Matsui, *Z. Naturforsch. C* **50** (1995) 467
20. M. Maffei, F. Chailva, A. Codignola, *J. Essent. Oil Res.* **2** (1989) 57
21. M. A. Dessi, M. Deiana, B. W. Day, A. Rosa, S. Banni, F. P. Corongiu, *Eur. J. Lipid Sci. Technol.* **104** (2002) 506
22. M. Hartmann, *Trends Plant Sci.* **3** (1998) 170
23. M. Hartmann, P. Benveniste, *Methods Enzymol.* **148** (1987) 632
24. T. Devarenne, A. Ghosh, J. Chappell, *Plant Physiol.* **129** (2002) 1095
25. J. Rasbery, H. Shan, R. LeClair, M. Norman, S. Matsuda, B. Bartel, *J. Biol. Chem.* **282** (2007) 17002
26. V. Milovanović, N. Radulović, V. Mitić, R. Palić, G. Stojanović, *J. Essent. Oil Res.* **20** (2008) 310
27. N. Radulović, G. Stojanović, V. Milovanović, D. Djoković, V. Randjelović, *J. Essent. Oil Res.* **20** (2008) 437
28. M. Stefanello, A. Cervi, A. Wisniewski Jr., *Braz. J. Pharm.* **15** (2005) 331
29. L. Rodriguez-Hahn, J. Cardens, *Curr. Topics Phytochem.* **2** (1999) 91
30. C. Kapetanos, A. Karioti, S. Bojović, P. Marin, M. Veljić, H. Skaltsa, *Chem. Biodiversity* **5** (2008) 101
31. N. Radulović, B. Zlatković, R. Palić, G. Stojanović, *Nat. Prod. Commun.* **2** (2007) 453.



www.shd.org.rs

*J. Serb. Chem. Soc.* 74 (1) 45–52 (2009)  
JSCS–3807

JSCS@tmf.bg.ac.yu • www.shd.org.rs/JSCS

UDC 519.111:547.216–125  
*Original scientific paper*

## Q-Conjugacy character table for the non-rigid group of 2,3-dimethylbutane

MOHAMMAD REZA DARAFSHEH<sup>1</sup> and ALI MOGHANI<sup>2\*</sup>

<sup>1</sup>*School of Mathematics, College of Science, University of Tehran, Tehran and* <sup>2</sup>*Department of color physics, Institute for Colorants Paint and Coating (ICPC), Tehran, Iran*

(Received 9 April 2008)

**Abstract:** Maturated and unmaturated groups were introduced by the Japanese chemist Shinsaku Fujita, who used them in the markaracter table and the Q-conjugacy character table of a finite group. He then applied his results in this area of research to enumerate isomers of molecules. Using the non-rigid group theory, it was shown by the second author that the full non-rigid (f-NRG) group of 2,3-dimethylbutane is isomorphic to the group  $(Z_3 \times Z_3 \times Z_3 \times Z_3):Z_2$  of order 162 with 54 conjugacy classes. Here  $(Z_3 \times Z_3 \times Z_3 \times Z_3):Z_2$  denotes the semi direct product of four copies of  $Z_3$  by  $Z_2$ , where  $Z_n$  is a cyclic group of order  $n$ . In this paper, it is shown with the GAP program that this group has 30 dominant classes (similarly, Q-conjugacy characters) and that 24 of them are unmaturated (similarly, Q-conjugacy characters such that they are the sum of two irreducible characters). Then, the Q-conjugacy character table of the unmaturated full non-rigid group 2,3-dimethylbutane is derived.

**Keywords:** full non-rigid group; Q-conjugacy character; 2,3-dimethylbutane.

### INTRODUCTION

In order to develop new methods of combinatorial enumeration of isomers, some relationship between character tables containing characters for irreducible representations<sup>1,2</sup> and mark tables containing marks for coset representations were clarified by Shinsaku Fujita.<sup>3–14</sup>

Fujita proposed not only markaracter tables, which enable characters and marks to be discussed on a common basis,<sup>15,16</sup> but also Q-conjugacy character tables,<sup>7–9</sup> which are obtained for finite groups. The enumeration of chemical compounds has been accomplished by various methods but the Pólya–Redfield theorem has been a standard method for combinatorial enumerations of graphs and chemical compounds. A dominant class<sup>15</sup> is defined as a disjoint union of conjugacy classes that corresponds to the same cyclic subgroup, which is selected

\* Corresponding author. E-mail: moghani@icrc.ac.ir  
doi: 10.2298/JSC0901045D

as a representative of conjugate cyclic subgroups. Let  $G$  be a finite group and  $h_1, h_2 \in G$ . It is said that  $h_1, h_2$  are  $Q$ -conjugate if there exists  $t \in G$  such that  $t^{-1} = \langle h_1 \rangle$  and  $t = \langle h_2 \rangle$ . It is easy to see that the  $Q$ -conjugacy is an equivalence relation on  $G$  and generates equivalence classes which are called dominant classes, *i.e.*, the group  $G$  is partitioned into dominant classes as follows:  $G = K_1 + K_2 + \dots + K_s$  in which  $K_i$  corresponds to the cyclic (dominant) subgroup  $G_i$  selected from a non-redundant set of cyclic subgroups of  $G$  denoted by SCSG.<sup>15</sup>

Now, let  $C = C_{u \times u}$  be the matrix of the character table of the finite group  $G$ . Thereby, it is transformed to a more concise form called a  $Q$ -conjugacy character table, the  $s \times s$ -matrix of which is denoted by  $C^Q$  where  $s \leq u$ , as follows: If  $u = s$ , then  $C = C^Q$ , *i.e.*,  $G$  is a maturated group. Assuming  $s < u$ , then according to literature,<sup>7-9</sup> since the dimension of the  $Q$ -conjugacy character table of  $G$  and the corresponding markaracter table of  $G$  are equal,  $t = \varphi(|H|)/m(H)$  is set, where  $m(H)$  is maturity discriminate.<sup>10-16</sup>

If  $t = 1$  (*i.e.*,  $K_i$  is exactly a conjugacy class), then there is no reduction in the rows and columns of  $C$  but, if  $t > 1$  ( $K_i$  is a union of  $t$ -conjugacy classes of  $G$ , *i.e.*, a reduction in the correspondence columns in the character table  $C$ ), the sum of the  $t$ -rows of the irreducible characters *via* the same degree in  $C$  (reduction in rows) gives a reducible character, which are called  $Q$ -conjugacy characters in both cases.

A rigid molecule is defined as being such that the barriers between its versions are insuperable and there are no observable tunneling splittings. For non-rigid molecules, there are one or more contortional large amplitude vibrations, such as inversion or internal rotation that give rise to tunneling splittings. Due to this deformability, non-rigid molecules exhibit some interesting properties of intramolecular dynamics, which can be more easily studied by resorting to group theory. The group theory for non-rigid molecules finds numerous applications ranging from rovibronic spectroscopy of molecules exhibiting large amplitude motions, chemical reactions to dynamic stereochemistry to weakly-bound van der Waals complexes. Following the pioneering works of Longuet-Higgins,<sup>19</sup> the symmetry group of a non-rigid molecule group consists of all permutations and permutation-inversion operations, which become feasible as molecules tunnel through a number of potential energy maxima separated by multiple minima. Subsequently, several other workers<sup>19-32,34-36</sup> formulated different ways of characterizing non-rigid groups (NRG).

The complete set of molecular conversion operations which commute with the nuclear motion operator contains overall rotation operations, describing the molecule rotating as a whole, and non-rigid tunneling motion operations, describing molecular moieties moving with respect to the rest of the molecule. Such a set forms a group, which is called the full non-rigid group (f-NRG). Longuet-Higgins<sup>19</sup> investigated the symmetry groups of non-rigid molecules, where

changes from one conformation to another can occur easily. The method as described here is appropriate for molecules which consist of a number of CH<sub>3</sub> groups attached to a rigid framework.

The present study investigates Q-conjugacy character tables of the f-NRG of 2,3-dimethylbutane. The motivation for this study is also outlined in literature,<sup>26–36</sup> and the reader is encouraged to consult these papers for background material as well as basic computational techniques with the aid of GAP.<sup>33</sup> For instance, an algorithm to work with big chemical graphs, such as the big fullerene C<sub>80</sub>, was introduced by the second author<sup>29,35</sup> and a Q-conjugacy character table for the f-NRG of tetra-amine platinum (II) was presented.<sup>36</sup>

The symmetry groups of 2,3-dimethylbutane was found as a semi-direct product by the first author (see Fig. 1).<sup>30</sup> In the present paper, it is shown that the f-NRG of 2,3-dimethylbutane is an unmatured group of order 162 with 30 dominant classes (similarly, Q-conjugacy characters), such that there are 24 unmatured (*i.e.*, there are 24 row (column) reductions in the character table of the f-NRG of 2,3-dimethylbutane).

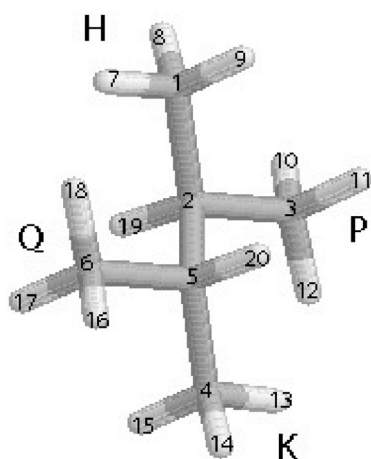


Fig. 1. Structure of 2,3-dimethylbutane.

#### COMPUTATIONAL METHOD AND DISCUSSION

A permutation representation  $P$  of a finite group  $G$  is obtained when the group  $G$  acts on a finite set  $X = \{x_1, x_2, \dots, x_t\}$  from the right, which means that the following mapping is given:

$P: X \times G \rightarrow X$  via  $(x, g) \rightarrow xg$  such that the following holds:  $(xg)g' = x(gg')$  and  $x_1 = x$ , for each  $g, g' \in G$  and  $x \in X$ . Now let it be assumed that an action  $P$  of  $G$  on  $X$  and a subgroup  $H$  of  $G$  are given. Considering the set of its right cosets  $Hg_i$  and the corresponding partition of  $G$  into these cosets:  $G = Hg_1 + Hg_2 + \dots + Hg_m$ .

If the cosets from the right are multiplied by a group element  $g$ , these cosets are permuted. In fact, one obtains an action of  $G$  on the set  $X$  of cosets and cor-

respondingly a permutation representation which is denoted by  $G(H)$ , following Fujita's notation.

If  $M$  is a normal subgroup of  $G$  and  $K$  is another subgroup of  $G$  such that  $M \cap K = \{e\}$  and  $G = MK = \langle M, K \rangle$ , then  $G$  is called a semi-direct product of  $K$  by  $M$  denoted by  $K:M$ .

The first author described<sup>30</sup> that the f-NRG of 2,3-dimethylbutane is isomorphic to the semidirect product of four copies of  $Z_3$  by  $Z_2$ , where  $Z_n$  is a cyclic group of order  $n$ , as follows: using numbers  $\{1,2,3,4,5,6\}$  to indicate the carbon atoms, the numbers  $\{7,8,9\}$  to label the three hydrogen atoms on the 1 corner and  $\{10,11,12\}$  to label the hydrogen atoms on the 3 corner and so on, see Fig. 1, then the symmetry of order 2 of the framework in terms of permutations is:  $\sigma = (1,4)(2,5)(3,6)(7,13)(8,14)(9,15)(10,16)(11,17)(12,18)(19,20)$ .

The group of symmetries of each  $\text{CH}_3$  group in terms of a generating system is:  $H = \langle (7,8,9) \rangle$ ,  $K = \langle (13,14,15) \rangle$ ,  $P = \langle (10,11,12) \rangle$  and  $Q = \langle (16,17,18) \rangle$ .

Since the effect of  $\sigma$  on the carbon atoms is not needed, its effect on the hydrogen atoms is considered, *i.e.*,  $\sigma' = (7,13)(8,14)(9,15)(10,16)(11,17)(12,18)$ . Therefore, the f-NRG of this molecule in terms of generators is  $G = \langle \theta_1, \theta_2, \theta_3, \theta_4, \sigma' \rangle$ , where  $\theta_1 = (7,8,9)$ ,  $\theta_2 = (13,14,15)$ ,  $\theta_3 = (10,11,12)$  and  $\theta_4 = (16,17,18)$ .

The computations of the symmetry properties of the molecules were carried out using of GAP.<sup>33</sup> GAP stands for Groups, Algorithms and Programming. The name was chosen to reflect the aim of the system, which is group theoretical software for solving computational problems in computational group theory. This software was constructed by the GAP team in Aachen. GAP is a free and extendable software package.

Now, at the prompt of GAP, the following program was run to compute the character table and the set SCSSG of the f-NRG of 2,3-dimethylbutane  $D = (Z_3 \times Z_3 \times Z_3 \times Z_3):Z_2$  as follow:

```
LogTo("Computations.txt");
a := (7,8,9);
b := (10,11,12);
c := (13,14,15);
d := (16, 17, 18);
e := (7,13)(8,14)(9,15)(10,16) (11,17)(12,18);
D := GroupWithGenerators(a,b,c,d,e);
Char := CharacterTable(D);
Order(D);IsPermGroup(D);
s:=ConjugacyClassesSubgroups(D);
Sort("s");
SCSSG:=List(ConjugacyClassesSubgroups(G),x->Elements(x));
Len:=Length(a); y:=[];
```

```

for i in [1,2...z]do
  if IsCyclic(a[i])then Add(y,i);
fi;
od;
Display(Char);
Display(s);
Print("Char", "\n");
Print("SCSG", "\n");
LogTo( );

```

In addition, since the dimensions of the Q-conjugacy character table of  $D = (Z_3 \times Z_3 \times Z_3 \times Z_3):Z_2$  and its corresponding markaracter table<sup>7-9</sup> are equal,  $|SCSG| = 30$ .

Now, on running the program, it can be seen that D has exactly 30 dominant (Q-conjugacy) classes as follow:

$K_1 = 1a$ ,  $K_2 = 2a$ ,  $K_3 = 3a \cup 3b$ ,  $K_4 = 3c \cup 3f$ ,  $K_5 = 3d \cup 3h$ ,  $K_6 = 3e \cup 3g$ ,  $K_7 = 3i \cup 3q$ ,  $K_8 = 3j$ ,  $K_9 = 3k \cup 3u$ ,  $K_{10} = 3l \cup 3w$ ,  $K_{11} = 3m \cup 3v$ ,  $K_{12} = 3n \cup 3r$ ,  $K_{13} = 3o \cup 3t$ ,  $K_{14} = 3p \cup 3s$ ,  $K_{15} = 3x \cup 3am$ ,  $K_{16} = 3y \cup 3ao$ ,  $K_{17} = 3z \cup 3an$ ,  $K_{18} = 3aa$ ,  $K_{19} = 3ab \cup 3aj$ ,  $K_{20} = 3ac \cup 3af$ ,  $K_{21} = 3ad \cup 3ar$ ,  $K_{22} = 3ae \cup 3aq$ ,  $K_{23} = 3ag \cup 3al$ ,  $K_{24} = 3ah$ ,  $K_{25} = 3ai \cup 3ap$ ,  $K_{26} = 3ak$ ,  $K_{27} = 6a \cup 6b$ ,  $K_{28} = 6c \cup 6f$ ,  $K_{29} = 6d \cup 6h$ ,  $K_{30} = 6e \cup 6g$ .

Here, just  $K_1$ ,  $K_2$ ,  $K_8$ ,  $K_{18}$ ,  $K_{24}$  and  $K_{26}$  are matured dominant classes (similar discussion for Q-conjugacy characters). Therefore, by the above computations, the Q-conjugacy character table ( $C^Q$ ) of group  $D = (Z_3 \times Z_3 \times Z_3 \times Z_3):Z_2$ , which are stored in Table I and II, can be introduced. More details are given in the literature.<sup>37</sup>

TABLE I. Q-conjugacy character table from  $K_1$  to  $K_{15}$  of the f-NRG of 2,3-dimethylbutane

$C^Q$	$K_1$	$K_2$	$K_3$	$K_4$	$K_5$	$K_6$	$K_7$	$K_8$	$K_9$	$K_{10}$	$K_{11}$	$K_{12}$	$K_{13}$	$K_{14}$	$K_{15}$
$\phi_1$	1	1	1	1	1	1	1	1	1	1	1	1	1	1	1
$\phi_2$	1	1	1	1	1	1	1	1	1	1	1	1	1	1	1
$\phi_3$	2	2	-1	-1	-1	2	2	-1	-1	-1	-1	-1	-1	-1	-1
$\phi_4$	2	2	-1	-1	-1	2	2	-1	-1	-1	-1	-1	-1	-1	-1
$\phi_5$	2	-1	2	-1	-1	-1	2	-1	2	-1	-1	-1	2	2	-1
$\phi_6$	2	-1	2	-1	-1	-1	2	-1	-1	2	-1	-1	2	2	-1
$\phi_7$	2	-1	-1	-1	2	-1	2	-1	2	-1	2	-1	-1	-1	2
$\phi_8$	2	-1	-1	-1	2	-1	2	-1	2	-1	2	-1	-1	-1	2
$\phi_9$	2	-1	-1	2	-1	-1	2	2	-1	-1	-1	2	-1	-1	-1
$\phi_{10}$	2	-1	-1	2	-1	-1	2	2	-1	-1	-1	2	-1	-1	-1
$\phi_{11}$	2	-1	2	-1	-1	2	-1	-1	2	-1	-1	2	-1	2	-1
$\phi_{12}$	2	2	-1	-1	-1	2	2	-1	-1	-1	-1	-1	-1	2	2
$\phi_{13}$	2	-1	-1	-1	2	2	-1	2	-1	-1	-1	-1	2	2	-1
$\phi_{14}$	2	-1	-1	2	-1	2	-1	-1	-1	2	2	-1	-1	2	-1
$\phi_{15}$	4	-2	-2	1	1	4	-2	1	-2	1	1	-2	1	-2	1

TABLE I. Continued

$C^Q$	$K_1$	$K_2$	$K_3$	$K_4$	$K_5$	$K_6$	$K_7$	$K_8$	$K_9$	$K_{10}$	$K_{11}$	$K_{12}$	$K_{13}$	$K_{14}$	$K_{15}$
$\phi_{16}$	4	1	-2	1	-2	-2	-2	1	4	1	-2	-2	1	-2	-2
$\phi_{17}$	4	1	-2	-2	1	-2	-2	-2	-2	1	1	4	1	-2	1
$\phi_{18}$	4	1	4	1	1	-2	-2	1	-2	-2	1	-2	-2	4	1
$\phi_{19}$	4	4	1	1	1	4	4	1	1	1	1	1	1	-2	-2
$\phi_{20}$	4	-2	1	1	-2	-2	4	1	-2	1	-2	1	1	-2	4
$\phi_{21}$	4	-2	1	-2	1	-2	4	-2	1	1	1	-2	1	-2	-2
$\phi_{22}$	4	-2	-2	1	1	-2	4	1	1	-2	-1	-1	-2	4	-2
$\phi_{23}$	4	-2	1	1	-2	4	-2	-2	1	1	1	1	-2	-2	1
$\phi_{24}$	4	-2	1	-2	1	4	-2	1	1	-2	-2	1	1	-2	1
$\phi_{25}$	4	1	-2	1	-2	-2	-2	-2	1	-2	1	1	4	4	1
$\phi_{26}$	4	1	-2	-2	1	-2	-2	1	1	4	-2	1	-2	4	1
$\phi_{27}$	4	1	1	1	4	-2	-2	-2	-2	1	-2	1	-2	-2	-2
$\phi_{28}$	4	1	1	-2	-2	-2	-2	1	-2	-2	4	1	1	-2	-2
$\phi_{29}$	4	1	1	-2	-2	-2	-2	4	1	1	1	-2	-2	-2	1
$\phi_{30}$	4	1	1	4	1	-2	-2	-2	1	-2	-2	-2	1	-2	1

Table II. Q-conjugacy character table from  $K_{16}$  to  $K_{30}$  of the f-NRG of 2,3-dimethylbutane

$C^Q$	$K_{16}$	$K_{17}$	$K_{18}$	$K_{19}$	$K_{20}$	$K_{21}$	$K_{22}$	$K_{23}$	$K_{24}$	$K_{25}$	$K_{26}$	$K_{27}$	$K_{28}$	$K_{29}$	$K_{30}$
$\phi_1$	1	1	1	1	1	1	1	1	1	1	1	1	1	1	1
$\phi_2$	1	1	1	1	1	1	1	1	1	1	-1	-1	-1	-1	-1
$\phi_3$	-1	2	2	2	-1	-1	2	2	-1	2	-2	-2	1	1	1
$\phi_4$	-1	2	2	2	-1	-1	2	2	-1	2	2	2	-1	-1	-1
$\phi_5$	-1	2	-1	-1	-1	2	-1	2	-1	2	-2	1	-2	1	1
$\phi_6$	-1	2	-1	-1	-1	2	-1	2	-1	2	2	-1	2	-1	-1
$\phi_7$	-1	2	-1	-1	-1	-1	-1	2	2	2	-2	1	1	1	-2
$\phi_8$	-1	2	-1	-1	-1	-1	-1	2	2	2	2	-1	-1	-1	2
$\phi_9$	2	2	-1	-1	2	-1	-1	2	-1	2	-2	1	1	-2	1
$\phi_{10}$	2	2	-1	-1	2	-1	-1	2	-1	2	2	-1	-1	2	-1
$\phi_{11}$	-1	2	-1	-1	2	-1	2	-1	2	-1	0	0	0	0	0
$\phi_{12}$	2	-1	-1	-1	2	2	-1	-1	2	-1	0	0	0	0	0
$\phi_{13}$	-1	-1	-1	2	2	-1	-1	-1	2	2	0	0	0	0	0
$\phi_{14}$	-1	-1	2	-1	2	-1	-1	2	2	-1	0	0	0	0	0
$\phi_{15}$	1	4	-2	-2	-2	1	4	-2	-2	-2	0	0	0	0	0
$\phi_{16}$	1	4	1	1	-2	1	-2	-2	4	-2	0	0	0	0	0
$\phi_{17}$	-2	4	1	1	4	1	-2	-2	-2	-2	0	0	0	0	0
$\phi_{18}$	1	4	1	1	-2	-2	-2	-2	-2	-2	0	0	0	0	0
$\phi_{19}$	-2	-2	-2	-2	-2	-2	-2	-2	-2	-2	0	0	0	0	0
$\phi_{20}$	-2	-2	1	1	-2	-2	1	-2	4	-2	0	0	0	0	0
$\phi_{21}$	4	-2	1	1	4	-2	1	-2	-2	-2	0	0	0	0	0
$\phi_{22}$	-2	-2	1	1	-2	4	1	-2	-2	-2	0	0	0	0	0
$\phi_{23}$	1	-2	4	4	2	1	-2	-2	-2	4	0	0	0	0	0
$\phi_{24}$	1	-2	4	-2	-2	1	-2	4	-2	-2	0	0	0	0	0
$\phi_{25}$	1	-2	1	-2	-2	-2	1	-2	-2	4	0	0	0	0	0
$\phi_{26}$	1	-2	-2	1	-2	-2	1	4	-2	-2	0	0	0	0	0

TABLE 2. Continued

$C^Q$	$K_{16}$	$K_{17}$	$K_{18}$	$K_{19}$	$K_{20}$	$K_{21}$	$K_{22}$	$K_{23}$	$K_{24}$	$K_{25}$	$K_{26}$	$K_{27}$	$K_{28}$	$K_{29}$	$K_{30}$
$\phi_{27}$	1	-2	1	-2	-2	1	1	-2	4	4	0	0	0	0	0
$\phi_{28}$	1	-2	-2	1	-2	1	1	4	4	-2	0	0	0	0	0
$\phi_{29}$	-2	-2	1	-2	4	1	1	-2	-2	4	0	0	0	0	0
$\phi_{30}$	-2	-2	-2	1	4	1	1	4	-2	-2	0	0	0	0	0

The derived Q-conjugacy character tables could also be valuable in other applications, such as in the context of chemical applications of graph theory and aromatic compounds.<sup>10-14</sup>

## ИЗВОД

ТАБЛИЦА КАРАКТЕРА Q-КОНЈУГАЦИЈЕ ЗА НЕРИГИДНУ ГРУПУ СИМЕТРИЈЕ  
2,3-ДИМЕТИЛБУТАНА

MOHAMMAD REZA DARAFSHEH<sup>1</sup> и ALI MOGHANI<sup>2</sup>

<sup>1</sup>*School of Mathematics, College of Science, University of Tehran, Tehran, Iran* и <sup>2</sup>*Department of color physics, Institute for Colorants Paint and Coating (ICPC), Tehran, Iran*

Јапански хемичар Shinsaku Fujita увео је матуриране и нематуриране групе, које је користио у теорији таблица марк-карактера и таблица карактера Q-конјугације коначних група. Он је онда применио ове резултате за пребројавање изомера. Користећи теорију неригидних група, један од садашњих аутора показао је да је потпуна неригидна група (f-NRG) 2,3-диметилбутана изоморфна са групом  $(Z_3 \times Z_3 \times Z_3 \times Z_3):Z_2$  реда 162 са 54 класа конјугације. Овде  $(Z_3 \times Z_3 \times Z_3 \times Z_3):Z_2$  означава семидиректни производ четири копије групе  $Z_3$  са групом  $Z_2$ , где је  $Z_n$  циклична група реда  $n$ . У овом раду је применом програма GAP показано да ова група има 30 доминантних класа (односно карактера Q-конјугације), и да су 24 од њих нематуриране (односно карактери Q-конјугације су збир два иредуцибилна карактера). Након тога, одређена је таблица катактера Q-конјугације за нематурирану потпуну неригидну групу симетрије 2,3-диметилбутана.

(Примљено 9. априла 2008)

## REFERENCES

1. F. A. Cotton, *Chemical Application of Group Theory*, Wiley-International, New York, 1971
2. I. Hargittai, H. Hargitta, *Symmetry through the Eyes of a Chemist*, VCH, Weinheim, 1986
3. S. Fujita, *J. Math. Chem.* **12** (1999) 173
4. S. Fujita, *J. Graph Theory* **18** (1994) 349
5. S. Fujita, *J. Org. Chem.* **67** (2002) 6055
6. S. Fujita, *J. Comput. Chem. Jpn.* (2004) 113
7. S. Fujita, *Bull. Chem. Soc. Japan* **71** (1998) 2071
8. S. Fujita, *Bull. Chem. Soc. Japan* **71** (1998) 2309
9. S. Fujita, *Bull. Chem. Soc. Japan* **71**(1998) 1587
10. S. Fujita, *MATCH Commun. Math. Comput. Chem.* **54** (2005) 251
11. S. Fujita, *MATCH Commun. Math. Comput. Chem.* **55** (2006) 5
12. S. Fujita, *MATCH Commun. Math. Comput. Chem.* **55** (2006) 237
13. S. Fujita, *MATCH Commun. Math. Comput. Chem.* **57** (2007) 5

14. S. Fujita, *Diagrammatical Approach to Molecular Symmetry and Enumeration of Stereoisomers*, MCM, Kragujevac, 2007
15. S. Fujita, *Theor. Chim. Acta* **91** (1995) 291
16. S. Fujita, *Theor. Chim. Acta* **91** (1995) 315
17. A. Kerber, *MATCH Commun. Math. Comput. Chem.* **46** (2002) 151
18. M. R. Darafsseh, Y. Farjami, A. R. Ashrafi, *Acta Chim. Slov.* **52** (2005) 282
19. H. C. Longuet-Higgins, *Mol. Phys.* **6** (1963) 445
20. Y. G. Smeyers, *Adv. Quantum. Chem.* **24** (1992) 1
21. S. L. Altmann, *Induced Representation in Crystal & Molecules*, Academic Press, London, 1977
22. P. R. Bunker, *Molecular Symmetry in Spectroscopy*, Academic Press, New York, 1979
23. J. S. Lomont, *Applications of Finite Groups*, Academic, New York, 1959
24. A. J. Stone, *J. Chem. Phys.* **41** (1964) 1568
25. Y. G. Smeyers, M. Villa, *J. Math. Chem.* **28** (2000) 377
26. K. Balasubramanian, *J. Phys. Chem.* **10** (2004) 5527
27. K. Balasubramanian, *Chem. Phys. Lett.* **391** (2004) 64
28. K. Balasubramanian, *Chem. Phys. Lett.* **398** (2004) 15
29. A. Moghani, S. Naghdi, A. R. Ashrafi, A. Ahmadi, *London Math. Soc.* **340** (2007) 630
30. M. R. Darafsseh, A. Darafsseh, A. R. Ashrafi, *MATCH Commun. Math. Comput. Chem.* **58** (2007) 47
31. M. R. Darafsseh, A. Darafsseh, A. R. Ashrafi, *Int. J. Quantum Chem.* **107** (2007) 340
32. M. R. Darafsseh,; A. R. Ashrafi, A. Darafsseh, *Chem. Phys. Lett.* **421** (2006) 566
33. GAP, Groups, Algorithms and Programming, Lehrstuhl De für Mathematik, RWTH, Aachen, <http://www.gap-system.org> (1995)
34. M. R. Darafsseh, Y. Farjami, A. R. Ashrafi, M. Hamadani, *J. Math. Chem.* **41** (2007) 315
35. A. Moghani, A. R. Ashrafi, *Croat. Chem. Acta* **79** (2006) 465
36. A. Moghani, *J. Serb. Chem. Soc.* **73** (2008) 189
37. M. R. Darafsseh, A. Moghani, *Bull. Chem. Soc. Japan* (2008), in press.



www.shd.org.rs

*J. Serb. Chem. Soc.* 74 (1) 53–60 (2009)  
JSCS–3808

Journal of  
the Serbian  
Chemical Society

JSCS@tmf.bg.ac.yu • www.shd.org.rs/JSCS

UDC 544.773.42+536.46+661.873:542.913:  
:543.57:535.42

*Original scientific paper*

## Gel-combustion synthesis of $\text{CoSb}_2\text{O}_6$ and its reduction to powdery $\text{Sb}_2\text{Co}$ alloy

MAJA JOVIĆ<sup>1</sup>, MARINA DAŠIĆ<sup>1</sup>, KONRAD HOLL<sup>2</sup>,  
DEJAN ILIĆ<sup>2</sup> and SLAVKO MENTUS<sup>1\*</sup>

<sup>1</sup>University of Belgrade, Faculty of Physical Chemistry, Studentski trg 1, 11000 Belgrade, Serbia and <sup>2</sup>Varta Microbattery GMBH, Daimlerstrasse 1, 73479 Ellwangen, Germany

(Received 7 May, revised 20 June 2008)

**Abstract:**  $\text{Sb}_2\text{Co}$  alloy in powdery form was synthesized *via* reduction with gaseous hydrogen of the oxide  $\text{CoSb}_2\text{O}_6$ , obtained by the citrate gel-combustion technique. The precursor was an aqueous solution of antimony nitrate, cobalt nitrate and citric acid. The precursor solution with mole ratio  $\text{Co(II)/Sb(V)}$  of 1:2 was gelatinized by evaporation of water. The gel was heated in air up to the temperature of self-ignition. The product of gel combustion was a mixture of oxides and it had to be additionally thermally treated in order to be converted to pure  $\text{CoSb}_2\text{O}_6$ . The reduction of  $\text{CoSb}_2\text{O}_6$  by gaseous hydrogen yielded powdery  $\text{Sb}_2\text{Co}$  as the sole phase. The process of oxide reduction to alloy was controlled by thermogravimetry, while X-ray diffractometry was used to control the phase compositions of both the oxides and alloys.

**Keywords:**  $\text{CoSb}_2\text{O}_6$ ;  $\text{Sb}_2\text{Co}$ ; gel-combustion; intermetallic compound; thermogravimetry; X-ray diffraction.

### INTRODUCTION

Sol–gel techniques and their variances: gel-combustion techniques, are widely used to produce nano-dispersed, simple or combined, oxides serving as high temperature superconductors,<sup>1</sup> ferrites,<sup>2,3</sup> electrode materials for lithium batteries,<sup>4</sup> catalysts,<sup>5,6</sup> *etc.* The reduction of oxides by heating in a hydrogen atmosphere presents an already known procedure of powder metallurgy, enabling the synthesis of powders of pure metals or alloys.<sup>7–15</sup>

Sol–gel techniques, being faster and more effective, are replacing more and more classical solid-state synthesis procedures. Namely, the low mobility of atoms in solids is the basic obstacle in the synthesis of solid materials through classic solid-state reactions, where the relatively coarse starting mixtures of the solid compounds require either a long time or high temperatures to achieve interdiffu-

\* Corresponding author. E-mail: slavko@ffh.bg.ac.yu  
doi: 10.2298/JSC0901053J

sional homogenization on the molecular level. Sol–gel techniques enable intimate precursor mixtures that are homogeneous on the molecular level to be obtained, leading to a final product with only little additional treatment. The citrate gel-combustion method was already used to synthesize the complex oxide compounds  $\text{LiMn}_2\text{O}_4$ <sup>4</sup> and  $\text{NiWO}_4$ ,<sup>16</sup> while a two-step procedure, involving both gel-combustion synthesis of oxide mixtures and their reduction to alloys, was used recently to obtain Ni–W<sup>16</sup> and Ni–Mo<sup>17</sup> alloys. The hypothesis underlying this two-step route may be expressed as follows: the gel-combustion procedure provides a mixture of oxides homogeneous on the molecular level, which yields immediately a thermodynamically stable alloy upon reduction. This idealized performance assumes low temperature synthesis of an alloy without the need for any additional thermal treatment to relax its structure.

The intermetallic compound  $\text{CoSb}_2$  is a representative of the arsenopyrite class of compounds.<sup>18</sup> This alloy is also known as a semiconductor material of relatively low thermal conductivity and high thermoelectric power.<sup>19,20</sup> For semiconductor investigations, large crystals of  $\text{CoSb}_2$  were synthesized earlier by Feschotte *et al.*<sup>20</sup> by the gradient-freeze technique. The intermetallic compound  $\text{CoSb}_2$  recently became additionally interesting as an anodic material for Li-ion batteries, being of high theoretical Faradic capacity (amounting to even  $530 \text{ mA g}^{-1}$ ), as well as nice cyclability, if prepared in a nano-dispersed or amorphous form.<sup>21–25</sup> Xie *et al.*<sup>22</sup> published the synthesis of a nano-dispersed alloy based on levitation melting and ball milling of the solidified bulk alloy. Somewhat later, Xie *et al.*<sup>23</sup> published the solvothermal synthesis, in which a solution of  $\text{CoCl}_2 \cdot 6\text{H}_2\text{O}$ ,  $\text{SbCl}_3$  and  $\text{NaBH}_4$  in anhydrous ethanol was placed in an autoclave and thermostated for a certain time, whereby  $\text{Sb}_2\text{Co}$  alloy as a precipitate, which was filtered, washed and vacuum-dried, was obtained.

The intention of the present study was to synthesize  $\text{Sb}_2\text{Co}$  alloy in the powdery form by reduction of a mixed oxide  $\text{CoO–Sb}_2\text{O}_5$  synthesized by combustion of the corresponding citrate gel. This was an attempt to surmount the disadvantages of the classic metallurgical melt-solidification route, which requires closed conditions due to a pronounced ability of antimony to sublime,<sup>22,25</sup> as well as to avoid the relatively complex solvothermal synthesis.<sup>23</sup>

#### EXPERIMENTAL

The chemicals used in this study: Sb,  $\text{Co}(\text{NO}_3)_2 \cdot 6\text{H}_2\text{O}$  and citric acid, were purchased from Merck. 1 g of metallic powdery Sb (8.214 mmol) was mixed with 5.178 g of citric acid (24.6 mmol) and 1 ml of concentrated nitric acid, and 2 ml of distilled water was added. The antimony was dissolved quantitatively under slight heating. Then 1.1952 g  $\text{Co}(\text{NO}_3)_2 \cdot 6\text{H}_2\text{O}$  (4.107 mmol) was added to the solution to obtain a mole ratio Sb:Co of 2:1. The solution was dried at 80 °C for 24 h to gelatinize. The dry gel was heated in air up to self-ignition, which occurred at about 300 °C, yielding a dark-gray powder, which was expected to be the oxide mixture. This powder was isothermally treated for 30 min in air at a predetermined temperature, in order to remove traces of carbon, which also unavoidably consolidated the crystal

structure. A small part of the oxide sample was used to prove thermogravimetrically the conditions of reduction with gaseous hydrogen. A TA Instruments Model 2090 TG-DTA device was used to obtain a TG curve under a flow of the gas mixture Ar +  $\text{H}_2$  (25 vol.%). From the TG curve, the final temperature of reduction was determined. Then, the whole oxide mass was placed in a quartz tube which was protruded through a horizontal furnace and the reduction gas stream (Ar +  $\text{H}_2$  (25 vol.%)), at a constant flow rate of  $70 \text{ ml min}^{-1}$ , was established through the tube. After heating up to the temperature required for complete reduction, a gray powder was obtained, which was expected to be  $\text{Sb}_2\text{Co}$ . X-Ray analysis for the purposes of this study was performed by means of a Philips PW 1710 diffractometer, using  $\text{CuK}_{\alpha 1,2}$  line ( $\lambda = 1.54056 \text{ \AA}$ ) in the  $15\text{--}70^\circ 2\theta$  range, in steps of  $0.05^\circ$  with an exposition of 3 s. The morphology of alloy was observed using a Jeol JSM-840A scanning electron microscope.

### RESULTS AND DISCUSSION

As is known from inorganic chemistry,  $\text{CoO}$  and  $\text{Sb}_2\text{S}_5$  may form the complex oxide compound  $\text{CoSb}_2\text{O}_6$ . This compound was expected to be the direct product of the gel-combustion synthesis described in the Experimental section, in view of the hypothesis that the gel-combustion procedure provides homogenization on a molecular level. The powdery product of the gel-combustion procedure described in the Experimental section was treated isothermally at  $700^\circ\text{C}$  during 30 min in order to remove traces of carbon and then was subjected to X-ray diffraction analysis in order to examine the phase composition. The XRD diffractogram (Fig. 1) evidenced not only the expected pure  $\text{CoSb}_2\text{O}_6$ , but a mixture of  $\text{CoSb}_2\text{O}_6$ ,  $\text{Sb}_2\text{O}_3$  and  $\text{CoO}$ , which were identified based on JCPDS cards 18-0403, 72-1854, and 75-0418,<sup>26</sup> respectively. The appearance of the compound  $\text{CoSb}_2\text{O}_6$  confirms the expectation that the gel-combustion procedure leads to a very intimate mixture of oxides, able to react mutually and to build a thermodynamically stable compound. However, the appearance of free simple oxides indicates that the temperature developed during the gel combustion was insufficient to provide

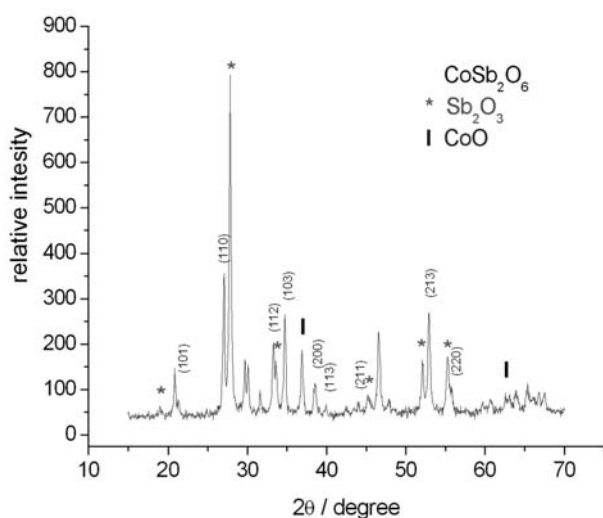


Fig. 1. X-Ray diffractogram of the oxide mixture obtained by citrate gel-combustion, upon thermal treatment at  $500^\circ\text{C}$ . The diffraction lines of  $\text{CoSb}_2\text{O}_6$ ,  $\text{Sb}_2\text{O}_3$  and  $\text{CoO}$  are labeled by Miller indices ( $\text{CoSb}_2\text{O}_6$ ) or by marks, shown in the inserted legend.

for complete conversion of simple oxides to their product,  $\text{CoSb}_2\text{O}_6$ . The appearance of the lower-valence oxide  $\text{Sb}_2\text{O}_3$  is most probably due to the partial reduction of  $\text{Sb}_2\text{O}_5$  by the carbon appearing as a product of incomplete combustion of citric acid.

In order to examine whether the obtained oxide mixture, in spite of its complexity, may yield the expected  $\text{Sb}_2\text{Co}$  alloy, the complete product of gel-combustion was subjected to reduction. Namely, the lower the temperature used in the procedure, the lower is the expected mean particle radius of resulting product.

The procedure of reduction was checked first by thermogravimetry. For this purpose, the oxide mixture was subjected to reduction within a thermobalance, in a stream of the gaseous mixture  $\text{Ar} + \text{H}_2$  (25 %). The mass change during linearly programmed heating is shown in Fig. 2. Obviously, reduction accompanied by mass loss proceeds in one step and finishes at 650 °C. This TG curve shows that the mass loss amounts to 20 %, confirming that a part of the Sb existed as  $\text{Sb}_2\text{O}_3$  in the initial product. Namely, the mass loss which corresponds to the conversion  $\text{CoSb}_2\text{O}_6 \rightarrow \text{Sb}_2\text{Co}$  amounts to 24 %. The TG data in Fig. 2 show that a temperature of at least 650 °C is required to finalize the reduction of the oxides. Bearing this fact in mind, the whole amount of the oxide product obtained by gel-combustion was reduced in a stream of the gaseous mixture  $\text{Ar} + \text{H}_2$  (25 vol.%) at 800 °C, and then cooled to room temperature, keeping it permanently under the reducing gas stream to avoid re-oxidation.

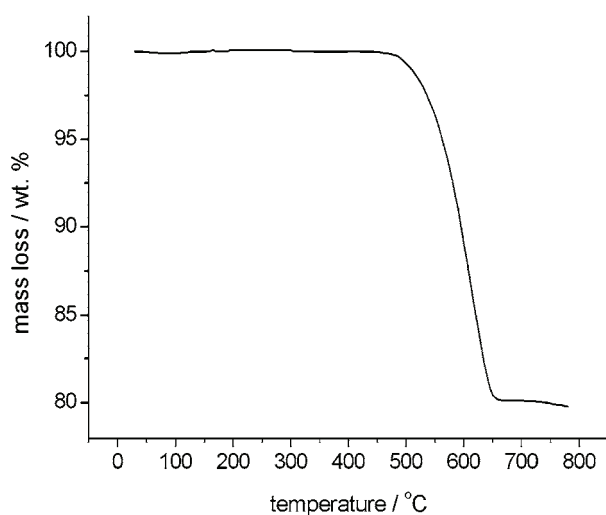


Fig. 2. Thermogravimetric curve obtained during the heating of the oxide mixture  $\text{CoSb}_2\text{O}_6$ ,  $\text{Sb}_2\text{O}_3$  and  $\text{CoO}$  in an  $\text{Ar} + \text{H}_2$  (25 vol. %) stream at a heating rate of  $15\text{ °C min}^{-1}$ .

The X-ray diffractogram of the obtained alloy, shown in Fig. 3, evidences that the resulting alloy was a mixture of  $\text{Sb}_2\text{Co}$  (monoclinic, JCPDS card No. 29-0126)<sup>26</sup> and  $\text{SbCo}$  (JCPDS card No 33-0097).<sup>26</sup> On the basis of the relative intensities,  $\text{Sb}_2\text{Co}$  was in excess. A real explanation for the complexity of the phase composition illustrated in Fig. 3 is the presence of simple oxides in the

initial oxide mixture, as visible in Fig. 1. At least, free antimony oxide present in the initial mixture yields elementary Sb during reduction, which may evaporate at 800 °C and deteriorate the expected mole ratio Sb:Co of 2:1. This explains the appearance of  $\text{SbCo}$  besides of  $\text{Sb}_2\text{Co}$  in the final alloy.

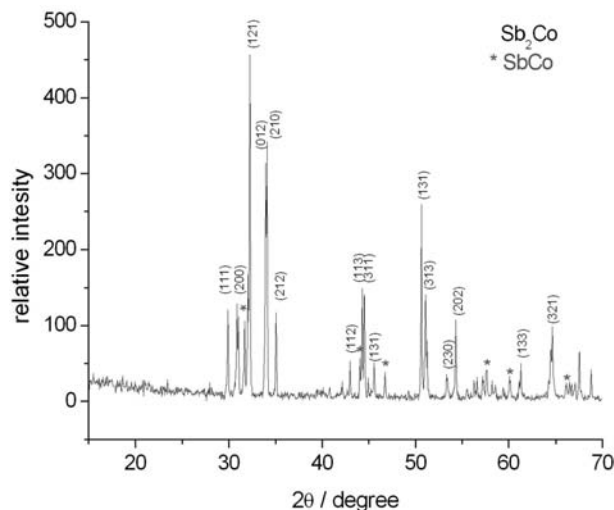


Fig 3. X-Ray diffractogram of the alloy obtained by the chemical reduction of the product of the gel-combustion procedure. The diffraction lines of  $\text{Sb}_2\text{Co}$  are labeled by Miller indices, while those of  $\text{SbCo}$  are labeled by an asterisk.

To avoid these obstacles, an attempt was made to simplify the phase composition of the oxides by an additional thermal treatment. Therefore, the oxide product obtained upon gel-combustion was treated isothermally at a temperature of 1000 °C in an air stream for 30 min, under the expectation that the simple oxides  $\text{CoO}$  and  $\text{Sb}_2\text{O}_3$ , appearing together with  $\text{CoSb}_2\text{O}_6$ , would mutually react *via* a solid-state reaction to yield pure  $\text{CoSb}_2\text{O}_6$ . After this treatment, the oxide product was examined by X-ray diffraction and the diffractogram, shown in Fig. 4, indeed evidenced only one phase,  $\text{CoSb}_2\text{O}_6$ .

The monophase powder  $\text{CoSb}_2\text{O}_6$  was then subjected to reduction. A thermogravimetric curve of the reduction of a small sample of the same oxide, presented in Fig. 5, shows a mass loss of 24 %, which is in accordance with the calculated value for complete reduction of  $\text{CoSb}_2\text{O}_6$  to metal. Generally, there is no remarkable difference in the shape between this TG curve of the monophase oxide and the one presented in Fig. 2 for the multiphase oxide mixture. Therefore, the oxide  $\text{CoSb}_2\text{O}_6$  was reduced in the same way on heating in an  $\text{Ar} + \text{H}_2$  (25 %) stream at 800 °C for 30 min. After cooling to room temperature, the mass was examined by X-ray diffraction and SEM. The X-ray diffractogram presented in Fig. 6 indicates the presence of  $\text{Sb}_2\text{Co}$  only, although the relatively low signal-to-noise ratio indicates its low crystallinity degree. Its SEM microphotograph, Fig. 7, shows that the particle diameter amounted to a few micrometers and that the relatively high temperature of 800 °C, required for oxide reduction, caused partial particle agglomeration by sintering.

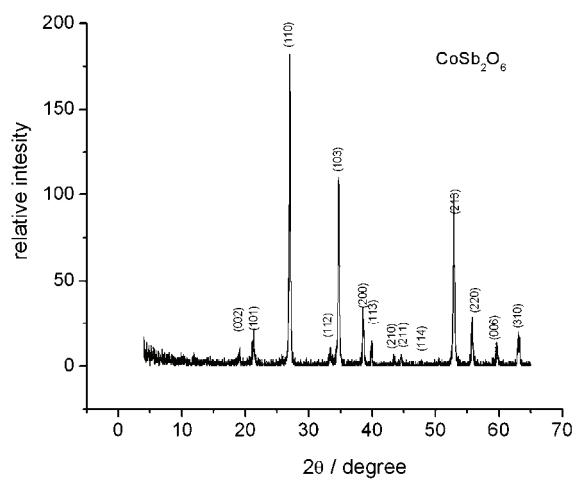


Fig 4. X-Ray diffractogram of the product of gel-combustion after thermal treatment at 1000 °C. Only the reflections of  $\text{CoSb}_2\text{O}_6$ , labeled by Miller indices, may be observed.

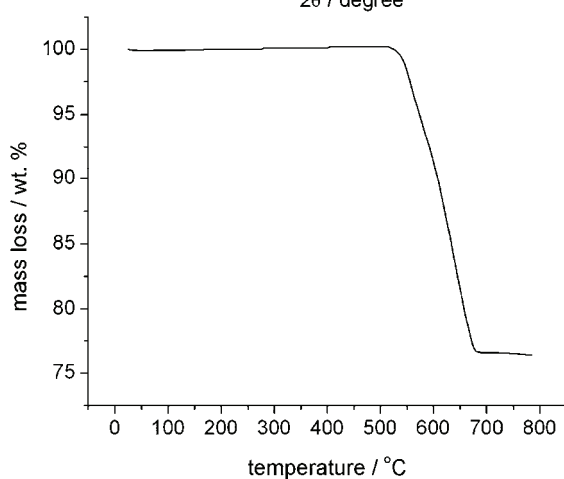


Fig 5. Thermogravimetric curve obtained during the heating of the stoichiometric oxide  $\text{CoSb}_2\text{O}_6$  in an  $\text{Ar} + \text{H}_2$  (25 vol.%) stream at a heating rate of  $15\text{ °C min}^{-1}$ .

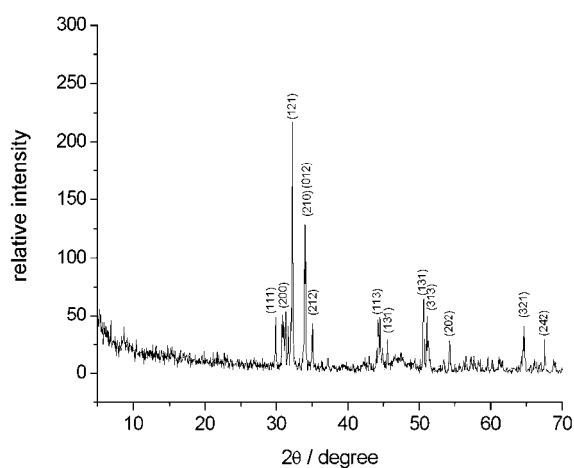


Fig 6. X-Ray diffractogram of the product of the reduction of  $\text{CoSb}_2\text{O}_6$ . The reflections from the different crystallographic planes of  $\text{Sb}_2\text{Co}$  are labeled by the corresponding Miller indices.



Fig. 7. An SEM microphotograph of the  $\text{Sb}_2\text{Co}$  alloy.

#### CONCLUSIONS

The intention of this study was first to synthesize an intimate mixture of  $\text{CoO}$  and  $\text{Sb}_2\text{O}_5$ , expecting to obtain  $\text{CoSb}_2\text{O}_6$ , and then to reduce it to the intermetallic compound  $\text{Sb}_2\text{Co}$  in powdery form. The gel-combustion procedure was used for the synthesis of the oxide mixture. The conditions of oxide reduction were controlled thermogravimetrically, while the phase composition of solid products was controlled by X-ray diffraction. For the gel-combustion product, purified from carbon residues by heating in air at  $700\text{ }^\circ\text{C}$ , X-ray diffractometry evidenced a multiphase system, consisting of the mixture  $\text{CoSb}_2\text{O}_6 + \text{CoO} + \text{Sb}_2\text{O}_3$ . Its reduction in a hydrogen atmosphere at  $800\text{ }^\circ\text{C}$  yielded a two-phase metallic product composed of  $\text{SbCo}$  and  $\text{Sb}_2\text{Co}$ . In order to improve the procedure, the oxide mixture obtained by the gel-combustion procedure was additionally treated by annealing at  $1000\text{ }^\circ\text{C}$ . This treatment provided the monophase oxide  $\text{CoSb}_2\text{O}_6$ . Its reduction in a hydrogen atmosphere at  $800\text{ }^\circ\text{C}$  yielded the monophase alloy  $\text{Sb}_2\text{Co}$ . This method requires a reduced number of time consuming steps in comparison to the solvothermal method.

*Acknowledgement.* The study is a part of the project No. 142047, granted by the Ministry of Science and Technological Development of the Republic of Serbia. Varta Microbattery GmbH supported the study through an agreement with the Faculty of Physical Chemistry, No. 297-14.4.2006.

#### ИЗВОД

#### СИНТЕЗА $\text{CoSb}_2\text{O}_6$ МЕТОДОМ САГОРЕВАЊА ГЕЛА И РЕДУКЦИЈА ДО ПРАШКАСТЕ ЛЕГУРЕ $\text{Sb}_2\text{Co}$

МАЈА ЈОВИЋ<sup>1</sup>, МАРИНА ДАШИЋ<sup>1</sup>, KONRAD HOLL<sup>2</sup>, ДЕЈАН ИЛИЋ<sup>2</sup> и СЛАВКО МЕНТУС<sup>1</sup>

<sup>1</sup>Универзитет у Београду, Факултет за физичку хемију, Студенски тирг 1, 11000 Београд и

<sup>2</sup>Varta Microbattery GMBH- Daimlerstrase 1, 73479 Ellwangen, Germany

Легура  $\text{Sb}_2\text{Co}$  у форми праха синтетисана је редукијом оксида  $\text{CoSb}_2\text{O}_6$  добијеног методом сагоревања цитратног гела. Полазни водени раствор направљен је од антимоно-нитрата, кобалт-нитрата и лимунске киселине. Полазни раствор са молским односом  $\text{Co(II)/Sb(V)}$

1:2 преведен је у гел упаравањем воде. Гел је загреван на ваздуху до температуре самопаљења. Производ сагоревања је смеша оксида, и морао је да се додатно третира термички да би се превео у чист  $\text{CoSb}_2\text{O}_6$ . Редукијом  $\text{CoSb}_2\text{O}_6$  у атмосфери водоника добијена је прашкаста легура  $\text{Sb}_2\text{Co}$  као чиста фаза. Процес редукије оксида до легура контролисан је термогравиметријски, док је фазни састав оксида и легура испитиван дифракцијом X-зрака.

(Примљено 7. маја, ревидирано 20. јуна 2008)

#### REFERENCES

1. L. R. Pederson, G. D. Maupin, W. J. Weber, D. J. McReady, R. W. Stephens, *Mat. Lett.* **10** (1991) 437
2. J. Huang, H. Zhuang, W.-L. Li, *Mat. Res. Bull.* **38** (2003) 149
3. X.-H. Wang, L. L. Z. Gui, S. Shu, J. Zhou, *Mat. Chem. Phys.* **77** (2002) 248
4. D. Jugović, N. Cvjetičanin, V. Kusigerski, S. Mentus, *J. Optoelectron. Adva. Mater.* **5** (2003) 343
5. Z. Jiao, M. Wu, Z. Qin, H. Xu, *Nanotechnology* **14** (2003) 458
6. Y. Yoshimura, T. Sato, H. Shimada, N. Matsubayashi, M. Imamura, A. Nishijima, M. Higo, S. Yoshitomi, *Catal. Today* **29** (1996) 221
7. H. Okamoto, A. Ishikawa, *Appl. Phys. Lett.* **55** (1989) 19239
8. H.-J. Kim, J.-H. Lee, I.-H. Sohn, T.-J. Hwang K.-Y. Lee, *Korea-Australia Rheol. J.* **14** (2002) 71
9. A. F. Benton, P. H. Emmett, *J. Am. Chem. Soc.* **46** (1924) 2728
10. J. A. Rodriguez, J. C. Hanson, A. I. Frenkel, J. Y. Kim, M. Perez, *J. Am. Chem. Soc.* **124** (2002) 346
11. J. T. Richardson, R. Scates, M. V. Twigg, *Appl. Phys. A* **246** (2003) 137
12. B. Janković, B. Adnadjević, S. Mentus, *Thermochim. Acta* **456** (2007) 48
13. I. K. Konstanchuk, E. Yu. Ivanov, V. V. Boldyrev, *Mat. Res. Bull.* **19** (1984) 769
14. T. Ressler, J. Wienold, R. E. Jentoft, *Solid State Ionics* **141–142** (2001) 243
15. R. Morales, *Scan. J. Metallurgy* **32** (2003) 263
16. S. Mentus, D. Majstorović, B. Tomić, R. Dimitrijević, *Mat. Sci. Forum* **494** (2005) 345
17. S. Mentus, B. Tomić-Tucaković, D. Majstorović, R. Dimitrijević, *Mater. Chem. Phys.* **112** (2008) 254
18. T. Caillat, *J. Phys. Chem. Solids* **59** (1995) 61
19. K. Liu, Z. Jiuxing, X. Dong, *J. Mater. Process. Technol.* **184** (2007) 257
20. P. Feschotte, D. Lorin, *J. Less-Common Metals* **155** (1989) 255
21. A. Aboulaich, M. Mouyane, F. Robert, P.-E. Lippens, J. Olivier-Fourcade, P. Willmann, J.-C. Jumas, in *Proceedings of International Meeting on Lithium Batteries*, Biarritz, France, (2006), Meeting Abstracts, (2006), Abstract No. 285
22. J. Xie, X. B. Zhao, G. S. Cao, Y. D. Zhong, M. J. Zhao, J. P. Tu, *Electrochim. Acta* **50** (2005) 1903
23. J. Xie, G. S. Cao, X. B. Zhao, Y. D. Zhong, M. J. Zhao, *J. Electrochem. Soc.* **151** (2004) A1905
24. P.-E. Lippens, J. Olivier-Fourcade, J.-C. Jumas, in *Proceedings of International Meeting on Lithium Batteries*, Biarritz, France, (2006), Meeting Abstracts, (2006), Abstract No. 232
25. V. Chevrier, J. R. Dahn, in *Proceedings of International Meeting on Lithium Batteries*, Biarritz, France, (2006), Meeting Abstracts, (2006), Abstract No. 277
26. *Powder Diffraction Files*, Joint Committee on Powder Diffraction Standards, International Center for Diffraction Data, Swarthmore, PA, 1987.



www.shd.org.rs

*J. Serb. Chem. Soc.* 74 (1) 61–69 (2009)  
JSCS–3809

Journal of  
the Serbian  
Chemical Society

JSCS@tmf.bg.ac.yu • www.shd.org.rs/JSCS

UDC 546.74–36:669.018:548.2+551.312.1

Original scientific paper

## Primary and secondary dendrite spacing of Ni-based superalloy single crystals

SLOBODANKA KOSTIĆ<sup>1</sup>, ALEKSANDAR GOLUBOVIĆ<sup>1\*#</sup> and ANDREJA VALČIĆ<sup>2</sup>

<sup>1</sup>*Institute of Physics, Pregrevica 118, P.O. Box 68, 11080 Zemun and* <sup>2</sup>*Faculty of Technology and Metallurgy, Karnegieva 4, 11000 Belgrade, Serbia*

(Received 5 May, revised 11 July 2008)

**Abstract:** Ni-based superalloy single crystals were grown by different methods (gradient method and Bridgman technique with spontaneous nucleation and with seed). In all crystal growth experiments using the Bridgman technique, the temperature gradient along the vertical furnace axes was constant ( $G = 33.5$  °C/cm). The obtained single crystals were cut, mechanical and chemical polished, and chemically etched. Using a metallographic microscope, the spacing of the primary and secondary dendrites was investigated. The dendrite arm spacing (DAS) was determined using a Quantimet 500 MC. The obtained results are discussed and compared with published data.

**Keywords:** superalloy; crystal growth; single crystal; dendrites; quantimeter.

### INTRODUCTION

Ni-based, single crystal alloys have applications in advanced gas turbines and jet engines, due to their improved mechanical properties, creep resistance, thermal fatigue resistance and high melting point as compared to the conventionally prepared Ni-based superalloys. The use of these expensive materials as gas turbine components requires stability of the microstructure as well as of the chemical composition. During fabrication and repair of the components, microstructural changes may occur, which can affect the mechanical properties. The main crystallization parameters having a considerable influence on the microstructure and physical properties of the material are the temperature gradient ( $G$ ), the crystal growth rate ( $R$ ), and the concentration of the alloying elements ( $c_0$ ).<sup>1</sup>

Ni-based superalloys are biphasic compounds, consisting of a face-centered cubic  $\gamma$  matrix and  $\gamma'$  precipitates. Dendrites are the most common growth morphology during the solidification of metals, alloys and other substances.<sup>2</sup> Ni-based superalloys single crystals also have a dendritic structure. Due to the need

\* Corresponding author. E-mail: golubovic@phy.bg.ac.rs

# Serbian Chemical Society member.

doi: 10.2298/JSC0901061K

to predict and control the microstructure of cast alloys, dendritic growth has been extensively studied. Since metallic alloys are opaque and have a high melting point, which impedes precise control of the solidification condition, direct observation of growing dendrites in transparent analogues has become a powerful tool for investigating microstructure formation under controlled conditions.<sup>3</sup>

A number of studies have indicated the effect of microstructure and, particularly, of dendrite spacing upon mechanical properties.<sup>4</sup> Dendritic structures can be more important in the prediction of mechanical properties than grain size. The improved mechanical characteristics of cast structures having smaller dendrite spacings are largely due to the shorter wavelength of the periodicity of the microsegregation. Much of the initial research devoted to dendritic coarsening was focused on the measurement of the secondary dendritic arm spacing,  $\lambda_2$ , and the proposal of a mechanism aimed at describing the evolution of this secondary arm spacing.<sup>5</sup> The aim of this study was to investigate the properties of the primary and secondary dendrites of Ni-based superalloy single crystals in order to improve the application of the superalloy.

#### EXPERIMENTAL

The composition of the superalloy 444 (Ed Fagan Inc., USA) was (in mass %): 8.6 % Cr, 1.98 % Ti, 5.1 % Al, 11.1 % W, 0.91 % Nb and 72.31 % Ni.

Single crystals of the Ni-based superalloy were grown by the Bridgman (spontaneous nucleation or from a polycrystalline seed) technique<sup>6,7</sup> and the gradient method.<sup>6</sup>

The temperature gradient along the vertical furnace axes for the Bridgman technique was constant ( $G = 33.5$  °C/cm).

All the samples were longitudinally cut, then mechanically and chemically polished, and finally selectively etched.<sup>7</sup>

All photographs were obtained using a metallographic microscope (PM10-35ACS, Olympus, Japan). The magnifications were 20.

Using an automatic device for quantitative picture analysis, Quantimet 500 MC (Leica Cambridge Ltd., Cambridge, UK), and the linear measuring method applied to the samples of superalloy, the dendrite arm spacing (*DAS*) were determined.

#### RESULTS AND DISCUSSION

The process of single crystal growth by the gradient method was performed in the standard way.<sup>6</sup> The seed used to commence the crystallization was a fine-grained material of the same alloy. The experiments were performed at different cooling rates ( $V$ ), which remained almost constant during the experiment. The best result was obtained with a cooling rate of 3.4 mm/min. Polycrystalline structure was approximately 10 mm from the top of the seed, and after that it was a single crystal to almost the end of the sample. Although the temperature gradient along the vertical furnace axes was not constant, the growing rate increased during the experiment by a factor of approximately 10.

The crystal growth by the Bridgman technique was performed in two different ways: a) the growth commenced from a completely molten alloy (spontaneous nucleation) or from a polycrystalline seed, formed by a relatively slow nucleation and b) the growth started from a polycrystalline seed, which had a more coarse structure than the seed used in the gradient method.

The temperature gradient along the vertical furnace axes was fixed and the same for both types of Bridgman techniques ( $G = 33.5 \text{ }^\circ\text{C/cm}$ ). The crystal growth rate was changed from 1 mm/min to 11 mm/min in order to obtain the best value. It was found in the literature that other authors<sup>4</sup> worked in a similar way, but fixed the crystal growth rate while changing the temperature gradient. In addition, these authors had a transparent material, while in this study a real alloy was employed.

A microphotograph of the sample grown by the Bridgman technique with spontaneous nucleation, with the crystal growth rate of 2 mm/min, is shown in Fig. 1. Samples grown by Bridgman technique with seed were grown with uniform rate or with different rates (the rate was changed in the process of crystal growth), in order to investigate the properties of dendrite spacing. The microphotographs of the same crystal grown by the Bridgman technique with seed at growth rates of 6 mm/min and 2 mm/min are shown in Figs. 2 and 3, respectively.



Fig. 1. Photograph showing the primary dendrite spacing in a Ni-based superalloy single crystal obtained by the Bridgman technique with spontaneous nucleation. The crystal growth rate was 2 mm/min and the length of the single crystal was 11.5 cm. The photograph was taken at 12–15 mm from the beginning of the crystal with a magnification of  $\times 24$ .



Fig. 2. Photograph showing the primary dendrite spacing in a Ni-based superalloy single crystal obtained by the Bridgman technique with seed. The crystal growth rate was 6 mm/min and the length of the single crystal was 6.36 cm. The photograph was taken at 2 cm from the seed with a magnification of  $\times 24$ .

It is clear that all the samples were single crystals and the various crystal growth methods can serve as a tool for a better understanding of the processes into non-transparent materials. For Ni-based superalloys, a single crystal with a dendritic structure is the common type of structure, as the process of thermal homogenization always follows the process of crystal growth.<sup>8</sup> Crystal growth

was in the [001] direction of the all samples, which is in accordance with literature data.<sup>3</sup>

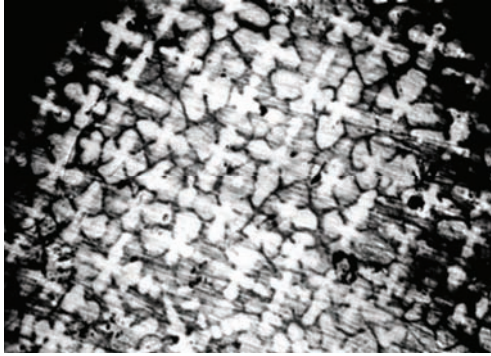


Fig. 3. Photograph showing the primary dendrite spacing in a Ni-based superalloy single crystal obtained by the Bridgman technique with seed. The crystal growth rate was 2 mm/min and the length of the single crystal was 3.5 cm. The photograph was taken at 1 cm from the end with a magnification of  $\times 24$ .

The morphology of the solidification interface has been a very important subject for investigation by many scientists. The primary spacing  $\lambda_1$  is one of the parameters which can correlate the growth conditions with the resulting microstructures. Most of the theoretical studies reach the analogical result, which gives:<sup>9</sup>

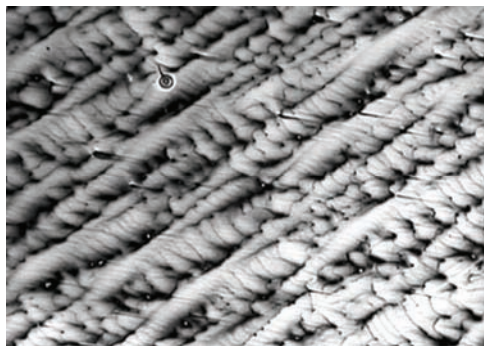
$$\lambda_1 = AG^{-m}R^{-n} \quad (1)$$

where  $G$  is the temperature gradient and  $R$  the crystal growth rate.  $A$  is a parameter that depends on the alloy composition, while  $m$  and  $n$  are 0.5 and 0.25, respectively. An analysis of the primary dendrite spacing ( $\lambda_1$ ) allows a better understanding of the mechanism of crystal growth. For the Bridgman technique, for a given growth condition, the velocity of 2 mm/min is the velocity of spontaneous nucleation. On doubling the crystal growth rate from 2 to 4 mm/min, the primary dendrite spacing remains the same value (295  $\mu$ ), although the velocity has a higher value. This result is in accordance with the result from the literature.<sup>3</sup> On further increasing the growth rate, almost the same result was obtained, although the authors stated that some larger dendrites of the array became unstable and the tertiary arms of these dendrites grew to form new primary dendrites, thereby decreasing the average primary spacing. It is supposed that this phenomenon cannot be observed as the present system was more complicated and many motions in the system were smothered. In addition, the Bridgman method with spontaneous nucleation additionally smothers the system.

Applying the Bridgman technique with seed, the effect of an increasing change of the average primary spacing was observed when the crystal growth rate of the same crystal was changed from 11 to 2 mm/min. The differences from 125 to 288  $\mu$  can be explained if the dendrites, after an unstable period, form a stable dendrite configuration. An attempt was made to decrease the primary dendrite spacing by employing a crystal growth rate to 1 mm/min, no interesting differences could be observed and the value of  $\lambda_1$  given above is the lower limit,

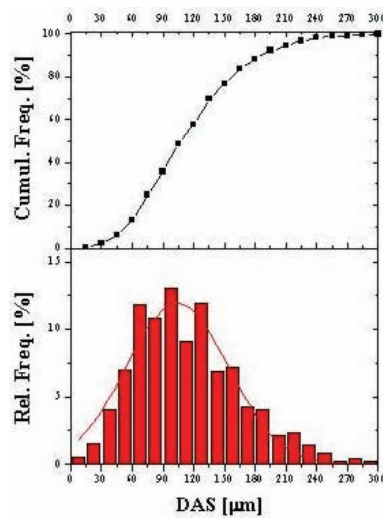
$\lambda_{1,min}$ . The same sample grown at 6 and 2 mm/min is shown in Figs. 2 and 3, respectively. No significant differences in the primary dendrite spacing could be observed, probably due to the properties of the system (more complicated than that used in the literature).<sup>3</sup>

An automatic device for quantitative picture analysis, Quantimet 500 MC, and the linear measuring method were applied to the samples of the superalloy, whereby the dendrite arm spacing (*DAS*) and the distribution of *DAS* values (histograms) were obtained. The obtained results are shown in Figs. 4–8.

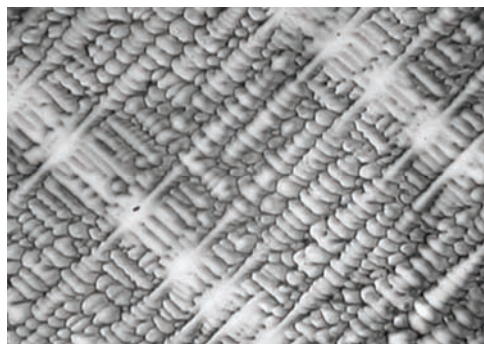


(a)

Fig. 4. a) Photograph showing the secondary dendrite spacing in a Ni-based superalloy single crystal obtained by the Bridgman technique with spontaneous nucleation and b) the histogram of the distribution of the secondary dendrite spacings. The crystal growth rate was 2 mm/min and the magnification  $\times 20$ .

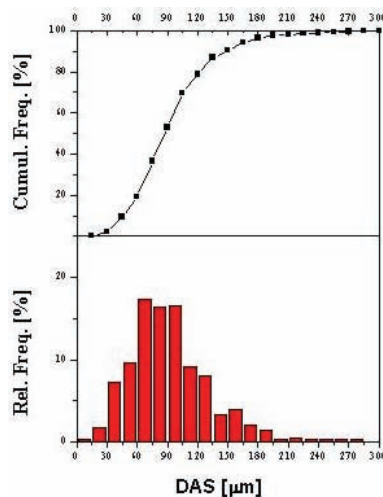


(b)

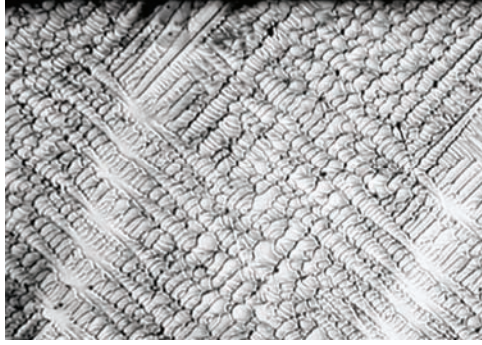


(a)

Fig. 5. a) Photograph showing the secondary dendrite spacing in a Ni-based superalloy single crystal obtained by the gradient method and b) the histogram of the distribution of the secondary dendrite spacing. The crystal growth rate was 3.4 mm/min and the magnification  $\times 20$ .

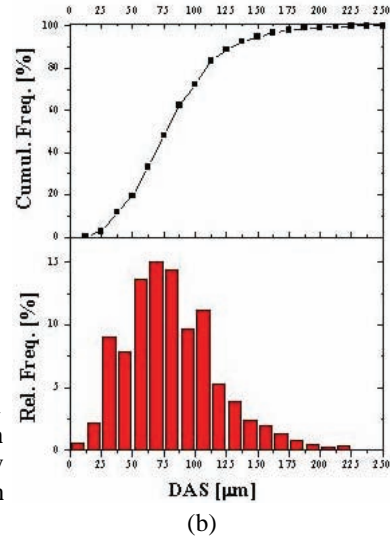


(b)



(a)

Fig. 6. a) Photograph, showing the secondary dendrite spacing in a Ni-based superalloy single crystal obtained by the Bridgman technique with spontaneous nucleation and b) the histogram of the distribution of the secondary dendrite spacing. The crystal growth rate was 4 mm/min and the magnification  $\times 20$ .

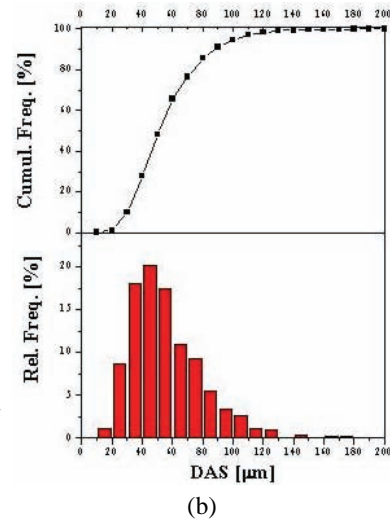


(b)



(a)

Fig. 7. a) Photograph showing the secondary dendrite spacing in a Ni-based superalloy single crystal obtained by the Bridgman technique with seed and b) the histogram of the distribution of the secondary dendrite spacing. The crystal growth rate was 6 mm/min and the magnification  $\times 20$ .



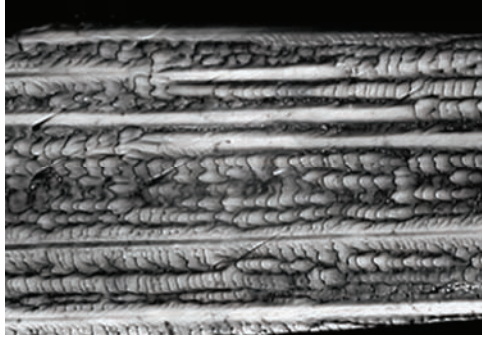
(b)

In accordance to Fleming's investigation,<sup>2</sup> the secondary dendrite spacing is a function of the temperature gradient and the crystal growth rate. This type of Relation can be express as:

$$\lambda_2 = C(GR)^{-n} \quad (2)$$

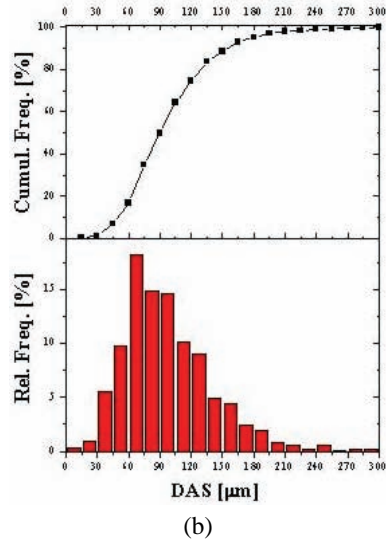
where  $\lambda_2$  is the secondary dendrite spacing,  $C$  a constant,  $G$  the temperature gradient,  $R$  the crystal growth rate and  $n = 1/3$ .

The results obtained from the Quantimet 500 MC measurements are summarized in Table I and Fig. 9 represents the linear fit for the Relation (2).



(a)

Fig. 8. a) Photograph showing the secondary dendrite spacing in Ni-based superalloy single crystal obtained by the Bridgman technique with spontaneous nucleation and b) the histogram of the distribution of the secondary dendrite spacing. The crystal growth rate was 11 mm/min and the magnification  $\times 20$ .



(b)

TABLE I. Secondary dendrite spacing values of Ni-based superalloy single crystals obtained from Quantimet 500 MC measurements

Growth method	Crystal growth rate, mm/min	Minimum distance, mm	Maximum distance, mm	Average distance, mm	Distinction %
Bridgman spont. nucleation	2	0.003	0.314	0.114	1.351
Gradient method	3.4	0.006	0.291	0.084	1.810
Bridgman spont. nucleation	4	0.018	0.328	0.064	2.036
Bridgman, with seed	6	0.014	0.178	0.075	1.662
Bridgman spont. nucleation	11	0.016	0.238	0.063	1.996

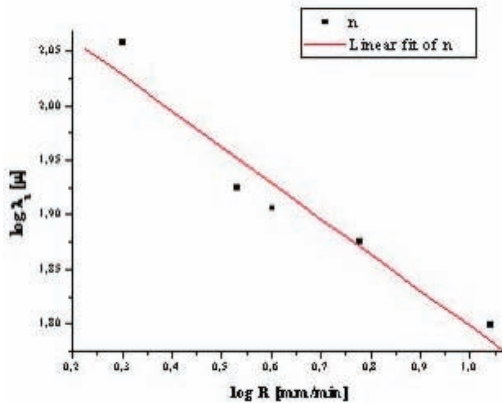


Fig. 9. Linear fit of  $n$  for the Relation  $\lambda_2 = C(GR)^{-n}$ .

It is clearly seen from Fig. 9 that  $n$  is very close to  $1/3$ , which is in accordance to Fleming's investigation<sup>2</sup> that the secondary dendrite spacing is function of the temperature gradient and the crystal growth rate. In the present experiments, the temperature gradient was fixed for both Bridgman techniques but the crystal growth rate was changed.

#### CONCLUSIONS

1. Single crystals of Ni-based superalloys were grown by the gradient method and by the Bridgman technique (spontaneous nucleation or from a polycrystalline seed). Comparing the applied techniques, the largest single crystal part of a sample superalloy was obtained by the Bridgman technique with spontaneous nucleation.

2. For the given growth conditions for the Bridgman technique, 2 mm/min is the velocity of spontaneous nucleation.

3. The primary dendrite spacing remained constant (295  $\mu$ ), although the velocity changed from 2 mm/min to 4 mm/min, which is in accordance with published data.<sup>5</sup>

4. The results for the secondary dendrite spacing, obtained by Quantimet 500 MC measurements, confirmed the presumption that the secondary dendrite spacing is a function of the temperature gradient and the crystal growth rate.

*Acknowledgements.* We are grateful to Dr. B. Jordović, Technical Faculty, Čačak, for measurements at Quantimet 500 MC. This work is supported by the Ministry of Science and Technological Development of the Republic of Serbia under Project 141028.

#### ИЗВОД

#### ПРОСТИРАЊЕ ПРИМАРНИХ И СЕКУНДАРНИХ ДЕНДРИТА МОНОКРИСТАЛА СУПЕРЛЕГУРЕ НА БАЗИ НИКЛА

СЛОБОДАНКА КОСТИЋ<sup>1</sup>, АЛЕКСАНДАР ГОЛУБОВИЋ<sup>1</sup> и АНДРЕЈА ВАЛЧИЋ<sup>2</sup>

<sup>1</sup>Институт за физику, Предревца 118, б.бр. 68, 11080 Земун и <sup>2</sup>Технолошко-металуришки факултет,  
Карнегијева 4, 11000 Београд

Монокристали суперлегури на бази никла су расли помоћу различитих метода (градијентна метода и техника по Брицману са спонтаном нуклеацијом и са клицом). У свим експериментима раста кристала по техници Брицмана температурни градијент дуж вертикалне осе пећи је био константан ( $G = 33,5$  °C/cm). Добијени монокристали су сечени, механички и хемијски полирани, и хемијски нагрисани. Примарни и секундарни дендрити су испитивани коришћењем металографског микроскопа. Простирања крака дендрита ( $DAS$ ) су одређивана коришћењем квантометра Quantimet 500 MC. Добијени резултати су дискутовани и упоређени са подацима из литературе.

(Примљено 5. маја, ревидирано 11. јула 2008)

## REFERENCES

1. M. Ahmad, J. I. Akhter, M. A. Shaikh, *J. Alloy. Compd.* **422** (2006) 97
2. M. S. Flemings, *Solidification Processing*, McGraw-Hill, New York, 1974
3. D. Ma, *J. Cryst. Growth* **260** (2004) 580
4. X. Lin, W. Huang, T. Li, Y. Zhou, *Acta Mater.* **47** (1999) 3271
5. D. Kammer, P. W. Voorhees, *Acta Mater.* **54** (2006) 1549
6. A. Valčić, S. Nikolić, T. Valčić, *J. Serb. Chem. Soc.* **58** (1993) 439
7. S. Nikolić, A. Valčić, V. Radojević, *Mat. Sci. Forum* **282–283** (1998) 331
8. A. Valčić, S. Nikolić, *Mater. Sci. Forum* **214** (1995) 265
9. H. A. Palacio, M. Solari, H. Biloni, *J. Cryst. Growth* **73** (1985) 369.





www.shd.org.rs

*J. Serb. Chem. Soc.* 74 (1) 71–84 (2009)  
JSCS–3810

JSCS@tmf.bg.ac.yu • www.shd.org.rs/JSCS

UDC 537.622.4.004.12:546.47–31+546.711–31

Original scientific paper

## Ferromagnetic behaviour of the Zn–Mn–O system

BRANKA BABIĆ-STOJIĆ\*, DUŠAN MILIVOJEVIĆ and JOVAN BLANUŠA

*Vinča Institute of Nuclear Sciences, P.O. Box 522, 11001 Belgrade, Serbia*

(Received 26 May, revised 16 July 2008)

**Abstract:** Polycrystalline Zn–Mn–O samples with nominal manganese concentrations  $x = 0.01, 0.04$  and  $0.10$  were synthesized by a solid state reaction route using  $(\text{ZnC}_2\text{O}_4 \cdot 2\text{H}_2\text{O})_{1-x}$  and  $(\text{MnC}_2\text{O}_4 \cdot 2\text{H}_2\text{O})_x$ . Thermal treatment of the samples was performed in air at temperatures 673, 773, 873, 973 and 1173 K for  $x = 0.01$  and at the temperature 773 K for  $x = 0.04$  and  $0.10$ . The samples were investigated by X-ray diffraction, thermogravimetry, differential thermal analysis, transmission electron microscopy, magnetization measurements and electron paramagnetic resonance. X-Ray diffraction was also performed on  $\text{MnO}_2$  thermally treated at temperatures 673, 773, 873, 973, 1073 and 1173 K. Room temperature ferromagnetism was observed in the Zn–Mn–O samples with  $x = 0.01$  thermally treated at low temperatures (673 and 773 K) and in the sample with  $x = 0.04$  thermally treated at 773 K. It seems that the ferromagnetic phase could originate from interactions between  $\text{Mn}^{2+}$  and acceptor defects incorporated in the ZnO crystal lattice during the thermal treatment of the samples.

**Keywords:** ZnO; diluted magnetic semiconductors; room temperature ferromagnetism.

### INTRODUCTION

Semiconductor materials that exhibit ferromagnetism above room temperature (RT) have attracted considerable interest in the past few years. These materials are essential components for the development of spintronic devices. Dietl *et al.*<sup>1</sup> predicted the existence of ferromagnetism with a Curie temperature,  $T_C$ , above RT in *p*-type ZnO and GaN doped with Mn. A ferromagnetic phase in undoped carrier and in *n*-type ZnO substituted with Fe, Co and Ni was also predicted.<sup>2,3</sup> Since then, transition metal doped II–VI and III–V semiconductors have been intensively investigated. Among these materials, Mn-doped ZnO is particularly interesting because of its unusual magnetic properties and disagreement about both the existence and the origin of RT ferromagnetism. The first observation of RT ferromagnetism in low-temperature processed bulk and thin

\* Corresponding author. E-mail: [babic@vin.bg.ac.yu](mailto:babic@vin.bg.ac.yu)  
doi: 10.2298/JSC0901071B

film samples of Mn-doped ZnO was reported by Sharma *et al.*<sup>4</sup> In this study, the authors found that their results were in agreement with a model of carrier induced ferromagnetic ordering between Mn ions in ZnO. The theoretical prediction that *p*-type defects in Mn-substituted ZnO can produce high  $T_C$  ferromagnetism was confirmed experimentally by doping  $Mn^{2+}$ :ZnO with nitrogen.<sup>5</sup> It was also shown that *n*-type defects in  $Mn^{2+}$ :ZnO introduced by Zn vapour diffusion<sup>5</sup> or by hydrogen annealing<sup>6</sup> did not stabilize long range Mn–Mn ferromagnetic coupling. Contrary to these reports, several authors suggested that the high-temperature ferromagnetism in low-temperature processed Mn–Zn–O samples originated from an oxygen-vacancy-stabilized metastable phase,  $Mn_{2-x}Zn_xO_{3-\delta}$ .<sup>7,8</sup> In addition, some recent studies showed the absence of ferromagnetic ordering in bulk single phase  $Zn_{1-x}Mn_xO$  materials down to 2 K.<sup>9–11</sup> Controversial results have also been obtained for  $Zn_{1-x}Mn_xO$  thin film samples, which extend from paramagnetic,<sup>12</sup> to spin-glass behaviour,<sup>13</sup> and to low-temperature ferromagnetism.<sup>14</sup> Various properties obtained for the Zn–Mn–O system by different methods suggest a strong dependence of the magnetic properties of these materials on the synthesis conditions. In the present work, we have studied the structural and magnetic properties of Zn–Mn–O samples prepared by thermal treatment in air at various temperatures were studied in order to obtain a better insight into the processes responsible for the observed high-temperature ferromagnetism in this material.

#### EXPERIMENTAL

Polycrystalline samples of Zn–Mn–O were prepared by a solid-state reaction method using zinc oxalate dihydrate ( $ZnC_2O_4 \cdot 2H_2O$ , 99.999 %, Alfa Aesar) and manganese oxalate dihydrate ( $MnC_2O_4 \cdot 2H_2O$ , 99 %, Alfa Aesar) as starting materials. Appropriate amounts of  $(ZnC_2O_4 \cdot 2H_2O)_{1-x}$  and  $(MnC_2O_4 \cdot 2H_2O)_x$  were mixed, pressed into pellets and calcined at 673 K for 5 h in air. The calcined samples were reground, pelletized and thermally treated at 673, 773, 873, 973 and 1173 K for 12 h in air to obtain Zn–Mn–O samples with a nominal manganese concentration  $x = 0.01$ . Thermal treatment of the samples with the nominal manganese concentration  $x = 0.04$  and 0.10, was carried out at 773 K. The samples of manganese dioxide ( $MnO_2$ , 99.999 %, Sigma Aldrich) were thermally treated at 673, 773, 873, 973, 1073 and 1173 K for 12 h in air.

Powder X-ray diffraction (XRD) patterns were recorded on a Philips PW 1050 diffractometer using  $CuK_\alpha$  radiation. The XRD patterns were measured with a step size ( $2\theta$ ) of  $0.02^\circ$  at a slow scan rate of 60 s per step. Thermogravimetry (TG) and differential thermal analysis (DTA) were performed by heating up to 1273 K in a static air atmosphere at a heating rate  $10^\circ \text{min}^{-1}$  using a model STA-1000 instrument (Stanton-Redcroft) which enables the simultaneous recording of TG and DTA signals. Transmission electron microscopy (TEM) measurements of Zn–Mn–O samples were performed using a Philips EM 400 instrument with an operating voltage 120 kV. The samples were prepared by placing a drop of an aqueous Zn–Mn–O solution onto a carbon-coated copper grid. After drying, the samples were examined by TEM. The magnetization measurements performed using a SQUID magnetometer (MPMS XL-5, Quantum Design). Electron paramagnetic resonance (EPR) experiments were performed on a Varian E-line spectrometer operating at a nominal frequency of 9.5 GHz.

## RESULTS AND DISCUSSION

The XRD patterns of Zn–Mn–O samples with a nominal manganese concentration  $x = 0.01$  thermally treated at 673, 773, 873, 973 and 1173 K in air are presented in Fig. 1. The diffraction lines can be indexed based on a mixture of phases, the major phase ZnO and the minor phases  $\text{MnO}_2$ ,  $\text{Mn}_2\text{O}_3$ ,  $\text{Mn}_3\text{O}_4$  and an impurity phase  $\text{Zn}_{1-y}\text{Mn}_y\text{Mn}_2\text{O}_4$  with tetragonal symmetry (space group  $I4_1/amd$ ). The vertical ticks and indices indicate the peak positions for the wurtzite crystal structure of ZnO (space group  $P6_3mc$ ). The XRD patterns show the evolution of minority manganese oxides phases with increasing temperature of thermal treatment. The XRD pattern of the sample thermally treated at 673 K shows, in addition to the ZnO phase, the presence of  $\text{MnO}_2$  and the onset of the  $\text{Mn}_2\text{O}_3$  phase in the form of a shoulder on the high-angle side of the ZnO (100) peak. In the  $x = 0.01$  sample sintered at 773 K, the  $\text{Mn}_2\text{O}_3$  phase progressively develops, existing together with  $\text{MnO}_2$ . With increasing sintering temperature (973 K), the  $\text{Mn}_2\text{O}_3$  phase did not exhibit a further increase, whereas the impurity phase  $\text{Zn}_{1-y}\text{Mn}_y\text{Mn}_2\text{O}_4$  continued to grow. For a sintering temperature 1173 K, a peak corresponding to the  $\text{Mn}_3\text{O}_4$  phase appears.

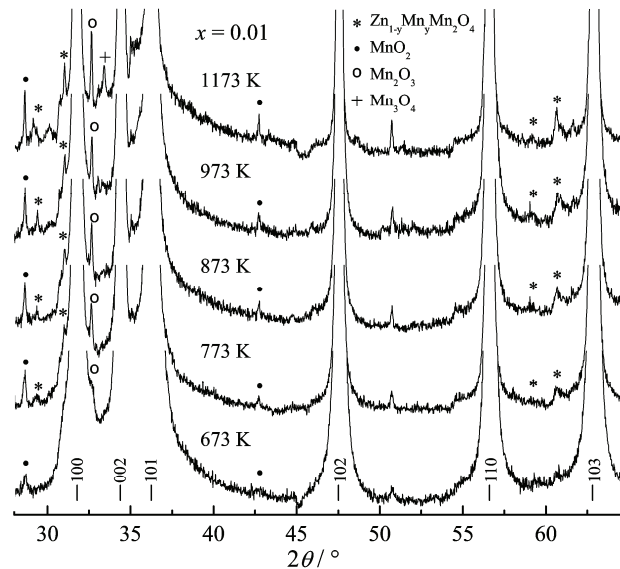


Fig. 1. X-Ray diffraction patterns at 300 K for the Zn–Mn–O samples with  $x = 0.01$ , thermally treated at temperatures 673–1173 K recorded at a slow scan rate. The peak positions for the wurtzite ZnO structure are labelled by vertical ticks and indices. Full circles, open circles, “plus” symbol and asterisks in the spectra denote the secondary phases  $\text{MnO}_2$ ,  $\text{Mn}_2\text{O}_3$ ,  $\text{Mn}_3\text{O}_4$  and  $\text{Zn}_{1-y}\text{Mn}_y\text{Mn}_2\text{O}_4$ , respectively.

The XRD pattern of the sample with a nominal manganese concentration  $x = 0.10$  thermally treated at 773 K in air is shown in Fig. 2, in which the impurity phase is

clearly observed. All the impurity XRD lines in this spectrum are indexed to  $\text{ZnMn}_2\text{O}_4$ , also with tetragonal symmetry (space group  $I4_1/amd$ ). The appearance of an impurity phase with the spinel structure  $(\text{Zn}_{1-x}\text{Mn(II)}_x)[\text{Mn(III)}_2]\text{O}_4$  having cubic symmetry was detected in Mn-doped ZnO nanoparticles prepared by a co-precipitation method after annealing the 2 and 5 % Mn-doped samples at temperatures  $1075 < T < 1275$  K.<sup>15</sup> The tetragonal phase of  $\text{ZnMn}_2\text{O}_4$  was observed in a ZnMnO bulk sample with 1 % Mn sintered in air at 1173 K.<sup>8</sup> The appearance of the  $\text{ZnMn}_2\text{O}_4$  phase in our Zn–Mn–O samples at a temperature of thermal treatment as low as 773 K was probably the result of the fast decomposition of the starting materials used in the synthesis.

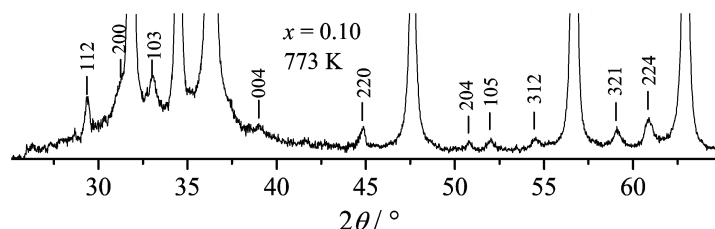


Fig. 2. X-Ray diffraction pattern at 300 K for the Zn–Mn–O sample with  $x = 0.10$  thermally treated at 773 K recorded at a slow scan rate. The vertical ticks and indices in the spectrum indicate the peak positions of tetragonal  $\text{ZnMn}_2\text{O}_4$ .

The XRD data were subject to Rietveld analysis. The ZnO lattice parameters of the dominant crystal phase in all the samples thermally treated at 773 K were found to be very close to the crystal lattice parameters of ZnO,  $a = 3.250$  Å and  $c = 5.207$  Å.<sup>16</sup> Changes of the  $a$  and  $c$  parameters with increasing temperature of thermal treatment from 673 to 1173 K are also not significant. These results are consistent with earlier observations that the solubility of Mn in the ZnO crystal lattice is low.<sup>8,10</sup> The average ZnO crystallite size determined from the width of the X-ray diffraction lines using the Scherrer formula was found to increase with increasing sintering temperature:  $d \approx 30, 50, 70, 70$  and  $100$  nm for the  $x = 0.01$  sample thermally treated at 673, 773, 873, 973 and 1173 K, respectively.

The XRD spectra of  $\text{MnO}_2$  untreated and thermally treated 12 h in air at 673, 773, 873, 973, 1073 and 1173 K are presented in Fig. 3. Up to 673 K,  $\text{MnO}_2$  is stable. At the temperature of 773 K, the  $\text{Mn}_2\text{O}_3$  phase developed and the sample consisted of equal proportions of  $\text{MnO}_2$  and  $\text{Mn}_2\text{O}_3$  (Fig. 4). At 873 K, the  $\text{MnO}_2$  sample was completely transformed into  $\text{Mn}_2\text{O}_3$  and at 1173 K, the  $\text{Mn}_3\text{O}_4$  phase appears.

The TG and DTA curves for the oxalate precursors and for a sample of unsintered mixture of  $(\text{ZnC}_2\text{O}_4 \cdot 2\text{H}_2\text{O})_{1-x}$  and  $(\text{MnC}_2\text{O}_4 \cdot 2\text{H}_2\text{O})_x$  with  $x = 0.01$  are presented in Fig. 5. The thermal decomposition of  $\text{ZnC}_2\text{O}_4 \cdot 2\text{H}_2\text{O}$  occurred in two stages, Fig. 5a. The first stage was dehydration (an endothermic process with  $T_{\text{max}} = 425$  K). The second stage was the decomposition of anhydrous zinc oxa-

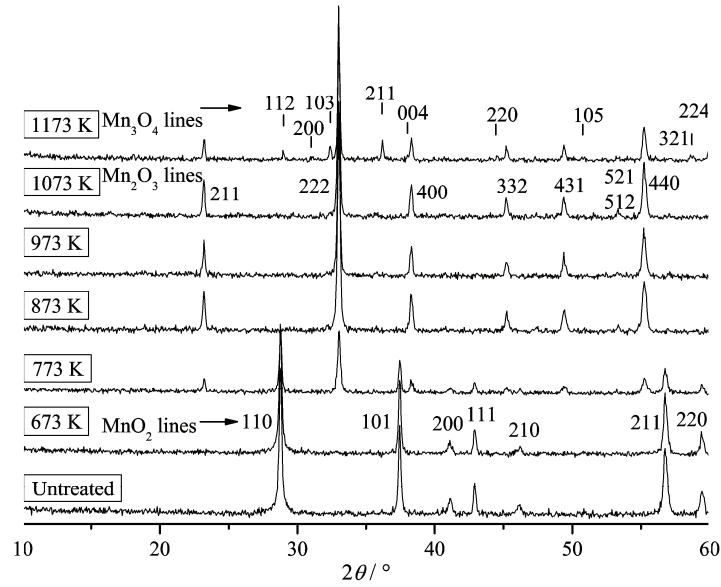


Fig. 3. X-Ray diffraction patterns at 300 K for MnO<sub>2</sub> untreated and thermally treated at temperatures 673–1173 K. The vertical ticks and indices indicate the peak positions of the corresponding manganese oxide noted on the left.

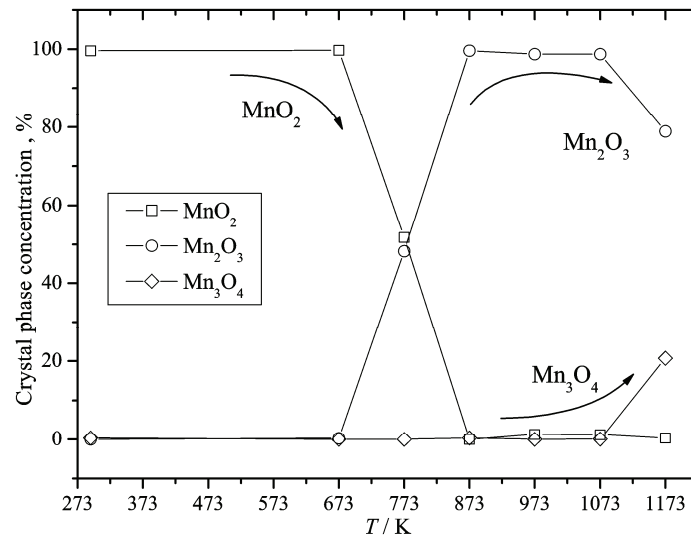


Fig. 4. Relative fraction of various manganese oxides developed after thermal treatment of MnO<sub>2</sub> at temperatures 673–1173 K.

late (an exothermic process with  $T_{\max} = 683$  K). The final solid product of this decomposition, found by XRD, was ZnO. The thermal decomposition of the unsintered mixture of two oxalates with  $x = 0.01$  occurred in three stages, Fig. 5b.

The first process was dehydration of the oxalates in the unsintered  $x = 0.01$  sample ( $T_{\max} = 430$  K). The event around  $T_{\max} = 686$  K involved decomposition of the zinc oxalate phase, and the process around  $T_{\max} = 598$  K was due to decarbonisation of the manganese oxalate in the sample. The same process of decarbonisation of the manganese oxalate in the starting  $\text{MnC}_2\text{O}_4 \cdot 2\text{H}_2\text{O}$  material occurred around  $T_{\max} = 592$  K, as can be seen in Fig. 5c. Taking into consideration the TG/DTA and XRD measurements, it appears that the ZnO phase in the studied Zn–Mn–O samples arose as a product of the decomposition of  $\text{ZnC}_2\text{O}_4 \cdot 2\text{H}_2\text{O}$ , whereas the  $\text{MnO}_2$  phase detected in the  $x = 0.01$  sample arose as a product of the decomposition of  $\text{MnC}_2\text{O}_4 \cdot 2\text{H}_2\text{O}$ .

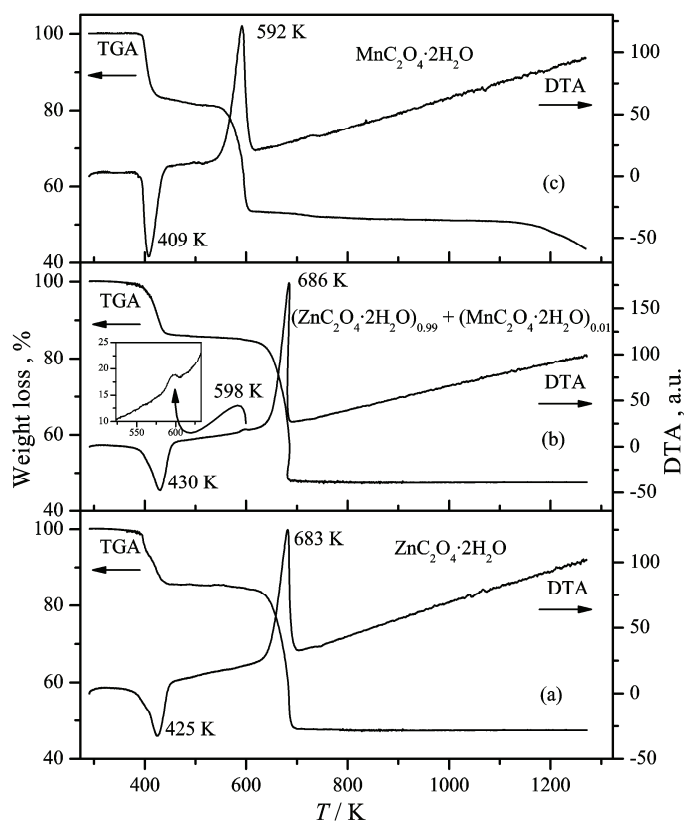


Fig. 5. TG and DTA curves for:  $\text{ZnC}_2\text{O}_4 \cdot 2\text{H}_2\text{O}$  (a), unsintered mixture of  $(\text{ZnC}_2\text{O}_4 \cdot 2\text{H}_2\text{O})_{1-x} + (\text{MnC}_2\text{O}_4 \cdot 2\text{H}_2\text{O})_x$  with  $x = 0.01$  (b) and  $\text{MnC}_2\text{O}_4 \cdot 2\text{H}_2\text{O}$  (c).

The particle size and morphology of one selected sample were characterized by transmission electron microscopy. A typical bright-field TEM image of the Zn–Mn–O sample, with  $x = 0.01$ , thermally treated at 773 K is shown in Fig. 6. TEM Analysis clearly revealed the presence of two types of particles: one was elongated with a faceted morphology and the other was nearly spherical in shape.

This implies that the two phases can be distinguished. The first is a hexagonal phase corresponding to ZnO recorded by XRD. The size of the ZnO crystallites with faceted morphology seen by TEM lies in the range 50–100 nm, which is consistent with the result obtained from the XRD patterns. The crystallites of the second phase in the TEM image appear in the form of nearly spherical particles. Most of the crystallites of nearly spherical shape have dimensions about 50 nm. These crystallites are attributed to the MnO<sub>2</sub> phase observed in the XRD spectrum of the  $x = 0.01$  sample, Fig. 1. A more detailed TEM analysis of the  $x = 0.01$  sample thermally treated at 773 K enabled the clarification of the coalescence of some ZnO and MnO<sub>2</sub> crystallites. The observed locations of coalescence of the two phases are denoted by arrows in Fig. 6.

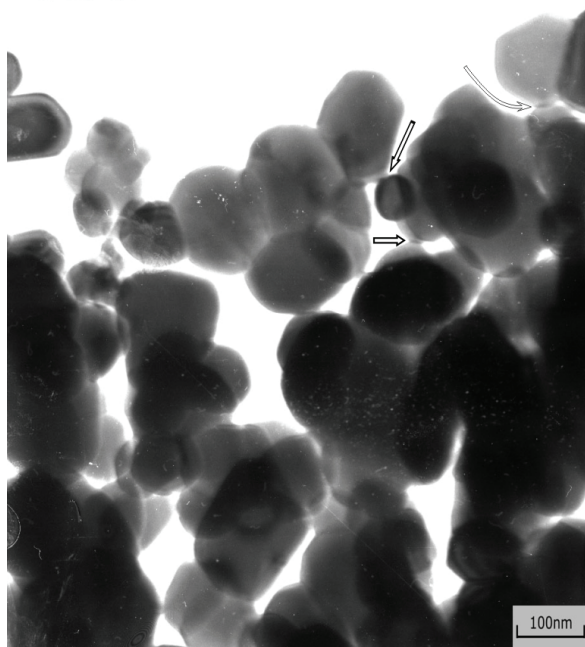


Fig. 6. TEM Microphotograph of the  $x = 0.01$  sample thermally treated at 773 K. The arrows in microphotograph denote the locations of coalescence of zinc oxide and manganese oxide crystallites.

The temperature dependence of magnetization under a magnetic field of 500 Oe for the Zn-Mn-O samples with  $x = 0.01$ , 0.04 and 0.10 thermally treated in air at 773 K for 12 h is presented in Fig. 7. At higher temperatures the magnetization of the  $x = 0.01$  sample was larger than that for the  $x = 0.04$  and 0.10 samples. The sample with  $x = 0.01$  showed a maximum in its  $M(T)$  dependence at about 65 K where the  $x = 0.04$  and 0.10 samples show a kink.

The magnetic field dependence of magnetization for the  $x = 0.01$  sample thermally treated at 673 K was observed at  $T = 250$  K (Fig. 8, curve 1) with a coercive field  $H_c = 80$  Oe and a remanent magnetization  $M_r = 0.0001$  emu/g. The  $M(H)$  dependence measured at 300 K for the  $x = 0.01$  sample thermally treated at

773 K was characterized by  $H_c = 800$  Oe and  $M_r = 0.0050$  emu/g (Fig. 8, curve 2). Subtracting the paramagnetic component from the total magnetization for the  $x = 0.01$  samples thermally treated at 673 and 773 K, the ferromagnetic component of the magnetization was evaluated with saturation value  $M_s = 0.0004$  emu/g and  $M_s = 0.0195$  emu/g for temperatures 673 and 773 K, respectively (Fig. 8). It can be seen that in the  $x = 0.01$  sample thermally treated at 773 K, the coercive field is ten times larger and saturation magnetization is about fifty times larger than the corresponding values for the sample thermally treated at 673 K.

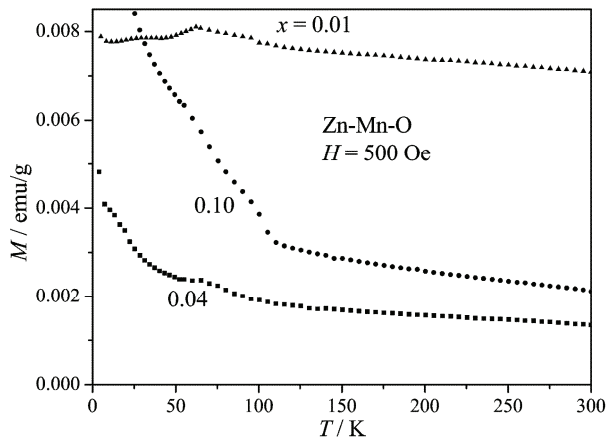


Fig. 7. Temperature dependence of the magnetization in the ZFC state at 500 Oe for Zn-Mn-O samples thermally treated at 773 K, with  $x = 0.01$ , 0.04 and 0.10.

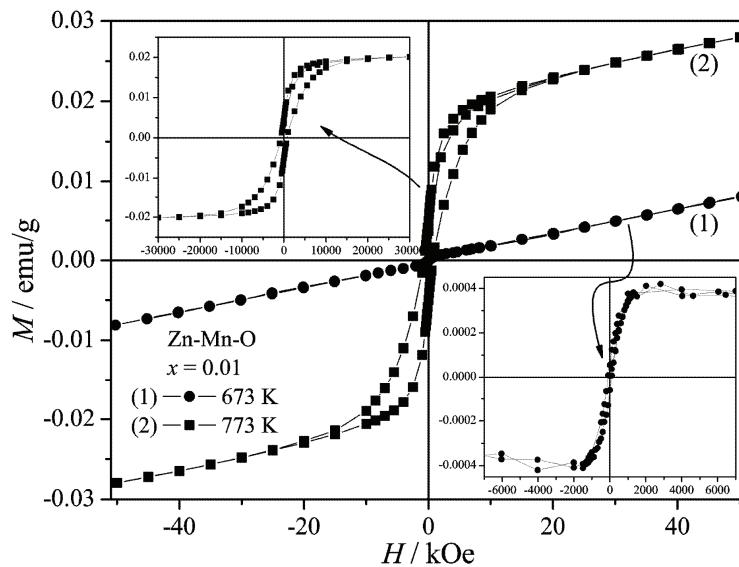


Fig. 8. Field dependent magnetization curves for the Zn-Mn-O samples with  $x = 0.01$  thermally treated at: 673 (1) and 773 K (2). The insets show the ferromagnetic component of the magnetization obtained after subtracting the paramagnetic contribution.

Contrary to these observations, there was no RT ferromagnetism in the  $x = 0.10$  sample thermally treated at 773 K nor in the  $x = 0.01$  sample thermally treated at 1173 K. The  $M(H)$  dependence for these samples was a linear function in the magnetic field range up to 50 kOe, indicating the paramagnetic origin of the magnetization at 300 K.

The EPR spectra of the studied Zn–Mn–O samples at 300 K are presented in Fig. 9. A broad resonance appeared in the  $x = 0.01$  and 0.04 samples thermally treated at 773 K on the lower field side, which was absent in the  $x = 0.10$  sample thermally treated at 773 K and in the  $x = 0.01$  sample thermally treated at 1173 K. The broad resonance is attributed to ferromagnetic phase in the material. The EPR spectrum in the form of fine and hyperfine lines was detected on the higher field side in all the investigated Zn–Mn–O samples (Fig. 9). This spectrum was analysed by the following spin-Hamiltonian:

$$H = g\mu_B \mathbf{HS} + D\left[S_z^2 - \frac{1}{3}S(S+1)\right] + ASI \quad (1)$$

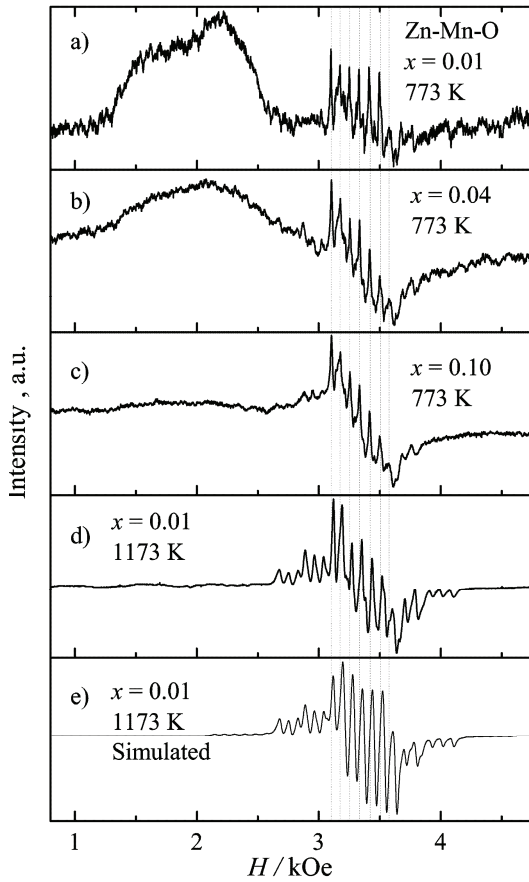


Fig. 9. EPR Spectra of the Zn–Mn–O samples: a)  $x = 0.01$  thermally treated at 773 K, b)  $x = 0.04$  thermally treated at 773 K, c)  $x = 0.10$  thermally treated at 773 K, d)  $x = 0.01$  thermally treated at 1173 K, e) simulated spectrum of  $\text{Mn}^{2+}$  with  $S = 5/2$  and  $I = 5/2$  in the ZnO crystal lattice (EPR parameters used in the simulation are  $A = -81$  G,  $D = -252$  G,  $g = 2.01$ ).

where the first term describes the Zeeman interaction, the second term describes the axial zero-field splitting due to the hexagonal symmetry of the wurtzite ZnO and the third term describes the hyperfine interaction between the electron and nuclear spins of the manganese ions. For the  $\text{Mn}^{2+}$ ,  $S = 5/2$ , there are five fine transitions in the magnetic field  $\mathbf{H}$ . Each fine transition has six hyperfine transitions due to the hyperfine interaction of the  $\text{Mn}^{2+}$  electron spin and its nuclear spin,  $^{55}\text{Mn}$  ( $I = 5/2$ ). Good agreement with the experimental spectrum for the sample  $x = 0.01$  thermally treated at 1173 K was obtained in the simulation using the spin-Hamiltonian parameters  $A = -81$  G,  $D = -252$  G and  $g = 2.01$ , Fig. 9e. These values agree well with the spin-Hamiltonian parameters ( $A = -81$  G,  $D = -232$  G and  $g = 2.0016$ ) reported for a  $\text{Mn}^{2+}$  doped ZnO single crystal.<sup>17,18</sup> Thus, the EPR spectrum appearing in all the investigated Zn–Mn–O samples arises from the paramagnetic moments of isolated  $\text{Mn}^{2+}$  substitutionally incorporated into the ZnO crystal lattice. The isolated (uncoupled)  $\text{Mn}^{2+}$  do not contribute to the RT ferromagnetism.

Taking into account the manganese concentration in the  $x = 0.01$  sample determined by an atomic absorption method, which was only a little less than that used in the synthesis,  $\approx 0.8$  at. %, and the measured saturation magnetization of the ferromagnetic phase in the sample thermally treated at 773 K, the average magnetic moment per Mn ion was found to be  $0.03 \mu_{\text{B}}/\text{Mn}$  at 300 K. A small value of the average magnetic moment per Mn ion was reported for bulk Mn-doped ZnO,<sup>4,19</sup> and in Mn-doped ZnO nanoparticles.<sup>15</sup>

TEM Analysis indicated that the coalescence of some zinc oxide and manganese oxide crystallites might cause microstructural changes (Fig. 6). It is very likely that at these locations, diffusion of zinc atoms into manganese oxide occurred. Clear evidence of this process is the appearance of the impurity phase in the thermally treated Zn–Mn–O samples detected by XRD analysis, which was identified as  $\text{Zn}_{1-y}\text{Mn}_y\text{Mn}_2\text{O}_4$  in the  $x = 0.01$  sample and as a  $\text{ZnMn}_2\text{O}_4$  phase in the  $x = 0.10$  sample. The reverse process of diffusion of manganese atoms into the zinc oxide crystallites also occurred. Substitutional incorporation of  $\text{Mn}^{2+}$  into the ZnO crystal lattice was recorded in the EPR spectra. It was found that isolated  $\text{Mn}^{2+}$  in the ZnO crystal lattice do not contribute to the RT ferromagnetism. Nor does the RT ferromagnetism originate from the  $\text{ZnMn}_2\text{O}_4$  phase. The  $\text{ZnMn}_2\text{O}_4$  phase with tetragonal symmetry was observed in the  $x = 0.10$  sample thermally treated at 773 K but RT ferromagnetism was not detected in this sample. The same applies to the  $\text{Zn}_{1-y}\text{Mn}_y\text{Mn}_2\text{O}_4$  phase. This impurity phase detected in the  $x = 0.01$  sample progressively developed with increasing temperature of thermal treatment up to the highest temperature used in the sintering procedure, 1173 K, but the  $x = 0.01$  sample thermally treated at 1173 K was fully paramagnetic at 300 K.

In addition to  $\text{Zn}_{1-y}\text{Mn}_y\text{Mn}_2\text{O}_4$ , another secondary phase,  $\text{MnO}_2$ , was detected in the  $x = 0.01$  sample thermally treated at 773 K. This manganese oxide is antiferromagnetic with a Néel temperature about 84 K.<sup>20</sup> Pure  $\text{MnO}_2$  transforms into  $\text{Mn}_2\text{O}_3$  at about 773 K (Fig. 4). Pure  $\text{Mn}_2\text{O}_3$  is also antiferromagnetic with a Néel temperature between 80 and 100 K.<sup>21</sup> In the presence of Zn atoms in  $\text{Mn}_2\text{O}_3$ , incorporation of Zn into  $\text{Mn}^{3+}$  sites is possible (the ionic radius of  $\text{Zn}^{2+}$  is about 0.60 Å and the ionic radius of  $\text{Mn}^{3+}$  is about 0.58 Å)<sup>22</sup> and this process causes oxygen release for charge neutrality and formation of vacancies in the  $\text{Mn}_2\text{O}_3$  structure. It is interesting to note that incorporation of Zn into  $\text{Mn}_3\text{O}_4$ , where Zn substitutes  $\text{Mn}^{2+}$  in the cation sublattice, leads to low-temperature ferrimagnetisms similar to that of  $\text{Mn}_3\text{O}_4$  but with a lower Curie temperature.<sup>7</sup> In the present investigation, RT ferromagnetism commenced to develop in the  $x = 0.01$  sample thermally treated at 673 K, Fig. 8. At this temperature (673 K), a large part of the zinc oxalate had decomposed into ZnO. The abrupt increase of the ferromagnetic component of the magnetization in the  $x = 0.01$  sample thermally treated at 773 K compared with that appearing at 673 K could be connected with the development of the  $\text{Mn}_2\text{O}_3$  phase observed in the XRD pattern, Fig. 1, where the creation of oxygen vacancies due to presence of Zn atoms was expected. An oxygen-vacancy-stabilized metastable phase in the form  $\text{Mn}_{2-x}\text{Zn}_x\text{O}_{3-\delta}$  was suggested as a possible source of the high-temperature ferromagnetism in the low-temperature processed Zn–Mn–O samples.<sup>7</sup> In several detailed studies, the diffusion of Zn atoms into the manganese oxides was also considered to be responsible for the observed high-temperature ferromagnetism in the low-temperature processed Zn–Mn–O bulk and some thin film multilayer samples.<sup>23,24</sup>

However, in a recently published paper, RT ferromagnetism in  $\text{Zn}_{1-x}\text{Mn}_x\text{O}$  thin films grown by pulsed laser deposition was observed even in those samples ( $x < 0.03$ ) which had no secondary phases.<sup>25</sup> The appearance of the  $\text{Mn}_2\text{O}_3$  phase aggregating at grain boundaries was found for a higher Mn concentration,  $x = 0.05$ , but this sample exhibited smaller saturation magnetization than that recorded for the thin films with lower manganese content. These results suggest that the high-temperature ferromagnetism in Zn–Mn–O is not necessarily related to manganese oxides or other impurity phases and that this phenomenon is an intrinsic property of Mn-doped ZnO materials. It was established in the present study that the solubility of Mn in low-temperature processed bulk ZnO was low and that manganese oxides existed even in the Zn–Mn–O sample with  $x = 0.01$  Mn doping.

There is a possibility that a fraction of the Mn ion magnetic moments incorporated in the ZnO crystal lattice in the  $x = 0.01$  sample thermally treated at 773 K was ordered ferromagnetically at RT and that the ferromagnetically coupled moments co-existed with the paramagnetic moments of the isolated Mn ions (Fig. 9a). The coexistence of ferromagnetically coupled Mn ion moments and

paramagnetic moments of isolated Mn ions was found in a  $\text{Zn}_{1-x}\text{Mn}_x\text{O}$  thin film sample with  $x = 0.01$ ,<sup>25</sup> and in 2 at. % Mn-doped ZnO nanocrystals with an average particle size 12 nm annealed at 673 K.<sup>15</sup> This possibility focuses attention on free charge carriers as mediators in the ferromagnetic ordering. Theoretical models identified *p*-type ZnO doped with Mn as a ferromagnetic semiconductor with a high  $T_C$ .<sup>1-3</sup> It is now well known that nitrogen is one of the most effective *p*-type doping agents in ZnO.<sup>26</sup> A film prepared from nitrogen-capped nanocrystals of 0.2 at. %  $\text{Mn}^{2+}:\text{ZnO}$  exhibited saturation magnetization of the ferromagnetically coupled  $\text{Mn}^{2+}$  moments of  $0.75 \mu_B/\text{Mn}$  at 300 K.<sup>5</sup> In a Mn-doped ZnO bulk sample with  $x = 0.3$  at. % Mn prepared from ZnO and  $\text{MnO}_2$  precursors by a sintering procedure at 773 K in air, a ferromagnetic ordering of the uniformly distributed  $\text{Mn}^{2+}$  moments was observed with a saturation magnetization of  $0.16 \mu_B/\text{Mn}$ .<sup>4</sup> It should be noted that a bulk Zn–Mn–O sample with 1.0 % Mn sintered at 773 K under vacuum exhibited weaker ferromagnetic properties at RT than the sample with 1.0 % Mn sintered at 773 K in air.<sup>8</sup> Contrary to this observation, the thermal treatment of a bulk  $\text{Zn}_{1-x}\text{Mn}_x\text{O}$  sample with  $x = 0.02$  at 873 K in an argon atmosphere resulted in considerably stronger ferromagnetic properties at 300 K than those for the sample sintered at the same temperature in air.<sup>19</sup> In a recent study of the electrical properties of nitrogen-doped ZnO thin films, it was found that the introduction of Ar in the growth ambient enhanced the hole concentration and improved the conductivity of N-doped ZnO.<sup>26</sup> In the present study, the Zn–Mn–O sample with  $x = 0.01$  prepared by the solid state sintering route, which was not intentionally doped with any kind of impurity, and with a final thermal treatment at 773 K in air, the saturation magnetization of the ferromagnetic phase was estimated to be  $0.03 \mu_B/\text{Mn}$  at 300 K. The very small value of the average magnetic moment per Mn ion in this ferromagnetic sample was partly the consequence of the small fraction of Mn ions participating in the ferromagnetic ordering. The common property of almost all the Zn–Mn–O samples prepared either in the bulk form by a solid state reaction method<sup>4,7,8,22,24</sup> or in the form of thin films,<sup>4</sup> or in the form of nanocrystalline particles<sup>15</sup> is that the RT ferromagnetism appeared in the low-temperature processed samples (673–873 K) and was absent in samples exposed to high-temperature treatment (above 1073 K). The magnetic properties of the Zn–Mn–O samples observed in the present study, as well as those reported by other authors, indicate that these properties are extremely sensitive to the conditions of sample preparation, where the type and concentration of defects play a very important role.

According to a theoretical study of the hole mediated ferromagnetism in  $\text{Mn}^{2+}:\text{ZnO}$ , the 3d electrons of  $\text{Mn}^{2+}$  were predicted to delocalize partially into the shallow acceptor states, thus providing exchange interaction and ferromagnetic coupling between the Mn ions.<sup>1</sup> Taking into consideration the conditions of synthesis of the low-temperature processed Zn–Mn–O samples in this study, it

seems that the observed RT ferromagnetism could originate from interactions between the  $Mn^{2+}$  and uncompensated acceptor defects incorporated in the ZnO crystal lattice during the thermal treatment of the samples.

#### CONCLUSIONS

Room temperature ferromagnetism was observed in Zn–Mn–O samples with  $x = 0.01$  thermally treated at 673 and 773 K, and in the  $x = 0.04$  sample thermally treated at 773 K. The structural and magnetic properties of the Zn–Mn–O samples showed that they were non-homogeneous materials. An analysis of the experimental results of this work suggests that the observed RT ferromagnetism in the low-temperature processed samples could arise from interactions between the  $Mn^{2+}$  and  $p$ -type defects incorporated in the ZnO crystal lattice during the thermal treatment of the samples.

*Acknowledgments.* Financial support for this study was granted by the Ministry of Science and Technological Development of the Republic of Serbia, Projects No. 141013 and 141027.

#### ИЗВОД

#### ФЕРОМАГНЕТНО ПОНАШАЊЕ Zn–Mn–O СИСТЕМА

БРАНКА БАБИЋ-СТОЈИЋ, ДУШАН МИЛИВОЈЕВИЋ и ЈОВАН БЛАНУША

*Институт за нукларне науке "Винча", б. бр. 522, 11001 Београд*

Поликристални узорци Zn–Mn–O номиналних концентрација мангана  $x = 0,01, 0,04$  и  $0,10$  добијени су реакцијом у чврстом стању између  $(ZnC_2O_4 \cdot 2H_2O)_{1-x}$  и  $(MnC_2O_4 \cdot 2H_2O)_x$ . Термички третман је извршен на ваздуху и температурама 673, 773, 873, 973 и 1173 K за  $x = 0,01$  и на температури 773 K за  $x = 0,04$  и  $0,10$ . Узорци су испитивани методама дифракције  $x$ -зрака на праху, термогравиметрије, диференцијалне термалне анализе, трансмисионе електронске микроскопије, мерења магнетизације и електронске парамагнетне резонанце. Методом дифракције  $x$ -зрака на праху су испитани и узорци  $MnO_2$  термички третиран на температурама 673, 773, 873, 973, 1073 и 1173 K. Феромагнетизам на собној температури је уочен у Zn–Mn–O узорцима концентрације мангана  $x = 0,01$  термички третираним на ниским температурама (673 и 773 K) и у узорку  $x = 0,04$  термички третираном на 773 K. Резултати указују на то да би феромагнетизам могао да буде последица интеракције између  $Mn^{2+}$  и акцепторских дефеката уграђених у кристалну решетку ZnO за време термичког третмана узорака.

(Примљено 26. маја, ревидирано 16. јула 2008)

#### REFERENCES

1. T. Dietl, H. Ohno, F. Matsukura, J. Cibert, D. Ferrand, *Science* **287** (2000) 1019
2. K. Sato, H. Katayama-Yoshida, *Japan J. Appl. Phys.* **39** (2000) L555
3. K. Sato, H. Katayama-Yoshida, *Semicond. Sci. Technol.* **17** (2002) 367
4. P. Sharma, A. Gupta, K. V. Rao, F. J. Owens, R. Sharma, R. Ahuja, J. M. Osorio Guillen, B. Johansson, G. A. Gehring, *Nat. Mater.* **2** (2003) 673
5. K. R. Kittilstved, N. S. Norberg, D. R. Gamelin, *Phys. Rev. Lett.* **94** (2005) 147209
6. A. Manivannan, P. Dutta, G. Glaspell, M. S. Seehra, *J. Appl. Phys.* **99** (2006) 08M110

7. D. C. Kundaliya, S. B. Ogale, S. E. Lofland, S. Dhar, C. J. Metting, S. R. Shinde, Z. Ma, B. Varughese, K. V. Ramanujachary, L. Salamanca-Riba, T. Vankatesan, *Nat. Mater.* **3** (2004) 709
8. J. Zhang, R. Skomski, D. J. Sellmyer, *J. Appl. Phys.* **97** (2005) 10D303
9. S. Kolesnik, B. Dabrowski, J. Mais, *J. Appl. Phys.* **95** (2004) 2582
10. G. Lawes, A. S. Risbud, A. P. Ramirez, R. Seshadri, *Phys. Rev.* **B71** (2005) 045201
11. H. W. Zhang, E. W. Shi, Z. Z. Chen, X. C. Liu, B. Xiao, *Solid State Commun.* **137** (2006) 272
12. A. Tiwari, C. Jin, A. Kvit, D. Kumar, J. F. Muth, J. Narayan, *Solid State Commun.* **121** (2002) 371
13. T. Fukumura, Z. Jin, M. Kawasaki, T. Shono, T. Hasegawa, S. Koshihara, H. Koinuma, *Appl. Phys. Lett.* **78** (2001) 958
14. S. W. Jung, S. J. An, G. C. Yi, C. U. Jung, S. I. Lee, S. Cho, *Appl. Phys. Lett.* **80** (2002) 4561
15. O. D. Jayakumar, H. G. Salunke, R. M. Kadam, M. Mohapatra, G. Yaswant, S. K. Kulshreshtha, *Nanotechnology* **17** (2006) 1278
16. S. J. Pearton, W. H. Heo, M. Ivill, D. P. Norton, T. Steiner, *Semicond. Sci. Technol.* **19** (2004) R59
17. P. B. Dorain, *Phys. Rev.* **112** (1958) 1058
18. A. Hausmann, H. Huppertz, *J. Phys. Chem. Solids* **29** (1968) 1369
19. W. Chen, L. F. Zhao, Y. Q. Wang, J. H. Miao, S. Liu, Z. C. Xia, S. L. Yuan, *Appl. Phys. Lett.* **87** (2005) 042507
20. B. D. Cullity, *Introduction to Magnetic Materials*, Addison–Wesley Publishing Company, Merlo park, CA, 1972, p. 157
21. M. Regulski, R. Przeniosło, I. Sosnowska, D. Hohlwein, R. Schneider, *J. Alloys Compounds* **362** (2004) 236
22. K. P. Bhatti, S. Chaudhary, D. K. Pandya, S. C. Kashyap, *Solid State Commun.* **136** (2005) 384
23. J. L. Costa-Krämer, F. Briones, J. F. Fernández, A. C. Caballero, M. Villegas, M. Díaz, M. A. García, A. Hernando, *Nanotechnology* **16** (2005) 214
24. M. A. García, M. L. Ruiz-González, A. Quesada, J. L. Costa-Krämer, J. F. Fernández, S. J. Khatib, A. Wennberg, A. C. Cabarello, M. S. Martín- González, M. Villegas, F. Briones, J. M. González-Calbet, A. Hernando, *Phys. Rev. Lett.* **94** (2005) 217206
25. J. Zhang, X. Z. Li, J. Shi, Y. F. Lu, D. J. Sellmyer, *J. Phys. Condens. Matt.* **19** (2007) 036210
26. J. Lu, Q. Liang, Y. Zhang, Z. Ye, S. Fujita, *J. Phys. D: Appl. Phys.* **40** (2007) 3177.



www.shd.org.rs

*J. Serb. Chem. Soc.* 74 (1) 85–92 (2009)  
JSCS–3811

Journal of  
the Serbian  
Chemical Society

JSCS@tmf.bg.ac.yu • www.shd.org.rs/JSCS

UDC 628.1.033:546.19:549.73–188+541.183

Original scientific paper

## Removal of inorganic As<sup>5+</sup> from a small drinking water system

MARJANA SIMONIČ\*

*University of Maribor, Faculty of Chemistry and Chemical Engineering,  
Smetanova 17, 2000 Maribor, Slovenia*

(Received 20 December 2007, revised 11 April 2008)

**Abstract:** The drinking water from a small drinking water system contained arsenic in a concentration of about 50 µg/L. Chemical analyses showed that the pentavalent form of arsenic was present. Since the MCL value is 10 µg/L, it was necessary to implement a technological treatment to make the water suitable for drinking. In order to do so, two technologies were suggested: activated alumina and α-FeOOH (TehnoArz, TA) adsorption media. Experiments using both adsorption media were performed on a laboratory scale. It was possible to remove arsenic to below 1 µg/L. The maximal adsorption capacity was found to be 12.7 mg of As<sup>5+</sup> per gram of α-FeOOH. Moreover, all the important physico-chemical parameters of the water remained practically unchanged after the treatment. Only a slight release of iron from the media was observed. The Fe–As bond was studied by means of chemical analysis and X-ray powder diffraction. Finally, in addition to showing the capability of arsenic removal by α-FeOOH, a comprehensive optimization of the technological parameters of the selected technology is provided.

**Keywords:** drinking water; arsenic; activated alumina (AA); goethite; adsorption.

### INTRODUCTION

In 2004, arsenic became to be regarded as a highly toxic substance by the US EPA and European Union with a maximum level of contamination MCL of 10 µg/L. It was confirmed that arsenic causes skin, liver, lung, and kidney cancer. Arsenic naturally occurs in water because of mineral dissolution from the parent rock and abandoned coal mines. Due to human pollution, 21 countries around the world are affected by arsenic contamination of groundwater.<sup>1</sup> Anthropogenic activities, such as mining and smelting and the use of pesticides, wood preservatives and fossil fuels have resulted in a dramatic effect on the levels of natural environmental arsenic. Bangladesh and the West Bengal State in India have the most severe arsenic problems, with concentration in mg/L range.<sup>2,3</sup>

\* Corresponding author. E-mail: marjana.simonic@uni-mb.si  
doi: 10.2298/JSC0901085S

Arsenic occurs in the oxidation states  $-3$ ,  $0$ ,  $3$  and  $5$ , yielding a variety of inorganic and organic compounds. In short, the inorganic species consist of arsenate and arsenite, while the organic consist of monomethylarsonic acid and dimethylarsonic acid. Other arsenic-containing organic compounds are also found in the environment, such as arsenobetaine, methylarsonate (MA), dimethylarsonate (DMA) and trimethylarsine oxide (TMAO). The toxicity decreases in the order arsine  $>$  inorganic  $\text{As}^{3+}$   $>$  organic  $\text{As}^{3+}$   $>$  inorganic  $\text{As}^{5+}$   $>$  organic  $\text{As}^{5+}$   $>$  arsonium compounds and elemental arsenic.<sup>4</sup>

The methods for the removal arsenic are explained in detail in the literature.<sup>1,5</sup> The existing removal processes include oxidation using Fenton's reagent, catalytic materials such as manganese dioxide coated sand, black iron removal material BIRM, green sand, UV irradiation, dissolved oxygen oxidation followed by a powdered activated carbon, coagulation by Fe- or Al-salts, ion exchange, activated alumina, AA, and membrane separation. It is very important to establish the form in which the arsenic is present in the water, because the pentavalent form is easier to remove than the trivalent form.

Lafferty<sup>6</sup> studied the efficiency of iron oxides in the removal of arsenic from water. According to literature data,<sup>7-12</sup> goethite showed a very good adsorption capacity for organic and inorganic arsenic species. Goethite is, therefore, a promising adsorption media for the removal of inorganic  $\text{As}^{5+}$  from water. Sherman<sup>13</sup> studied the mechanism of arsenate ( $\text{AsO}_4^{3-}$ ) ion sorption to oxide hydroxides ( $\alpha$ -FeOOH). At the pH and pore water concentrations of the reservoir, arsenite remained sorbed to labile iron solid phases until they underwent reductive dissolution.<sup>14</sup> Also, Tripathy reported an enhanced efficiency of arsenic removal by alum coated activated alumina.<sup>15</sup>

The aim of this study was to investigate which of the two chosen adsorption media is the most adequate for  $\text{As}^{5+}$  removal and to provide the optimum parameters of selected technology for small communities.

## EXPERIMENTAL

### *Materials and analytical methods*

Activated alumina (AA) was obtained from Alcan Chemicals, the Netherlands, and TehnoArz (TA) from Tehnobiuro, Slovenia; TA is a commercial name for  $\alpha$ -FeOOH.

All the employed chemical substances were of a high degree of purity (p.a.).

Analyses of  $\text{Fe}^{2+}$ ,  $\text{Mn}^{2+}$ ,  $\text{Cl}^-$ ,  $\text{NO}_2^-$ ,  $\text{NO}_3^-$ ,  $\text{PO}_4^{3-}$  and  $\text{SO}_4^{2-}$ , were done spectroscopically using a Cary instrument, based on standard methods (DIN 38406, DIN 38405-D19).

The concentrations of  $\text{K}^+$  and  $\text{Na}^+$  were measured by atomic absorption spectrometry using a Perkin-Elmer 1100 B spectrometer with the appropriate source of radiation (DIN 38406 E-13, E-14, E-15).

$\text{Ca}^{2+}$ ,  $\text{Mg}^{2+}$  and  $\text{HCO}_3^-$  were determined titrimetrically by standard methods (DIN 38409 H6).

The pH was measured using a pH meter MA 5740, after calibration with buffers of pH 4.0 and 7.0 (DIN 38404-C5).

X-Ray powder diffraction data was collected with an AXS-Bruker/Siemens/D5005 diffractometer using  $\text{CuK}\alpha$  radiation at 293(1) K. The samples were PSD fast scanned and measured in the  $2\theta$  range 10–80°. The measuring times were from 47 to 52 h with a step of 0.014 and a scanning speed of 2 s per step. The values for the divergence and anti-scattering slit were fixed at 0.2 mm. The X-ray diffraction pattern was indexed with the help of automatic indexing programs TREOR and ITO. For the determination of the end product, the Search/Match program was used.<sup>15</sup>

The concentrations of arsenic were analysed using a Perkin–Elmer Elan 6100 ICP–MS instrument. All samples were filtered through a 0.45- $\mu\text{m}$  filter (Whatman Autovial), acidified and stored at 5.0 °C until analysed. Arsenic analysis using ICP has a relative standard deviation of less than 5 %.

#### *Water sampling, characteristics and purification*

The water well is situated under the Pohorje Hill and rises from an abandoned mining site. Arsenic may have been released into the environment through the mining process. A groundwater aquifer is the source of the water. The internal pressure is high enough to push the water up to the surface. The water flows from the rock through a 2.5 cm diameter tube. The water flow has been constant at 18000 m<sup>3</sup> per year for a long period of time (over 100 years).

The water samples were taken directly at the spring, according to the water quality sampling guidance on the preservation and handling of samples standard method (ISO 5667-3; 96). All water samples were stored in brown glass bottles and kept cool (at 4.0 °C) during transport to the laboratory, where they were processed the day after sampling campaign. The water was odourless, colourless and tasteless. All measured parameters are presented in Table I. Three replicates were made for all measurements and very good reproducibility was obtained. There was no iron, manganese, nitrite or phosphate in water, as can be seen from Table I. According to the EU legislation, the concentration of arsenic is too high. Thus, it should be removed before the water is used for drinking.

Two water purification procedures were selected: adsorption on activated alumina (AA) and on goethite  $\alpha\text{-FeOOH}$  (TA).

The water was filtered through an AA column of diameter 3.2 cm and height 1.0 m at a velocity of 10 to 40 m/h.

The water was filtered through a TA column of diameter 3.2 cm and height 30 cm at a velocity of about 10 m/h (Fig. 1).



Fig. 1. Laboratory equipment for arsenic removal with  $\alpha\text{-FeOOH}$  (TA) filter media.

### Adsorption studies

The equilibrium adsorption measurements consisted of mixing various amounts of adsorbent (1–2 g) with a fixed mass of test liquid in stoppered flasks, which were shaken for at least 24 h (the time required for each system to reach equilibrium had previously been determined by contact time experiments). Preliminary purging was necessary to eliminate the effects of oxidative coupling of the adsorbates. The adsorbent was subsequently separated by filtration and the filtrate analysed by ICP–MS for residual adsorbate concentration.

### RESULTS AND DISCUSSION

Preliminary tests made using HPLC–HG–AFS<sup>16</sup> showed that the drinking water source contained As in the inorganic pentavalent form.

The obtained results of physico–chemical analyses are presented in Table I for both arsenic removal procedures.

TABLE I. Physico–chemical parameters of the water before and the after treatment procedures

Parameters	Water	AA	TA
pH	7.6	7.8	7.6
$c(\text{As}) / \mu\text{g L}^{-1}$	50	6	0.2
$c(\text{Na}^+) / \text{mg L}^{-1}$	4	11	4
$c(\text{K}^+) / \text{mg L}^{-1}$	1.5	1.5	1.5
$c(\text{Ca}^{2+}) / \text{mg L}^{-1}$	53	50	55
$c(\text{Mg}^{2+}) / \text{mg L}^{-1}$	44	40	43
$c(\text{Fe}^{2+}) / \text{mg L}^{-1}$	< 0.05	< 0.05	< 0.05
$c(\text{Cl}^-) / \text{mg L}^{-1}$	6	6	6
$c(\text{NO}_3^-) / \text{mg L}^{-1}$	15	15	15
$c(\text{SO}_4^{2-}) / \text{mg L}^{-1}$	22	23	20
$c(\text{HCO}_3^-) / \text{mg L}^{-1}$	330	330	330

The removal of arsenic from the drinking water was successful. As presented in Table I, the pH value increased from 7.6 to 7.8 after treatment with AA. The concentration of  $\text{Na}^+$  remained practically unchanged when using TA, while the concentration increased after adsorption on AA. Slight oscillations were observed for the concentrations of Ca and Mg ions.

The concentrations of arsenic ions were reduced to under the MCL value by both the employed methods. The experiments were repeated several times and the results were always the same as presented in Table I.

It is clear that water purified in this way agrees with the standards for drinking waters.

The Freundlich model is defined by Eq. (1):

$$q = K \gamma_e^{1/n} \quad (1)$$

where  $q$  is the mass adsorbed per mass of media (mg/g) and  $\gamma_e$  is the equilibrium concentration of adsorbate (mg/L).

The parameters of the model were calculated from measured data (Fig. 2):  $K = 25.1$  and  $1/n = 0.1439$ . The model reasonably described the experimental values.

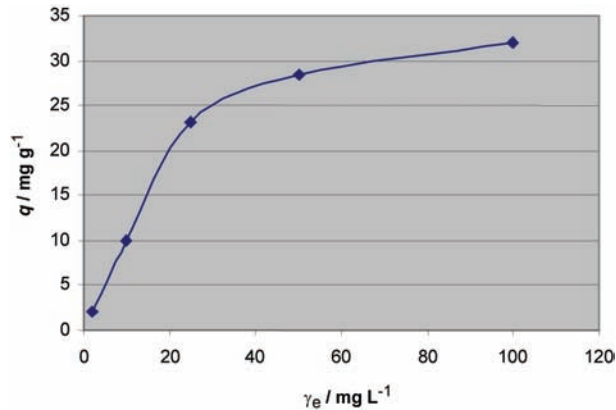


Fig. 2. Experimental adsorption isotherms at 25 °C and pH 7.6.

Tests showed that the AA and TA filtration efficiency was quite high. If  $q$  is the mass adsorbed per mass of media (mg/g),  $\gamma_0$  is the As<sup>5+</sup> influent concentration (mg/L) and  $\gamma_1$  is the As<sup>5+</sup> effluent concentration (mg/L), the bed life  $Y$ , the volume of water that can be treated per mass unit of AA (L/g), can be calculated:

$$Y = \frac{q}{\gamma_0 - \gamma_1} \quad (2)$$

Since  $q$  for AA was determined as 2 mg/g,<sup>17</sup>  $Y$  for AA was calculated to be 48.8 L/g.  $Y$  for TA was determined as 311 L/g, according to Eq. (2).

Thus, the adsorption capacity using TA was much higher than when AA was used. Therefore, the following parameters were suggested:

- Water flow: 0.50 m<sup>3</sup>/h;
- Daily water need: 2.0 m<sup>3</sup>/d;
- $\gamma(\text{As})$ : 0.050 mg/L;
- TA mass: 2860 g;
- TA height: 1.0 m;
- Column diameter: 22 cm;
- Contact time: 275 s;
- Pump power: 0.75 kW.

If the water flow is assumed at 2000 L/d,  $\gamma(\text{As})$  is 0.050 mg/L and the adsorption capacity 12.74 mg/g, the TA bed life was calculated as 443 days or approximately 1.2 year. After this period, it would have to be replaced.

The release of iron ions from the medium was monitored. From Fig. 3 it is seen that the concentration of iron ions increases slightly. After 50 days, the

concentration was still below 0.01 mg/L. It could be concluded that the concentration will not rise above the 0.02 mg/L before replacement of the media.

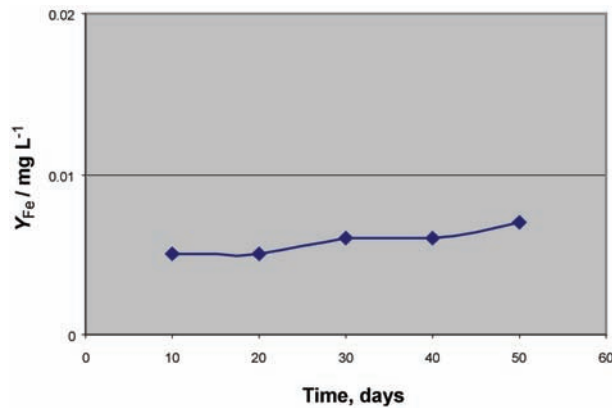


Fig. 3. The release of iron ions with time.

The type of the Fe–As bond was characterized, in addition to chemical analysis, also by X-ray powder diffraction analysis. With powder diffraction analyses, arsenic as  $\text{AsO}_4^{3-}$  forms a strong bond to  $\alpha\text{-Fe}_2\text{O}_3$  and  $\alpha\text{-FeOOH}$ . The mechanism has not yet been fully explained. Powder diffraction analysis of TA, shown in Fig. 4, showed that the arsenic was bound to Fe in the form  $\alpha\text{-FeOOH}$  and  $\text{Fe}_2\text{O}_3$ .

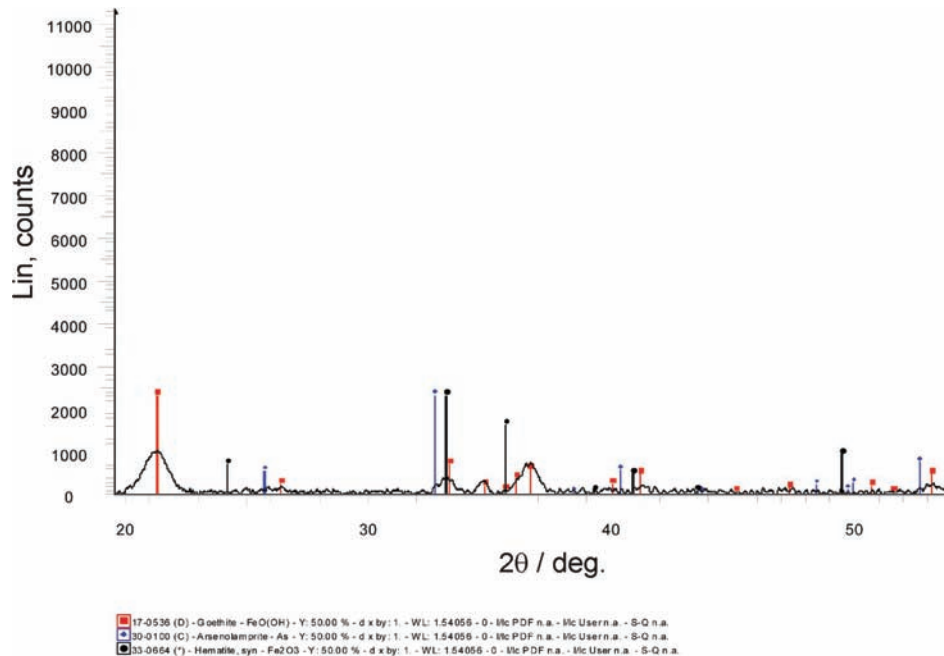


Fig. 4. Powder X-ray diffraction pattern of TA.

First, 1.0 g of TA was stirred in a water sample with 20 mg/L  $\text{As}^{5+}$ . After the equilibrium had been attained, it was dried and subjected to X-ray powder diffraction analysis. The same material was mixed with rainwater and left first for a week, and then for a month. The As concentrations were measured in the water before and after stirring. The As ions were bound strongly to the TA and they did not re-dissolve into the water, thus the concentration of arsenic in all samples did not change. Also, X-rays powder diffractograms were made for both dried samples: they did not differ one from the other at all. All three diffractograms were very similar to the shown in Fig. 4. This proved that the spent material could be discharged to a landfill without the fear of As leaking to the ground water sources.

TA adsorption is cost effective. It was calculated that the capital cost would be 11,740 Euros and the operational costs, including maintenance, would be at the same level. Thus, the process could be fully implemented for such a small water plant.

#### CONCLUSIONS

$\alpha\text{-FeOOH}$  was shown to be the most adequate adsorption media for arsenic removal for a small water system. The mass concentration of pentavalent arsenic in the source water was about 50  $\mu\text{g/L}$ . The results showed that arsenic was removed below the MCL value of 10  $\mu\text{g/L}$  by adsorption on activated alumina and  $\alpha\text{-FeOOH}$ . The obtained adsorption capacity of  $\alpha\text{-FeOOH}$  was 12.7 mg/g, and the determined contact time was 4.5 min. For small ground water systems, the implementation of  $\alpha\text{-FeOOH}$  (TA) adsorbent is more efficient than activated alumina. X-Ray powder diffraction analysis proved that arsenic as  $\text{AsO}_4^{3-}$  forms a strong bond to TA.

#### ИЗВОД

#### УКЛАЊАЊЕ $\text{As}^{5+}$ ИЗ МАЛОГ СИСТЕМА ЗА ПИЈАЋУ ВОДУ

MARJANA SIMONIČ

*University of Maribor, Faculty of Chemistry and Chemical Engineering, Smetanova 17, 2000 Maribor, Slovenia*

Вода из малих система за пијаћу воду садржала је арсен у концентрацији од око 50  $\mu\text{g/L}$ . Хемијске анализе су показале да је арсен присутан у петовалентном стању. Пошто је MCL вредност 10  $\mu\text{g/L}$ , неопходно је применити технолошки третман да би се вода учинила погодном за пиће. За то се предлажу две технологије: са употребом активираних алумина и  $\alpha\text{-FeOOH}$  као адсорпционих медијума. Изведени су експерименти на лабораторијском нивоу који користе оба адсорпциона медијума. Било је могуће смањити концентрацију арсена на испод 1  $\mu\text{g/L}$ . Нађен је максимални адсорпциони капацитет од 12,7 mg  $\text{As}^{5+}$  по граму  $\alpha\text{-FeOOH}$ . Такође, сви важни физичко-хемијски параметри остали су практично неизмењени након третмана. Уочено је само незнатно ослобађање гвожђа из медијума. Испитивана је веза Fe-As хемијском анализом и дифракцијом x-зрака праха. Коначно, уз приказ капацитета уклањања арсен помоћу  $\alpha\text{-FeOOH}$  дата је и детаљна оптимизација технолошких параметара одабране технологије.

(Примљено 20. децембра 2007, ревидирано 11. априла 2008)

## REFERENCES

1. D. Mohan, C. U. Pittman, Jr., *J. Hazard. Mater.* **142** (2007) 1
2. WHO, *Guidelines for Drinking Water Quality*, Vol. 1, Recommendations, Geneva, 1996
3. M. Bissen, F. H. Frimmel, *Acta Hydroch. Hydrob.* **31** (2003) 97
4. AWWA, *Water Quality and Treatment*, 5<sup>th</sup> Ed., McGraw Hill, New York, 1999
5. US EPA, *Technologies and costs for removal of arsenic from drinking water*, EPA 815-R-00-028, December 2000
6. B. J. Lafferty, R.H. Loeppert, *Environ. Sci. Technol.* **39** (2005) 2120
7. C. Luengo, M. Brigante, M. Avena, *J. Colloid Interf. Sci.* **311** (2007) 354
8. S. D. Smith, M. Edwards, *J. AWWA* **94** (2001) 1
9. J. S. Zhang, R. S. Stanforth, S. O. Pehkonen, *J. Colloid Interf. Sci.* **306** (2007) 16
10. J. S. Zhang, R. S. Stanforth, S. O. Pehkonen, *J. Colloid Interf. Sci.* **317** (2008) 35
11. J. Giménez, M. Martínez, J. de Pablo, M. Rovira, L. Duro, *J. Hazard. Mater.* **141** (2007) 575
12. D. M. Shermann, S. R. Randall, *Geochim. Cosmochim. Acta* **67** (2003) 4223
13. I. Ban, M. Kristl, M. Drogenik, A. Popovič, *Thermochim. Acta* **419** (2004) 253
14. R. A. Root, S. Dixit, K. M. Campbell, A. D. Jew, J. G. Hering, P. A. O'Day, *Geochim. Cosmochim. Acta* **71** (2007) 5782
15. S. S. Tripathy, A. M. Raichur, *Chem. Eng. J.* 138 (2008) 179
16. Z. Šlejkovec, *Talanta* **49** (1999) 619
17. M. Simonič, *Sanitary Eng.* **1** (2007) 47 (in Slovenian).



www.shd.org.rs

*J. Serb. Chem. Soc.* 74 (1) 93–102 (2009)  
JSCS–3812

Journal of  
the Serbian  
Chemical Society

JSCS@tmf.bg.ac.yu • www.shd.org.rs/JSCS

UDC 546.17–032.6+631.415:66.095.81:66.091  
Original scientific paper

## Specific transformations of mineral forms of nitrogen in acid soils

MIRJANA KRESOVIĆ<sup>1</sup>, MIODRAG JAKOVLJEVIĆ<sup>1</sup>, SRDJAN BLAGOJEVIĆ<sup>1\*#</sup>  
and SRBOLJUB MAKSIMOVIĆ<sup>2</sup>

<sup>1</sup>Faculty of Agriculture, Nemanjina 6, 11080 Zemun, Belgrade and <sup>2</sup>Institute of  
soil science, Teodora Drazera 7, 11000 Belgrade

(Received 21 March, revised 30 June 2008)

**Abstract:** Investigations were performed on soils of different acidity, ranging in the pH interval 4.65–5.80 (in water). Changes of the mineral nitrogen forms in the examined soils were studied by applying short-term incubation experiments performed under aerobic conditions, with a humidity of 30 % and a temperature of 20 °C, both with and without the addition of 100 and 300 ppm NH<sub>4</sub>-N. The results of the incubation experiments showed that retarded nitrification was present in all the examined soils. Increased and toxic quantities of nitrites (35.7 ppm) were formed during the incubation, which remained in the soil solution for several days, and even weeks, in spite of favorable conditions of moisture, aeration and temperature for the development of the process of chemoautotrophic nitrification. Decelerated chemoautotrophic nitrification was the source of the occurrence of nitrite in the examined less acid soil (soil 1), while in soils of higher acidity (soils 2 and 3) after addition of 100 and 300 ppm NH<sub>4</sub>-N, nitrite occurred due to chemical denitrification (chemodenitrification). Nitrites formed in the process of chemodenitrification underwent spontaneous chemical oxidation resulting in nitrate formation (chemical nitrification). The content of mineral nitrogen (NH<sub>4</sub> + NO<sub>3</sub> + NO<sub>2</sub>-N) decreased during the incubation period, proving gaseous losses from the examined soils. Application of lower doses of nitrogen fertilizers could decrease nitrogen losses by denitrification as well as the occurrence of nitrite in toxic quantities in the investigated pseudogley soil.

**Keywords:** incubation; mineral nitrogen; nitrification; denitrification; chemodenitrification.

### INTRODUCTION

The processes of mineralization and nitrification represent integral parts of the cycle of nitrogen circulation in soil.

\* Corresponding author. E-mail: sblagoje@eunet.yu

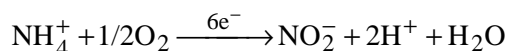
# Serbian Chemical Society member.

doi: 10.2298/JSC0901093K

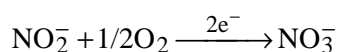
Nitrogen mineralization in soil is a process in which organic nitrogen compounds are decomposed releasing non-organic nitrogen ( $\text{NH}_4\text{-N}$ ). Non-specific microorganisms (bacteria, actinomycetes, fungi) participate in the mineralization process. As for the ambient conditions involved in the mineralization process, the content of organic matter in the soil has the biggest influence while the influence of soil acidity is a little smaller, bearing in mind that this process also occurs in an acidic environment. This is because fungi, being acidophilic microorganisms, play a significant role in the transformation of organic nitrogen compounds. In neutral and alkaline soils, mineralization develops due to the presence of bacteria.<sup>1</sup>

The largest differences in the nitrogen circulation cycle in acid soils refer to the nitrification process.

Biological nitrification is an extremely specific process in soil, with the participation of specific microorganisms from the group of real bacteria. The process of biological nitrification is performed in two phases, namely: ammonia oxidation (nitritation) with the participation of *Nitrosomonas*:

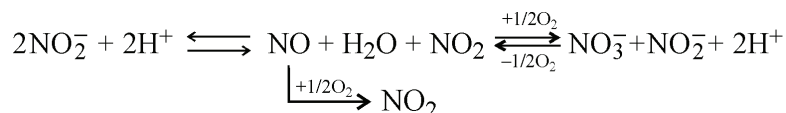


and nitrite oxidation (nitration), with the participation of *Nitrobacter*:



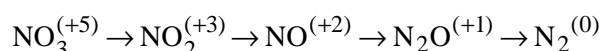
Nitrification bacteria are sensitive to the influence of the external environment, where the pH value of the soil represents one of the limiting factors. Thus, a pH value of 4.5 (water) is taken as the lower threshold for the activity of autotrophic nitrifiers.<sup>2</sup> In addition to this, high levels of ammonium nitrogen can also inhibit the activity of *Nitrobacter*, resulting in an accumulation of  $\text{NO}_2\text{-N}$  in soil.<sup>3,4</sup> Nitrification in acid soils has some specific features differing to that in neutral and alkaline soils. Namely, in acid soils, due to the higher sensitivity of nitrate bacteria to the low pH value of the soil, nitrification is often significantly slower resulting in nitrite accumulation.<sup>5</sup> Thus, nitrites in acid soils are accumulated, their quantity is rather small (several ppm) but sufficient to have a toxic influence on plants and microorganisms, especially if higher concentrations exist for a longer period.

In very acid soils (pH lower than 4.5 in 1.0 M KCl), a chemical oxidation of nitrites into nitrates (chemical nitrification) is possible, whereby the nitrite nitrogen acts as a self-donor and acceptor of electrons.<sup>6,7</sup> The process of chemical nitrification can be presented by the following reaction:



Bearing in mind the fact that nitrites are formed in the first phase of nitrification (nitritation), they can be found in the soil as a result of the denitrification process. Denitrification process in a wider sense means gaseous nitrogen losses from the soil in a microbiological or chemical way where volatilization is excluded.

The process of biological denitrification can be presented as:



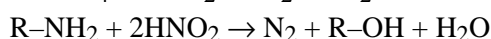
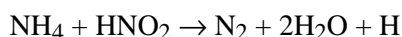
In this process, nitrites occur as intermediate products since the denitrification bacteria reduce  $\text{NO}_3$  into  $\text{NO}_2$  faster than  $\text{NO}_2$  into  $\text{N}_2$ <sup>8</sup> and the final products of this process are gaseous nitrogen and its oxides. This process occurs in the absence of oxygen, in the presence of organic matter and by neutral or alkaline reactions.

The process of biological denitrification cannot explain all the gaseous losses from soils, especially when they occur in completely aerated soil. It was concluded that these losses occur by chemodenitrification and in addition to all, when there is an intense accumulation of nitrites and when the pH value of the soil is lower than 5.5 (water), the final products of this process are  $\text{NO}$ ,  $\text{N}_2\text{O}$  or  $\text{N}_2$  and the nitrites appear as an intermediate product. The appearance of the aforementioned gases in a completely sterilized soil is confirmation of the chemodenitrification process.<sup>9</sup> The chemodenitrification process occurs by one of the following reactions:

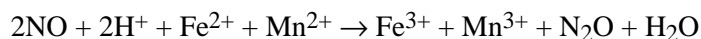
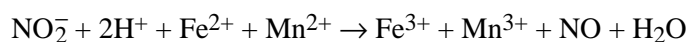
1. Self-decomposition of nitric acid:



2. Formation of molecular nitrogen in reactions of  $\text{NO}_2$  with ammonium salts and amino acids:



3. Formation of  $\text{NO}$  and  $\text{N}_2\text{O}$  from accumulated nitrites with participation of  $\text{Fe}^{2+}$  and  $\text{Mn}^{2+}$ :



Therefore, the nitrites in the soil are dominantly formed in two processes, namely in the process of nitrification and in the process of denitrification. In acid soils, nitrites often accumulate as a result of retarded biological nitrification<sup>10</sup> and chemodenitrification,<sup>9</sup> as well as in the presence of higher quantity of ammonium nitrogen in soil.<sup>11</sup> Formed nitrites in acid soils in any of the aforementioned

ways can remain for a longer or shorter period. The presence of increased nitrite quantities in the soil causes temporary chlorosis of plants and even their complete destruction.<sup>5,12</sup> Nitrites can also have toxic effects to humans and animals.<sup>13,14</sup> The quantities higher than 5 ppm in acid soils are considered as toxic and 10 ppm in neutral and alkaline soils, respectfully.<sup>5</sup>

The scope of these researches resulted from the fact that in Serbia there is the area of around 500,000 hectares of pseudogley type soil,<sup>15</sup> representing a significant part of the total cultivable area. The basic chemical property of pseudogley soil is that it belongs to the category of acid soils with typical excesses of soluble Al and Mn, which have harmful effects on cultivated plants.<sup>16</sup> Additionally, the occurrence of toxic quantities of nitrite nitrogen is possible, especially when larger quantities of fertilizer are applied. The purpose of this investigation was to determine in which quantities and under what conditions nitrites are accumulated in pseudogley soil, bearing in mind the fact that they can be toxic to plants.

#### EXPERIMENTAL

The experiments were performed on pseudogley soils taken from three localities near the city of Šabac. The soil samples were taken from a depth of 0–20 cm and then air-dried, triturated and sieved through a 2 mm sieve. The incubation experiments were performed and the chemical properties of the experimental soil established with samples prepared in this manner.

In order to observe nitrogen specific transformations in acid soils, three pseudogley soils of different acidity were chosen and incubation experiment under optimum moisture and temperature conditions was performed using high (100 ppm  $\text{NH}_4\text{-N}$ ) and very high nitrogen doses (300 ppm  $\text{NH}_4\text{-N}$ ). These doses are often used in inappropriate application of mineral fertilizers in fields, having negative effects on the plants, especially in acid soils.

##### *Incubation experiments*

The tested soils were submitted to short-term incubation experiments by a proposed procedure.<sup>17</sup> The following treatments: soil + water, soil + 100 ppm  $\text{NH}_4\text{-N}$  and soil + 300 ppm  $\text{NH}_4\text{-N}$  were applied. The experiments were performed with 30 % soil moisture at 20 °C. Thus, 10 g of soil samples were put in glass jars having a volume of 150 ml and then 3 ml of distilled water and 3 ml of an  $(\text{NH}_4)_2\text{SO}_4$  solution containing 100 and 300 ppm  $\text{NH}_4\text{-N}$  were added. The jars were closed with a thin plastic foil and thermostated at 20 °C. After the required incubation period (5, 8, 12, 15, 19 or 22 days), the jars were opened and 100 ml of a 2.0 M KCl solution added. The jars were then shaken for 1 h and the contents filtered.

The contents of  $\text{NH}_4$ ,  $\text{NO}_3$  and  $\text{NO}_2\text{-N}$  were determined in the extracts by the distillation method with hot water vapor. MgO as an alkaline agent and Devarda alloy were used in this method to reduce nitrate to ammonium. It was necessary to perform three distillations to determine  $\text{NH}_4$ ,  $\text{NO}_3$  and  $\text{NO}_2\text{-N}$ . In the first distillation of the extract,  $\text{NH}_4\text{-N}$  was determined when the MgO base was added and in the second distillation,  $\text{NO}_3 + \text{NO}_2\text{-N}$  was determined when the Devarda alloy was added. A fresh quantity of extract was taken for the third distillation, MgO was added as in the first distillation and the  $\text{NH}_4\text{-N}$  content was again determined, thus enabling the accuracy of the first distillation to be controlled. The remaining extract was cooled and a 0.20 M solution of sulfamine acid was added in order to destroy the nitrites. Devarda alloy was afterwards added, enabling the determination of the content of

NO<sub>3</sub>-N. The content of NO<sub>2</sub> was determined from the difference between confirmed nitrogen content in the second distillation (NO<sub>3</sub> + NO<sub>2</sub>-N) and the content of NO<sub>3</sub> determined in the third distillation.<sup>18</sup>

*Determination of the basic chemical properties of examined soils*

The pH value of the soil was determined by an Iskra pH meter using a glass (indicator) and a calomel (reference) electrode in suspensions: soil:water = 1:2.5 and soil:1 M KCl = 1:2.5.

The humus content was determined volumetrically after oxidation with excess 0.40 M K<sub>2</sub>Cr<sub>2</sub>O<sub>7</sub> in an acid environment (H<sub>2</sub>SO<sub>4</sub>). The K<sub>2</sub>Cr<sub>2</sub>O<sub>7</sub> remaining after the oxidation of the organic carbon in the soil was determined by the oxidation-reduction reaction with 0.10 M (NH<sub>4</sub>)<sub>2</sub>Fe(SO<sub>4</sub>)<sub>2</sub> using phenanthranilic acid as the indicator. The K<sub>2</sub>Cr<sub>2</sub>O<sub>7</sub> solution was standardized volumetrically with KMnO<sub>4</sub>, the molarity of which had been determined using pure oxalic acid as the standard substance.

The method for determination of the content of total nitrogen in the soil consisted of two steps: (1) sample digestion in order to transform the organic nitrogen into NH<sub>4</sub>-N and (2) determination of NH<sub>4</sub>-N in the solution after digestion. The digestion was performed by gradual heating to a temperature of 380 °C with p.a. H<sub>2</sub>SO<sub>4</sub> and by adding a catalyst mixture (K<sub>2</sub>SO<sub>4</sub>:CuSO<sub>4</sub>:Se = 100:10:1) in a period of 4 h. The NH<sub>4</sub>-N in the obtained digest was determined by catching the NH<sub>3</sub> released during the digest distillation with hot water vapor in the presence of excess NaOH. The released NH<sub>4</sub> passed through a cooler and was taken in a given volume of boric acid. Then, titration of the ammonium borate was performed with 0.010 M H<sub>2</sub>SO<sub>4</sub>.

Content of the mineral forms of nitrogen (NH<sub>4</sub>, NO<sub>3</sub> and NO<sub>2</sub>-N) before and after incubation were determined by the distillation method after extraction with 2.0 M KCl (100 ml), as explained in the part concerning the procedure for performing the incubation experiments.

## RESULTS AND DISCUSSION

The chemical properties of the examined soils are given in Table I.

TABLE I. Basic chemical properties of the examined soils

Soil	pH		Total nitrogen %	Humus %	Organic C %	Available N / ppm			
	Water	nKCl				NH <sub>4</sub> -N	NO <sub>3</sub> -N	NO <sub>2</sub> -N	Sum
Soil 1	5.80	4.80	0.11	1.60	0.93	7.0	2.8	2.8	12.6
Soil 2	4.90	3.45	0.12	1.44	0.84	26.6	18.2	1.4	46.2
Soil 3	4.65	3.20	0.13	1.80	1.04	28.0	25.2	7.0	60.2

Examined soils can be classified into the group of acid ones, whereby soil 1 was acid while soils 2 and 3 belong to the category of very acid. All three examined soils have a low content of humus and total nitrogen. The content of available nitrogen at the time of sampling of soil 1 was low and of soils 2 and 3 was high.

The results of the incubation experiments for the examined soils with only water added (soil + water) are shown in Fig. 1.

Initial content of available nitrogen in soil 1 was the lowest (12.5 ppm), while in other two soils had much higher amounts (soil 2 – 46.2 ppm and soil 3 – 60.2 ppm).

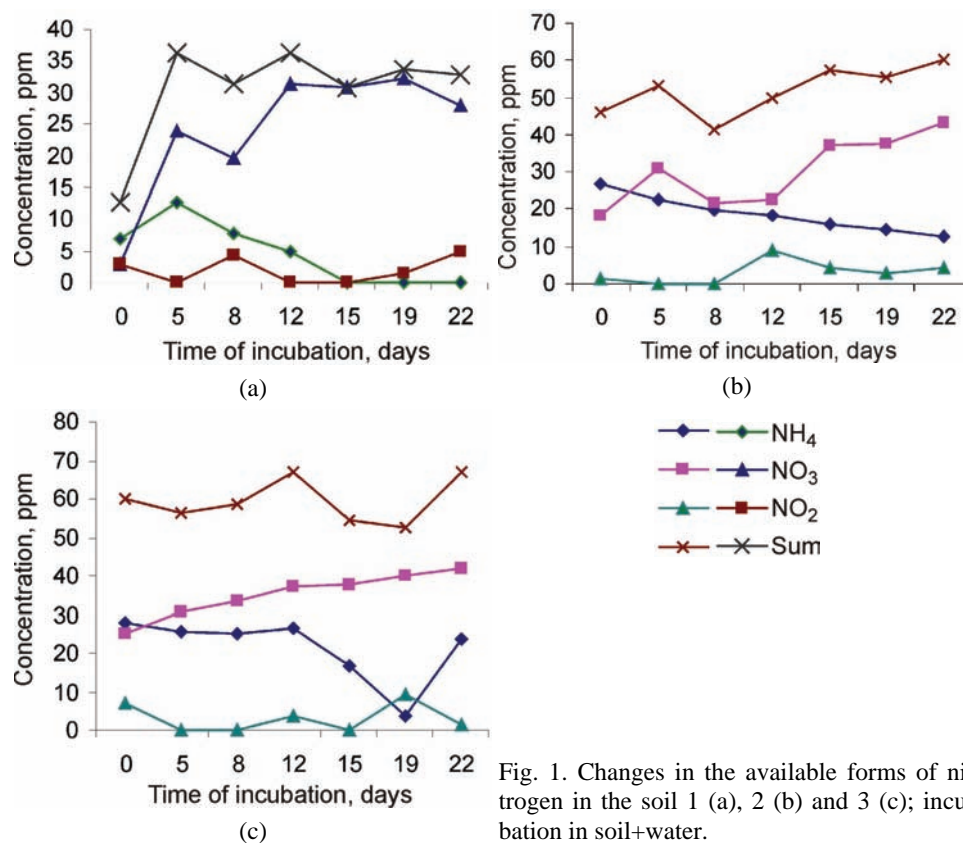


Fig. 1. Changes in the available forms of nitrogen in the soil 1 (a), 2 (b) and 3 (c); incubation in soil+water.

Taking into consideration the initial contents of available nitrogen in soil 1, the most intense nitrogen mineralization was created in a short time period (from initial 12.6 to 36.4 ppm after 5 days). During further incubation, the quantities of mineralized nitrogen showed a trend of either increasing or decreasing. This can be explained by the periodic occurrence of denitrification when some of the nitrogen disappears, while in the mineralization process it is generated. Nitrogen transformation in this soil was characterized by fixation of newly formed NH<sub>4</sub>-N, as well as its fast nitrification. NH<sub>4</sub>-N had disappeared by the end of experiment, but increased quantities of nitrogen nitrite forms were generated after 8 days and at the end of incubation period, day 22, had reached a value of 4.9 ppm. This can be connected with the processes of nitrification and denitrification, in which nitrites are formed as intermediate products.

Soil 2 was more acid (pH 4.90 in water) compared to soil 1 (pH 5.80), so that nitrogen mineralization was significantly retarded in this soil. The retardation was even more pronounced in soil 3, which had the lowest pH value, 4.65. Soils 2 and 3 are characterized by a more distinctive decelerated nitrification due

to the limiting influence of the pH value of the soils on biological nitrification. In soils 2 and 3, toxic amounts of nitrite appeared (9.1 ppm).<sup>5</sup> These toxic amounts appeared earlier (12<sup>th</sup> day) in soil 2. This phenomenon is connected with the decrease in the contents of  $\text{NH}_4$  and  $\text{NO}_3\text{-N}$  content. Thus, the increased nitrite content is brought into connection with retarded nitrification and denitrification.<sup>19</sup>

The results of the incubation experiments of examined soils with the addition of 100 ppm of  $\text{NH}_4\text{-N}$  are shown in Fig. 2.

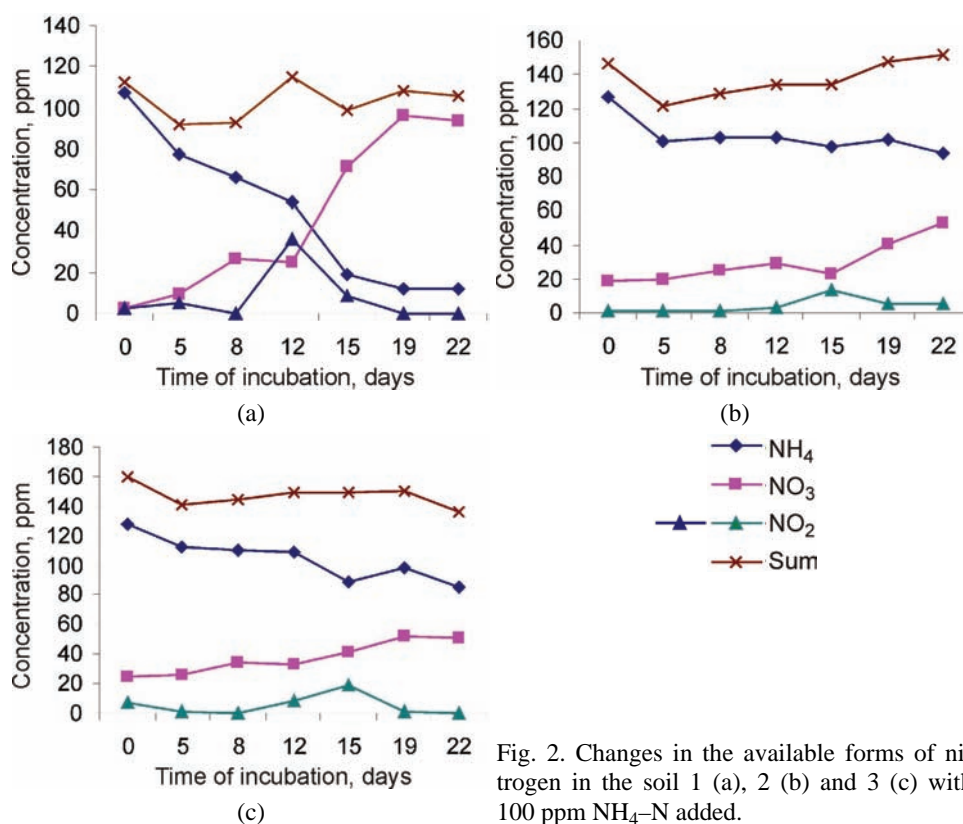


Fig. 2. Changes in the available forms of nitrogen in the soil 1 (a), 2 (b) and 3 (c) with 100 ppm  $\text{NH}_4\text{-N}$  added.

Regardless of the applied  $(\text{NH}_4)_2\text{SO}_4$ , there was no increased nitrogen mineralization in the soils in relation to the treatment without addition of this salt (soil+water).

The fastest changes in the processes of nitrification and denitrification were registered in soil 1. This is understandable taking into consideration the higher pH value of this soil and the fact that in the soil a constant source of  $\text{NH}_4\text{-N}$  was present, being the result of the  $(\text{NH}_4)_2\text{SO}_4$  addition. This soil contained the highest amounts of  $\text{NO}_2\text{-N}$  (35.7 ppm), which is the consequence of intense processes of nitrification and denitrification, as shown in a previous paper.<sup>16</sup>

In soils 2 and 3 that had a lower pH value, *i.e.*, they were more acid, the  $\text{NH}_4\text{-N}$  quantities decreased slower due to retarded biological nitrification, decreasing in that way the denitrification. In addition to acidity, these two processes were decelerated due to the influence of the addition of  $(\text{NH}_4)_2\text{SO}_4$  (100 ppm).<sup>20</sup> In these soils (2 and 3), smaller quantities of  $\text{NO}_2\text{-N}$  were observed compared to soil 1. However, in the later phases of incubation (on the 15<sup>th</sup> day, soil 2 – 14.0 ppm, soil 3 – 18.9 ppm) these quantities were also toxic for plants and microorganisms (>5 ppm).<sup>5</sup> The presence of toxic amounts of  $\text{NO}_2\text{-N}$  can be explained as resulting from processes of chemical nitrification<sup>16</sup> and chemodenitrification.<sup>21</sup> This was confirmed by the decreased total content of mineral forms of nitrogen at the end of the experiment.

The results of the incubation experiments of the examined soils with 300 ppm  $\text{NH}_4\text{-N}$  added are shown in Fig. 3.

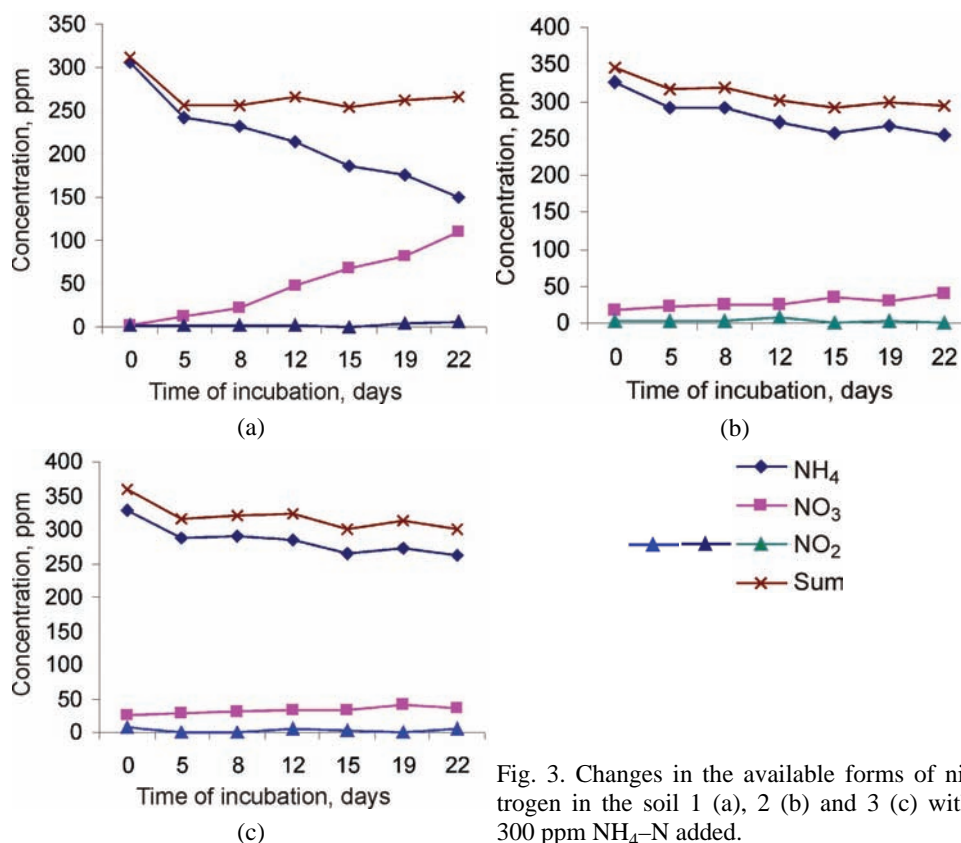


Fig. 3. Changes in the available forms of nitrogen in the soil 1 (a), 2 (b) and 3 (c) with 300 ppm  $\text{NH}_4\text{-N}$  added.

When larger quantity of  $\text{NH}_4\text{-N}$  (300 ppm) was added, besides the influence of the low pH value of soil 1, an inhibition effect of  $\text{NH}_4\text{-N}$  on the development

of biological nitrification and denitrification was also present, so that the deceleration of these processes was greater.

The process of biological nitrification still occurred in soil 1, but more slowly than in the experiment when a smaller quantity of  $\text{NH}_4\text{-N}$  was added. Under these conditions, nitrites were formed but in smaller quantities and the toxic amount appeared only at the end of the incubation experiment (on the 22<sup>nd</sup> day – 6.3 ppm).<sup>5</sup>

In more acid soils (2 and 3), the process of biological nitrification nearly ceased and nitrites did not appear in larger quantities. In both soils, the toxic amount of 6.3 ppm appeared in the middle of incubation period (12<sup>th</sup> day). However, the content of  $\text{NH}_4\text{-N}$  decreased during the incubation period, although slowly, as well as the quantity of mineral forms of nitrogen. This indicates the occurrence of gaseous losses, mostly chemodenitrification. Hence, nitrites were not accumulated. This was confirmed in experiments when  $\text{NaNO}_2$  was added.<sup>16</sup>

#### CONCLUSIONS

On the basis of the obtained results, it is possible to draw the following conclusions:

1. In the examined soils, the low pH value of the soils caused retardation of biological nitrification and denitrification, which was the reason for the occurrence of nitrite nitrogen in toxic quantities.

2. The other source of increased and toxic amounts of nitrite nitrogen in the examined soils (soils of higher acidity) was chemodenitrification upon application of  $(\text{NH}_4)_2\text{SO}_4$  (100 and 300 ppm  $\text{NH}_4\text{-N}$ ), when biological nitrification and denitrification was considerably retarded and even ceased.

3. Nitrites formed in the chemodenitrification process underwent spontaneous oxidation to nitrates by a chemical process (chemical nitrification).

4. On the basis of obtained results, the application of lower doses of nitrogen fertilizers in fields on pseudogley soil is recommended (50 ppm) in relation to the doses applied on neutral or alkaline soils. Using the lower doses, nitrogen losses due to denitrification might be decreased. The possibility of the occurrence of toxic quantities of nitrite, which often damage or destroy plants, could also be decreased.

#### ИЗВОД

#### СПЕЦИФИЧНОСТИ ТРАНСФОРМАЦИЈЕ МИНЕРАЛНИХ ОБЛИКА АЗОТА У КИСЕЛИМ ЗЕМЉИШТИМА

МИРЈАНА КРЕСОВИЋ<sup>1</sup>, МИОДРАГ ЈАКОВЉЕВИЋ<sup>1</sup>, СРЂАН БЛАГОЈЕВИЋ<sup>1</sup> и СРБОЉУБ МАКСИМОВИЋ<sup>2</sup>

<sup>1</sup>Пољопривредни факултет, Немањина 6, 11080 Земун и <sup>2</sup>Институт за земљиште,  
Теодора Драјзера 7, 11000 Београд

Истраживања су обављена на земљишту типа псеудogleј из околине Шапца. Испитивана земљишта спадају у групу киселих и јако киселих земљишта. Промене минералних облика азота су праћене помоћу краткотрајних инкубационих огледа (влажност 30 % и температура 20 °C), са и без додатка 100 и 300 ppm  $\text{NH}_4\text{-N}$ . Током инкубације утврђене су

повишене и токсичне количине нитрита, које су се у земљишном раствору задржавале више дана и недеља. Утврђене количине нитрита су се јављале као последица успорене биолошке нитрификације (код мање киселог земљишта), док су при додатку 100 и 300 ppm NH<sub>4</sub>-N оне настајале у процесу хемоденитрификације. У испитиваним земљиштима се одвијала и спонтана оксидација насталих нитрита хемијским путем (хемијска нитрификација). Да би се смањили губици азота процесом денитрификације и стварање токсичних количина нитрита на псеудоглејном земљишту се може препоручити примена нижих доза азотних ђубрива у односу на дозе које се примењују код неутралних и алкалних земљишта.

(Примљено 21. марта, ревидирано 30. јуна 2008)

#### REFERENCES

1. R. J. Haynes, in *Mineral Nitrogen in the Plant-Soil System*, T. T. Kozlowski, Ed., Wisconsin, Madison, 1986, p. 52
2. S. U. Sarathchandra, *Plant Soil* **50** (1978) 99
3. L. G. Morrill, J. E. Dawson, *Soil Sci. Soc. Am. Proc.* **31** (1967) 757
4. L. C. Burns, R. J. Stevens, R. J. Laughline, *Soil Biol. Biochem.* **28** (1996) 609
5. C. A. Black, *Soil-Plant Relationships*, 2<sup>nd</sup> Ed., Wiley, London, 1968, p. 464
6. R. J. Bartlett, *Soil Sci. Soc. Am. J.* **45** (1981) 1054
7. J. O. Reuss, R. L. Smith, *Soil Sci. Soc. Am. Proc.* **29** (1965) 267
8. M. P. Korsakova, *Microbiology* **2** (1941) 3
9. J. R. Haynes, R. R. Sherlock, in *Mineral Nitrogen in the Plant-Soil System*, T. T. Kozlowski, Ed., Wisconsin, Madison, 1986, p. 242
10. K. L. Sahrawat, *Plant Soil* **65** (1982) 281
11. L. C. Burns, R. J. Stevens, R. V. Smith, J. E. Cooper, *Soil Biol. Biochem.* **27** (1995) 47
12. M. N. Court, R. C. Stephens, J. S. Wais, *Nature* **194** (1962) 1263
13. W. M. Lewis, D. P. Morris, *Trans. Am. Fish. Soc.* **115** (1986) 183
14. F. B. Eddy, E. M. Williams, in *Water Quality for Freshwater Fish*, G. Howells, Ed., Gordon and Breach Science Publishers, Yverdon, 1994, p. 117
15. *Soil Map of Serbia* (scale 1:50.000), The Institute for Soil Science, Belgrade, 1964
16. M. Jakovljević, M. Kresović, S. Blagojević, S. Antić-Mladenović, *J. Serb. Chem. Soc.* **70** (2005) 765
17. J. M. Bremner, in *Methods of Soil Analysis*, C. A. Black, Ed., Madison, Wisconsin, 1965, p. 1324
18. R. J. Mulvaney, in *Methods of Soil Analysis*, J. M. Bigham, Ed., Madison, Wisconsin, 1996, p. 1123
19. Q. R. Shen, W. Raw, Z. H. Cao, *Chemosphere* **50** (2003) 747
20. S. S. Malhi, W. B. McGill, *Soil Biol. Biochem.* **14** (1982) 393
21. C. J. Smith, P. M. Chalk, *Soil Sci. Soc. Am. J.* **44** (1980) 277.